

# Peptide-based functional materials: From structural control to catalytic activities and inorganic-organic hybrids

ASHMEET SINGH

*A thesis submitted for the partial fulfillment of  
the degree of Doctor of Philosophy*



Institute of Nano Science and Technology  
Habitat Centre, Sector-64, Phase-10, Mohali, Punjab 160062, India

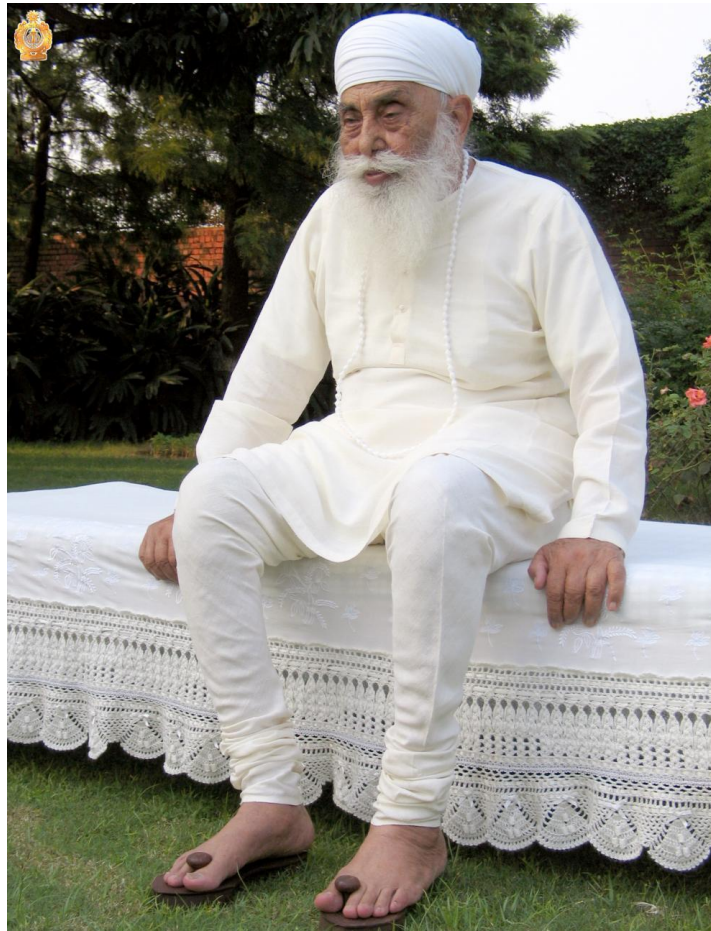
Indian Institute of Science Education and Research Mohali  
Knowledge city, Sector 81, SAS Nagar, Manauli PO, Mohali 140306, Punjab, India.

July 2020



*Dedicated to my beloved*

*His Holiness Sri Satguru Jagjit Singh Ji*

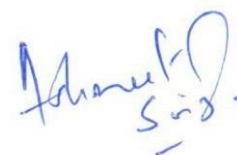






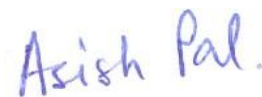
## **Declaration**

The work presented in this thesis has been carried out by me under the guidance of Dr. Asish Pal at Institute of Nano Science and Technology, Mohali. This work has not been submitted in part or in full for a degree, a diploma, or a fellowship to any other university or institute. Whenever contributions of others are involved, every effort is made to indicate this clearly, with due acknowledgement of collaborative research and discussions. This thesis is a bonafide record of original work done by me and all sources listed within have been detailed in the bibliography.



**Ashmeet Singh**

In my capacity as the supervisor of the candidate's thesis work, I certify that the above statements by the candidate are true to the best of my knowledge.



**Dr. Asish Pal**



## **Acknowledgments**

First and foremost, I would like to thank with the deepest sense of gratitude to my supervisor, Dr. Asish Pal, with his never-ending source of continuous help and guidance over my Ph.D. tenure. I have benefited beyond expression from his keen scientific attitude and vision, and I am grateful to have had a supervisor who has taken such great interest in teaching me his scientific ways, yet allowing me enough creative freedom to develop my own skills along the way. His friendly behavior always allowed me to discuss every aspect of my tenure with him and he always acted as a true mentor, provided his best advice on every front of my life. I am indebted to him for being the beacon of hope whenever I found myself in a scientific, professional, personal or financial crisis and he ensured that I had the best environment possible to conduct my research work.

I would like to thank Prof. Ashok Kumar Ganguli for his interest and enthusiasm in inspiring me throughout the last six years. As the founding director of Institute of Nano Science and Technology, he kept his administrative vows and created a harmonious place to generate the paramount scientific outputs. I will always remember him for his keenest attention to even the slightest details to ensure that no student faced any hardship even if this was as little as extending the shuttle timings to suit the students working late hours to as great as providing the best equipment, space and infrastructure for such a budding institute. The greatest attribute that I have learned from him that if you are at a good position in your life, help everyone who works under you so that they get motivated and should shine like you. It was my immense pleasure to volunteer in every conference and event organized under his leadership which has motivated and built my confidence to the next level.

I am grateful to Prof. H. N. Ghosh (Previous Director, INST) for his kind support especially to me. He has always encouraged me with his inspirational words. I am also grateful to Prof. Amitava Patra (Director, INST) for his support at the end of my PhD.

I would like to thank Late Shri P.K. Datta for his kind-hearted support. He always acted as a father-figure to me, encouraging me when I lose and cheering whenever I stood victorious. He will always have a dearest spot in my heart.

I would also like to acknowledge Dr. Dibyendu Das, Dr. Nirmalaya Chaki, and Dr. Surjit Karmakar for their role as my previous administrative supervisors. I would also like

to thank my thesis committee members Dr. Sangita Roy and Dr. Kamalakannan Kailasam for their kind and supportive guidance.

I would like to heartily appreciate my lab members Jojo P. Joseph, Deepika Gupta, Chirag, Nimisha, and Dr. Nidhi Gupta who helped me in conducting my research work, and also proof-reading my thesis. I would especially like to thank Jojo P. Joseph and Deepika Gupta with whom I spend most of my research time and appreciate their supportive nature whenever I required assistance. A special thanks to Chirag for his love and affection for me as my younger brother.

Friends who deserve a very special thank are Munish Shorie and Sandeep with whom I have successfully planned and executed my research activities in a cheerful and encouraging manner.

Thanks are also due to my collaborators. Dr. Bhagwati Sharma and Dr. Nidhi Gupta, in particular, helped me with a number of experiments and provided valuable insights into the project. I would like to especially thank Dr. Vinod Kumar and Dr. Sanjeev Sharma, brother figure to me who have been a continuous source of motivation and guidance.

Over the last six years, I have worked and spent maximum time in the INST lab at IISER campus alongside a fantastic and diverse bunch of people from all across the scientific domains. There are too many people to thank everyone individually, but I would like to record my gratitude to all of my lab-mates for their experience, their time and their company (enjoying their birthday parties), which they have shared freely throughout. Having said I won't list names, I am still bound to single out Swati, Ankur, Rajinder, Ritu, Soumen, Naimat, Renu, Taru, Kalpesh, Ritika, Deepika Rani, Navpreet, Rakesh Mishra, Avinash, Sushil, Neha Wadehra, Rohit, Kamaljit, Ajit *etc.* for their major contributions in making every moment of my tenure worth remembering.

I would like to mention Pulkit Bindra for his help in providing his laptop and for installing useful software in my laptop to process my data. I would like to thank my UGC fellowship partner Atul Dev and Saveena who helped me time to time.

It is my pleasure to pay a special thanks to Sonika Chibh. I have lost the count that she has dropped whatever she was doing in order to come to my aid. She has immensely supported me in my up and down moments. Her assistance has also been greatly appreciated which have carried me through the last four years--thank you.

I want to deeply thank my IISER friends (Shradha, Abhijeet, Gurdeep, Bishnu, Joydip, Priyanka, Bara Singh) who have arranged the essential chemicals for me in urgency. In-office, I would like to especially thank Mrs. Gurveen Kaur and Mr. Surender Singh for being unconditionally supportive to me. I am also thankful to Shweta Ma'am and Mukesh Raja Sir. I wish to thank Bharat and Vinod who ensured that we got the cleanest and most hygienic lab environment. I am also thankful to INST bus driver Ravinder Singh Ji who worked as many hours as we did and ensured that we never had to worry about reaching back after the long days. I really want to thank Vikram Ji for serving delicious and hygienic food that kept me healthy. I am also thankful to research vendors Maninder Singh, Jitender Singh, Simran Scientific, and especially Surajit Singh for delivering the chemicals and other necessary items to me on a timely basis.

I am thankful to all security guards of INST. I must say that they are very nice and their helping hands were always open for me. Without any reservation, I would like to name one by one, Gurinder, Vikram, Harbhajan uncle, Ranbir Ji, Harman, Gurdharam Ji, Venketeshwar Ji, Narender uncle, Uttam uncle---thanks a lot!

I am also grateful to the Peptide synthesizer engineers (Mr. Nand Kumar Thite, Kuldeep, and Balbir) who have been the sources of great technical assistance, troubleshooting even over phone calls to keep the instrument functional. I owe them all the weeks they saved with this kind gesture.

No acknowledgments would be complete without thanking INST for providing the best research facility, instruments, space, research funding, and state-of-art infrastructure for conducting my research. I am highly grateful to IISER for providing a hostel for the initial three years of my Ph.D. tenure, a fantastic Wi-Fi facility, an air-conditioned library facility, *etc.*

How I can forget the continuous showering of blessings and love from *Sri Satguru Jagjit Singh Ji* and *Sri Satguru Uday Singh Ji* to me that made me strong enough to tackle every situation and helped to follow a path of Gursikhi in life.

At last, I hugely thank my family members, especially my parents, my mother Sardarni Baljit Kaur and my father Sardar Paramjeet Singh who have been hugely supportive of my time taking research career. I would also like to thank my grandmother Bibi Swaran Kaur who always remembers me in her prayers, seeking goodness and happiness for me.



# TABLE OF CONTENTS

<b>Contents</b>	<b>i</b>
<b>Acronyms</b>	<b>v</b>
<b>Abbreviations</b>	<b>vi</b>
<b>Synopsis</b>	<b>vii</b>

## **Chapter 1: Introduction**

1.1. Self-assembly	1
1.2. Supramolecular polymerization and control over nanostructures	2
1.3. Peptide as a building block for self-assembly	9
1.4. Peptide-based hydrogels and their applications	12
1.5. Self-assembled peptide nanostructures in catalysis	15
1.6. Self-assembled organic-inorganic hybrid, bioactive glass	21
1.7. Scope of Research	24
1.8. References	25

## **Chapter 2: Chirality control to multi-stimuli responsive and self-healing supramolecular metallo-hydrogels**

2.1. Introduction	31
2.2. Results and Discussion	32
2.2.1. Control over gelation	33
2.2.2. Multi-stimuli response of the hydrogel	36
2.2.3. Structural characterizations of the hydrogel	39
2.2.4. Microscopic Characterizations	40
2.2.5. Supramolecular Chirality	41
2.2.6. Rheological Investigation	43
2.3. Conclusion	46
2.4. Experimental Section	47
2.4.1. Materials	47
2.4.2. Instrumentation	47
2.4.3. Methods	47
2.4.3.1. Preparation of Zn-histidine metallogels	48
2.4.3.2. Interaction of <i>L</i> -histidine with Zn <sup>2+</sup> ions in mixed solvent systems	48
2.4.3.3. Stimuli responsive studies of the Zn-histidine metallogels	48
2.4.3.4. Transmission electron microscopic studies	49
2.4.3.5. Circular Dichroism studies	49

2.4.3.6. Rheological studies	49
2.5. References	50

### **Chapter 3: Pathway driven self-assembly and living supramolecular polymerization of an amyloid-inspired peptide amphiphile**

3.1. Introduction	53
3.2. Results and Discussion	54
3.2.1. Design of Peptide Amphiphile	54
3.2.2. Self-assembly	55
3.2.2.1. Circular Dichroism (CD) Spectroscopy	55
3.2.2.2. Microscopic investigation	56
3.2.2.3. Binding to Thioflavin-T	59
3.2.2.4. Small angle X-ray scattering (SAXS)	60
3.2.3. Nucleation mediated growth: Seeded Supramolecular Polymerization (SSP)	60
3.2.4. Hydrogel network formation	66
3.3. Conclusion	70
3.4. Experimental Section	70
3.4.1. Materials	70
3.4.2. Methods	71
3.4.2.1. Synthesis of peptide 1	71
3.4.2.2. Atomic Force Microscopy (AFM)	71
3.4.2.3. Transmission Electron Microscopy (TEM)	72
3.4.2.4. Generation of Seeds by mechanical agitation	73
3.4.2.5. Analysis of average length from AFM images	73
3.4.2.6. Seeded Supramolecular Polymerization	73
3.4.2.7. SAXS study	74
3.5. References	75

### **Chapter 4: Modulation of catalytic activities mediated by pathway driven nanostructures**

4.1. Introduction	77
4.2. Results and Discussion	79
4.2.1. Design of Peptide Amphiphiles	79
4.2.2. Self-assembly	80
4.2.2.1. Microscopic study	80
4.2.2.2. Photo-dimerization Studies	82
4.2.2.3. Monitoring Host-Guest complexation by $^1\text{H}$ NMR Spectroscopy	84
4.2.2.4. UV Spectroscopy	87



4.2.2.5.	CD Spectroscopy	87
4.2.2.6.	Kinetics Study	88
4.3.	Conclusion	92
4.4	Materials and Methods	93
4.4.1.	Materials	93
4.4.2.	Methods	93
4.4.2.1.	Synthesis of peptide 1	94
4.4.2.2.	Atomic Force Microscopy (AFM)	95
4.4.2.3.	Transmission Electron Microscopy (TEM)	94
4.4.2.4.	Kinetics of <i>para</i> -nitrophenyl acetate ( <i>p</i> -NPA) hydrolysis	94
4.4.2.5.	Rate of hydrolysis of <i>p</i> -NPA	96
4.4.2.6.	Kinetics study on nylon 0.22 $\mu\text{m}$ filter	96
4.5.	References	97

## **Chapter 5: Peptide nanostructures directed bioglass composites as dynamic and self-healable bone matrix mimick**

5.1	Introduction	99
5.2	Biom mineralization on self-assembled nanostructures and characterization	101
5.2.1.	Atomic Force Microscopy (AFM)	101
5.2.2.	Persistence length ( $L_p$ )	102
5.2.3.	Scanning Electron Microscopy (SEM)	103
5.2.4.	Energy Dispersive X-ray Spectroscopy (EDX)	104
5.2.5.	Thermogravimetric Analysis (TGA)	105
5.2.6.	X-ray Diffraction (XRD)	106
5.2.7.	Fourier Transform Infrared (FTIR) Spectroscopy	106
5.2.8.	Raman Spectroscopy	108
5.2.9.	X-ray Photoelectron Spectroscopy (XPS)	109
5.2.10.	Rheological Studies	111
5.3.	Bioactivity Study	113
5.3.1.	Scanning Electron Microscopy (SEM)	112
5.3.2.	Fourier Transform-Infrared Spectroscopy (FTIR)	114
5.3.3.	X-ray diffraction Studies (XRD)	114
5.3.4.	Effect of pH	116
5.3.5.	Biocompatibility Study	117
5.4.	Conclusions	120
5.5.	Experimental Section	120
5.5.1.	Materials	120
5.5.2.	Methods	120
5.5.2.1.	Design of self-assembled peptide templated bioactive glass	120
5.5.2.2.	Thermo-gravimetric Analysis (TGA)	121
5.5.2.3.	Atomic Force Microscopy (AFM)	121

5.5.2.4. Scanning Electron Microscopy (SEM)	121
5.5.2.5. X-ray Diffraction (XRD)	122
5.5.2.6. Fourier Transform Infra-Red spectroscopy (FTIR)	122
5.5.2.7. Raman Scattering Spectroscopy	122
5.5.2.8. High-resolution X-ray photoelectron spectroscopy (XPS)	122
5.5.2.9. Rheology	122
5.5.2.10. Bioactivity Test	123
5.5.2.11. Cell Culture Studies	123
5.5.2.12. Evaluation of cellular morphology through bright field microscopy on hydrogel surfaces	124
5.6. References	125
<b>Publications</b>	127
<b>Awards</b>	129
<b>Curriculum Vitae</b>	131

## ACRONYMS

pH	The negative logarithm of hydronium-ion concentration ( $-\log_{10} [\text{H}_3\text{O}^+]$ )
UV-vis	UV-Visible Spectroscopy
FTIR	Fourier Transform Infrared
XRD	X-ray Diffraction
TEM	Transmission Electron Microscopy
HRTEM	High Resolution Transmission Electron Microscope
SEM	Scanning Electron Microscopy
XPS	X-ray Photoelectron Spectroscopy
EDX	Energy Dispersive X-ray Spectroscopy
SAED	Selected Area Electron Diffraction
DNA	Deoxyribonucleic Acid
AFM	Atomic Force Microscopy
CD	Circular Dichroism
TGA	Thermogravimetric analysis
NMR	Nuclear magnetic resonance
Ee	Enantiomeric excess
Fmoc	fluorenylmethyloxycarbonyl
$\gamma$ -CD	$\gamma$ -cyclodextrin
HPLC	High-Performance Liquid Chromatography
NP	Nanoparticle
NF	Nanofiber
NS	Nanosheet
TB	Twisted Bundle

## ABBREVIATIONS

$\lambda$	Wavelength
$\varepsilon$	Extinction coefficient
$\alpha$	Alpha
$\Sigma$	Sigma
$\Gamma$	Gamma
$\Delta$	Delta
$\Pi$	Pi
$\text{\AA}$	Angstrom
$^{\circ}\text{C}$	Degree Centigrade
nm	Nanometer
$\mu\text{m}$	Micrometer
cm	Centimeter
mL	Millilitre
$\mu\text{L}$	Microlitre
pM	Picomolar
$\mu\text{M}$	Micromolar
mM	Millimolar
$\Theta$	Theta
mW	Milliwatt
BG	Bioglass
BO	Bridging oxygen
NBO	Non-bridging oxygen

# Synopsis

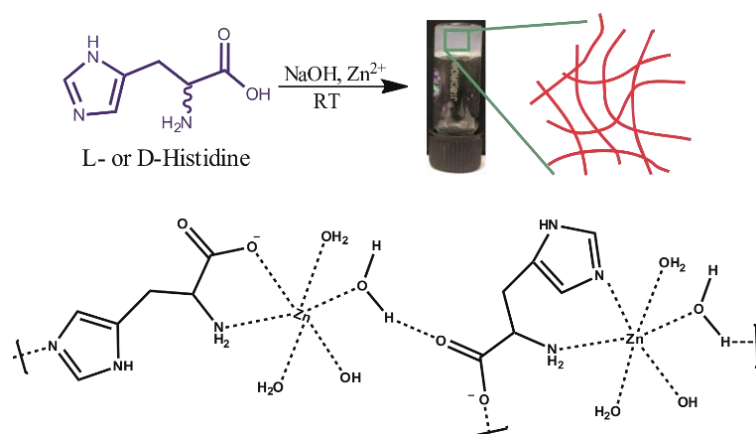
## Chapter 1. Introduction

This chapter introduces the fundamental concepts of self-assembly to result in complex structures through the mediation of non-covalent interactions. Such bottom-up self-assembly allows chemists to create supramolecular materials with structural and functional control in a diverse hierarchical regime from nanometer to micrometer. However, the natural supramolecular systems employ out-of-equilibrium pathways, while chemists have till date designed mostly equilibrium self-assembly in laboratories. Recently, attempts are being made to design kinetically controlled system where parameters such as solvents, temperatures, pH are found to be crucial to alter the nature of the self-assembly pathways and have been summerized here. Living supramolecular polymerization exploiting nucleation-elongation growth has emerged a fascinating protocol to create complex yet precise self-assembled nanostructures, that is discussed in details. On the functional aspect, we discussed the catalytic properties of the self-assembled nanostructures in the quest for new, robust enzyme mimetic biomaterials. In this regard, a special focus is laid on the minimalistic peptides-based robust artificial enzyme owing to their similarity with the native protein by means of amino acid as the building blocks. Further, inorganic-organic hybrids are designed which involve a range of peptide that can be mineralized with bioactive glass composites which showed enhanced mechanical properties in comparison to its native scaffolds by mediation of hydroxyapatite formation, a prerequisite for mimicking bone matrices with immense applications in bone tissue engineering.

## Chapter 2. Chirality control to multi-stimuli responsive and self-healing supramolecular metallo-hydrogels

This chapter discusses the stereo-selective co-ordination mediated self-assembly of metal-based hydrogel in a single step is performed using naturally occurring, amino acid, histidine with Zn (II) ions (Scheme 2.1.). Mixing an aqueous solution of  $Zn(NO_3)_2$  (100 mM) with an alkaline deprotonated solution of histidine (pH  $\approx$  12.3) (100 mM) in a 1:1 molar ratio results in self-standing stable Zn-His hydrogel. The hydrogel formation is instantaneous and exhibits stimuli-responsive behaviour with respect to pH, heat and external chemicals. The

gelation ability depends on the optical purity and enantiomeric excess of the amino acids. The supramolecular chirality mediated by Zn-histidine complex and subsequent fiber formation is studied using circular dichroism (CD) spectroscopy that shows sign inversion of CD signal with respect to that of native amino acids (*L*- or *D*-). Job's plot from the circular dichroism probing supramolecular chirality confirms 1:1 complex of Zn and histidine. The viscoelastic property and kinetics of the hydrogel can conveniently be tuned by changing its enantiomeric excess (ee%), concentration and the ratio of Zn and histidine. Moreover, the resulting metallo-hydrogel is thixotropic in nature and exhibits instantaneous, intrinsic self-healing behaviour.

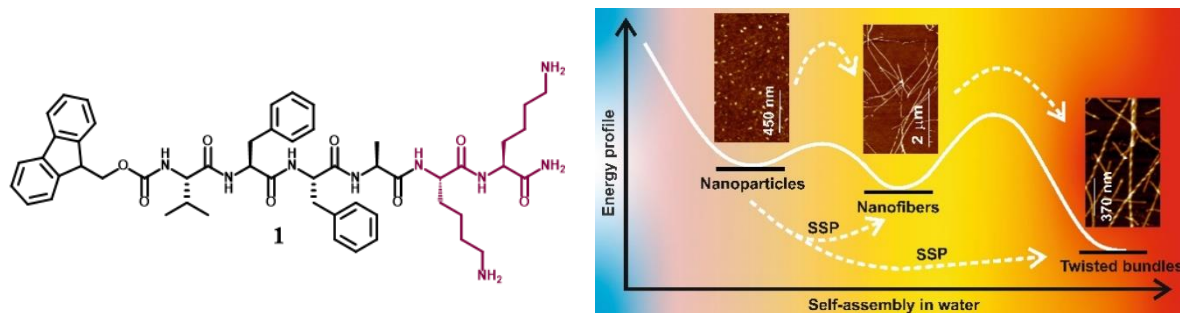


**Scheme 2.1.** Proposed structure of the complex upon interaction of histidine with Zn (II) ions that results in the formation of supramolecular metallo-hydrogel.

### Chapter 3. Pathway driven self-assembly and living supramolecular polymerization in an amyloid-inspired peptide amphiphile

The peptide amphiphile **1** inspired by the  $\beta$ -amyloid nucleating core of A $\beta$ 42 is designed by tethering a hydrophobic groups at the N-terminal and two hydrophilic lysine units at the C-terminal of a short peptide sequence <sup>N</sup>VFFA<sup>C</sup> (Scheme 3.1). The peptide demonstrates step-wise self-assembly in water. Variation of temperature or solvent composition arrests the self-assembly to result metastable nanoparticles with height of ~3-4 nm and diameter ranging from 30-40 nm at 10°C, which on gradual increase in temperature produce kinetically controlled nanofibers with height of ~4 nm and diameter of ~8-9 nm at 25°C and eventually thermodynamically stable twisted helical bundles at 80 °C. Mechanical agitation of the fibers

is performed which furnishes short seeds with narrow polydispersity index, which by mediation of seeded supramolecular polymerization establishes a perfect control over the



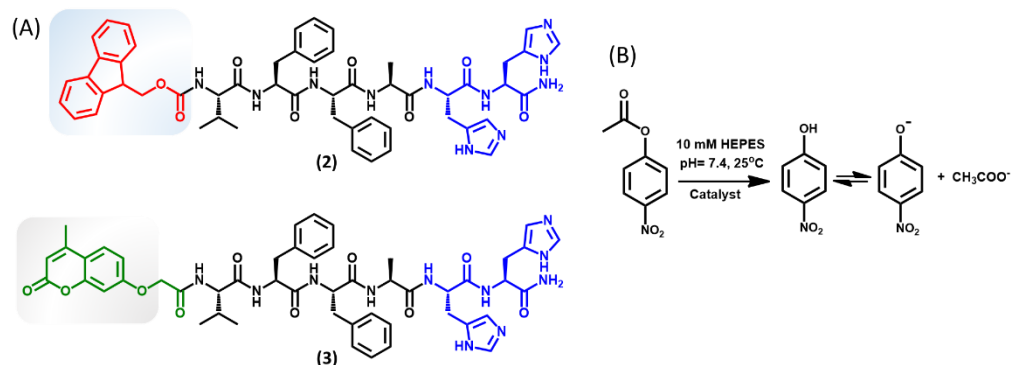
**Scheme 3.1.** Chemical structure of the peptide amphiphile **1** and pathway driven self-assembly to produced different nanostructures.

length of the nanofibers. To ascertain the living nature of the fiber ends, nucleation and fiber elongation are performed with the sequential addition of the freshly prepared monomer to result in a stepwise increase in the length of the fibers. The peptide fibers are positively charged at physiological pH due to protonation of lysine side chains. Addition of sodium phosphate buffer transforms the peptide solution into a hydrogel via physical cross-linking of the fibers with negatively charged counter anions. Such pathway dependence and the length control of the supramolecular peptide nanofibers is exploited to tune the mechanical strength of the resulting hydrogel materials.

#### **Chapter 4. Modulation of catalytic activities mediated by pathway driven nanostructures**

The rationale design of short peptides **2** and **3** with Fmoc- and photodimerizable moiety 4-methyl coumarin respectively at N-terminal and two histidine units at C-terminal to render temperature and photo-stimuli mediated self-assembly (Scheme 4.1). Temperature dependent self-assembly results in the formation of metastable nanoparticles from **2** (**2<sub>NP</sub>**) and **3** (**3<sub>NP</sub>**) at 10°C which transforms to nanofibers of **2** (**2<sub>NF</sub>**) and **3** (**3<sub>NF</sub>**) at 25°C. Interestingly, further increasing the temperature of fibrous solution of **2** (**2<sub>NF</sub>**) to 85°C, resulted in twisted bundles (**2<sub>TB</sub>**). Equimolar concentration  $\gamma$ -Cyclodextrin is added to a solution of metastable nanoparticle of **3** (**3<sub>NP</sub>**) and subsequent irradiation with UV light ( $\lambda_{\text{max}} = 320 \text{ nm}$ ) drives the morphology to form 2D nanosheets (**(di-3<sub>C</sub> $\gamma$ -CD)<sub>NS</sub>**). These different

nanostructures from **1** and **2** were employed to mimic the complex hydrolase enzyme activity using para-nitrophenylacetate (*p*-NPA) as a model substrate results in the formation of para-nitrophenolate ion (*p*-NP) as the product. The kinetic parameters of rate of hydrolysis of



**Scheme 4.1** Molecular structure of (A) the peptide amphiphiles **2** and **3** (left). (B) Hydrolase catalytic activity for the conversion of *p*-NPA to *p*-NP (right).

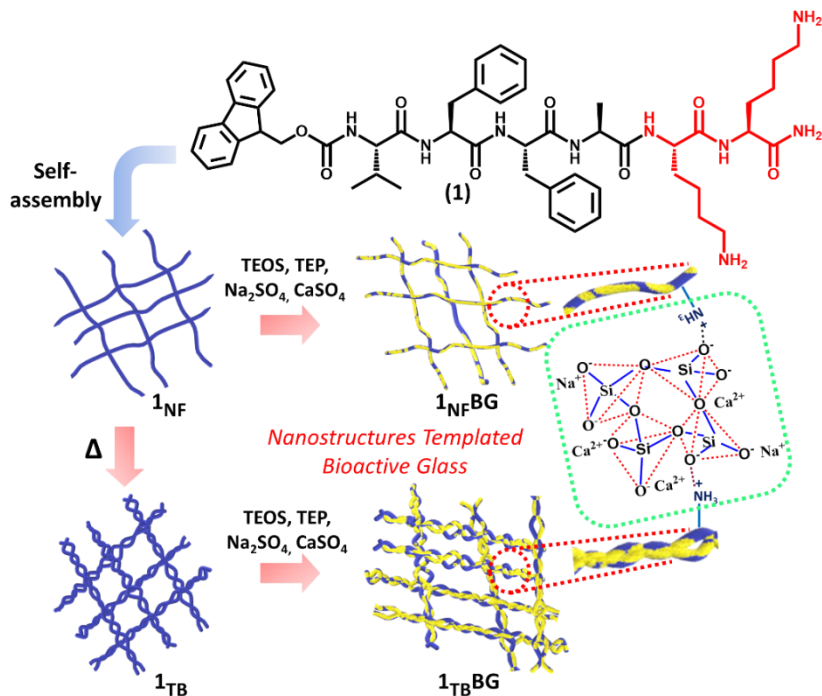
*p*-NPA were obtained by fitting in Michaelis Menten's equation. Interestingly, we observed that different morphologies had different binding efficacy for the substrate (*p*-NPA) which eventually reflected in different catalytic efficiencies ( $k_{cat}/K_m$ ) for the product formation.

## Chapter 5. Peptide nanostructures directed bioglass composites as dynamic and self-healable bone matrix mimick

Peptide hydrogels have recently emerged as potential biomaterials for designing synthetic scaffold in tissue engineering. We demonstrate pathway controlled self-assembly of peptide amphiphile **1** to furnish kinetically controlled nanofibers (**1<sub>NF</sub>**) and thermodynamically stable twisted helical bundles (**1<sub>TB</sub>**). These supramolecular nanostructures with different persistence lengths promote *in situ* mineralization to result templated bioactive glass composites, **1<sub>NF</sub>BG** and **1<sub>TB</sub>BG**- resorbable and degradable biomaterials as bone scaffolds (Scheme 5.1). The structural features of the hydrogel composites were investigated extensively with microscopic characterization, EDX, Raman, XPS to conclude **1<sub>TB</sub>BG** as superior materials with higher percentage of open network structures as obtained from ratios of non-bridging and bridging oxygen. The hydrogel composites showed excellent dynamic and self-healing behavior from rheological studies, especially the elastic moduli of **1<sub>TB</sub>BG** being almost comparable to natural bone. Upon



incubation in simulated body fluid, the bioglass composites illustrated tunable bioactive response mediated by the structural and topological control to induce the deposition of multiphasic calcium phosphate along with octacalcium phosphate and carbonate hydroxyapatite.



**Scheme 5.1** Molecular structures of the peptide amphiphile, **1** and its pathway driven self-assembly to render nanostructures, **1<sub>NF</sub>** and **1<sub>TB</sub>**. The nanostructures with positively charged lysine moieties at surfaces are utilized as higher propensity sites for the bioactive glass mineralization. Tetraethyl ortho-silicate (TEOS), triethylphosphite (TEP), sodium sulphate and calcium sulphate were used as precursor to Si, P, Na and Ca content of bioactive glass, respectively.



# Chapter 1

## Introduction

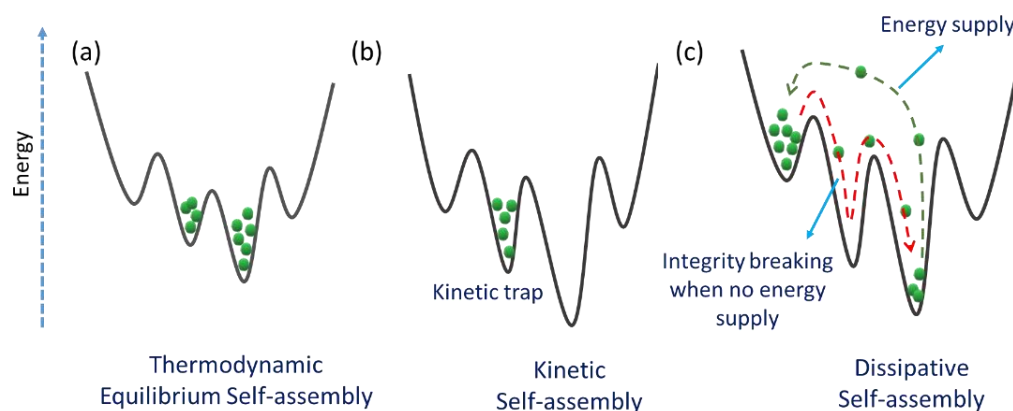
*This chapter starts with a discussion of different types of self-assembly. A special focus is laid for creating a variety of nanoarchitectures especially with their structure, shape, and length control which further find applications towards catalysis and designing inorganic-organic hybrids such as bioglass composite materials.*

### 1.1. Self-assembly:

Self-assembly is a spontaneous process for the formation of organized structures using a bottom-up approach and can be controlled by the judicious design of building block components, environment and driving interactions. Self-assembly is abundant in biological systems and natural examples such as DNA double helix, collagen, microtubules and protein folding *etc.* are result of the interplay of multiple non-covalent interactions. Self-assembling systems play a significant role in performing physiological functions and have therefore, attracted remarkable consideration owing to their immense potential for various biological applications. The self-assembly process are of three types: (a) thermodynamic, (b) kinetic and (c) dissipative and are discussed below:

- (a) **Thermodynamic or equilibrium self-assembly:** As the name suggests, equilibrium means reversibility. Molecules from the monomeric state can easily enter self-assembled systems and self-assembled molecules can easily go back to the monomeric state (Scheme 1.1a). This is owing to the quite low energy gap between the two states and thus molecules possess a low activation energy barrier to exchange between the states. Thermodynamically self-assembled structures are quite stable and they persist in the lowest free-energy state. The only way to move the systems away from their states is possible by generating a new minimum energy state in the same energy landscape.
- (b) **Kinetic self-assembly:** Self-assembled system results in the formation of a single structure that defines the property of the system. Systems are transiently stable and trapped in the lower free-energy state that on the supply of activation energy or with

incubation time-period changes to lowest free-energy state (Scheme 1.1b).



**Scheme 1.1.** A representative scheme illustrating the different routes of self-assembly. (a) Thermodynamic or equilibrium, (b) kinetic trap and (c) dissipative self-assembly.

(c) **Dissipative self-assembly:** System requires a continuous supply of energy to maintain its integrity. As soon as the energy supply stops, the system starts falling apart into the lowest free-energy state (Scheme 1.1c). Unlike equilibrium and kinetic self-assembly, the state of the system can be changed with the constant energy supply that will result in the formation of different self-assembled structures.

Most of the supramolecular systems as traditionally investigated till last decade are under thermodynamic control. However, more recently, self-assembly processes ruled by kinetic trap and energy dissipation are appearing in literature, thereby, rendering such emergent self-assembly an exciting field of research.

## 1.2. Supramolecular polymerization and control over nanostructures:

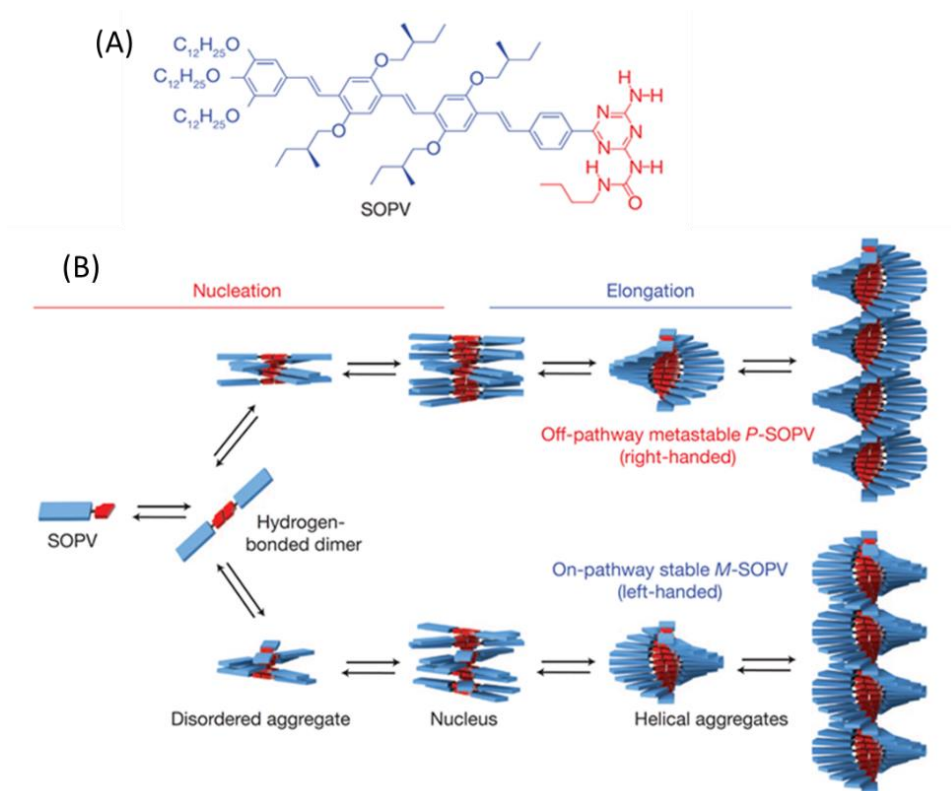
In 1920, Hermann Staudinger described that polymeric substances are the long chains of repeating molecules that are connected through covalent bonds<sup>[1]</sup> which he termed as macromolecules in 1922. A decade later, Wallace H. Carothers nicely conveyed his brilliant thoughts about the rapidly evolving field of synthetic polymers in his review entitled as “polymerization”.<sup>[2]</sup> He categorized macromolecules by the polymerization mechanism

involved such as step-growth, chain-growth, or ring-opening polymerizations. Supramolecular polymers are rather polymers with individual monomeric units connected together through directional and reversible non-covalent interactions. Through the years, many excellent reviews and books have been published describing progress in the area of supramolecular polymers that is defined as the “*polymeric arrays of monomeric units that are brought together by reversible and highly directional secondary interactions, resulting in polymeric properties in dilute and concentrated solution as well as in the bulk. The directionality and strength of the supramolecular bonding are important features of systems that can be regarded as polymers and that behave according to well-established theories of polymer physics.*”

Along with the synthesis of a range of polymers, the interactions between molecular units became equally important to understand the properties of the material at the molecular level. The supramolecular polymers are distinguished by the type of interactions such as hydrogen bonds,  $\pi$ - $\pi$  interactions, hydrophobic interactions and metal-ligand binding that result in the formation of hierarchical self-assemblies.<sup>[3-9]</sup>

Living polymerization introduced in the 1950s,<sup>[10]</sup> has set a standard, that is leading a comprehensive advancement in covalent polymer synthesis.<sup>[11,12]</sup> However, its supramolecular counterpart has rather evolved recently. There are numerous exciting reports that show the formation of a range of polymeric architectures that depend on secondary supramolecular interactions.<sup>[13-21]</sup> One of the first such examples of living seeded polymerization of amphiphilic block-copolymers yielded micelles with controlled length through an epitaxial crystallization process.<sup>[20,22,23]</sup> Manner *et al.* were first to report this crystallization-driven self-assembly (CDSA) in block co-polymeric chains. Moreover, crystallization-driven polymerizations represent a synthetic tool to create a variety of complex and hierarchical nanostructures that can be tailored in two dimensions (2D) producing block micelles.<sup>[24-26]</sup> Similarly, Aida and co-workers achieved a p-n heterojunction through seeded growth of hexabenzocoronene derivatives into semiconducting nanotubes.<sup>[27]</sup> This paid a footstep towards the logical advancement in this research field that has initially been established under thermodynamic control resulting in equilibrium

structures. A vast majority of supramolecular polymers, formed through an isodesmic or a cooperative mechanism, are investigated under thermodynamic control.<sup>[28–30]</sup> However, the understanding of pathway complexity, coexistence of multiple competitive pathways in self-assembly process, provided a new paradigm and tool to control the fate of supramolecular systems under a variety of conditions.<sup>[31–35]</sup> E.W. Meijer *et al.* have shown that S-chiral oligo(*p*-phenylenevinylene) (SOPV) assembles to result right handed off-pathway



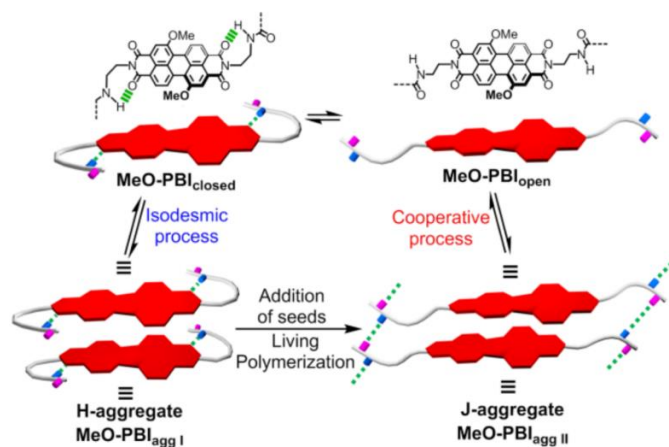
**Scheme 1.2.** (A) Chemical structure of the S-chiral oligo(*p*-phenylenevinylene) (SOPV) derivatives. (B) Schematic demonstration for SOPV derivative where two helical aggregation pathways are competing with each other. The quickly formed right-handed *P*-helices are less stable than to its transformation into left-handed *M*-helical aggregates through the nucleation-elongation mechanism as shown by E.W. Meijer *et al.* (Reprinted with permission from reference<sup>[31]</sup>. Copyright 2012, Springer Nature).

metastable aggregate (*P*-SOPV) and left-handed on-pathway stable aggregate (*M*-SOPV) through nucleation elongation mechanism depending on the solvent systems (interplay of polar and apolar) and reaction conditions employed. The group has demonstrated that the

kinetically favored metastable right-handed off-pathway aggregate eventually transforms to thermodynamically stable left-handed aggregate (*M*-SOPV) as shown in Scheme 1.2. Thus, two competing pathways lead to the formation of two different helical aggregates.<sup>[31]</sup> It is essential to construct a far-from-equilibrium condition using kinetically controlled self-assembly. A promising method to get control over the kinetics of one-dimensional aggregation processes is living supramolecular polymerization. The living supramolecular polymerization has been achieved using seed-mediated as well as the initiator molecule mediated approach, where either added seeds or properly designed molecules that function as initiators for the growth of monomers into one-dimensional non-covalently bound molecular aggregates. The kinetically trapped species generate an out-of-equilibrium scenario in which the nucleation of the monomers, prior to the subsequent elongation, is retarded. There are scarce examples of kinetically controlled supramolecular polymerization that proceeds through the formation of metastable species, which are crucial for the consecution of seeded supramolecular polymerizations. Such kinetically controlled self-assembly resulted in out-of-equilibrium structures with precise control over their shape, dimension with narrow polydispersity index regulated by kinetics.

The “seeding” approach has been applied to porphyrin dye for the first time by Sugiyasu, Takeuchi and co-workers in 2014 to control the nanostructure of supramolecular polymers with a unimolecular width. They demonstrated seed-initiated living supramolecular polymerization of porphyrin-based monomers, leading to supramolecular polymers with controlled length and narrow polydispersity.<sup>[36]</sup> To achieve living supramolecular polymerization, an in-depth understanding of the mechanistic path of supramolecular polymerization is required based on both thermodynamic and kinetic insights. Frank Würthner *et al.* explained that seeded polymerization is effective under the following conditions: (a) polymerization route through a nucleation-elongation cooperative model, in such a way that growth of the fiber is assisted by the addition of seeds to the monomer solution; (b) supramolecular polymerization is kinetically controlled if the spontaneous nucleation is arrested or very slow; (c) an independent preparation of seeds that initiate the supramolecular polymerization externally. A planar perylene bisimide (PBI)

derivatives have evolved as one of the most intensively investigated classes of  $\pi$ -conjugated molecules. PBI containing amide groups at the imide positions is kinetically inactivated under appropriate conditions in the monomeric state because the amide hydrogens are intramolecularly hydrogen-bonded to the imide carbonyl oxygens of the PBI which starts polymerizing in the presence of seeds. Thus, molecular design, solvent systems, and appropriate conditions play a significant role in programming a kinetically trapped species.<sup>[37]</sup> Moreover, Frank Würthner *et al.* have discussed about the kinetic and thermodynamic supramolecular polymerizations of a series of amide functionalized PBI organogelator molecules with alkyl spacers of various lengths between the amide and PBI imide moiety.<sup>[38]</sup> They have explained PBI based system that self-assembles into kinetically trapped H-type aggregates, which can be converted into thermodynamically favored J-aggregates by the addition of seeds to achieve living polymerization. This polymerization cycle could be repeated several times consuming “living” polymer from the preceding cycle as shown in Scheme 1.3.<sup>[36,39,40]</sup>

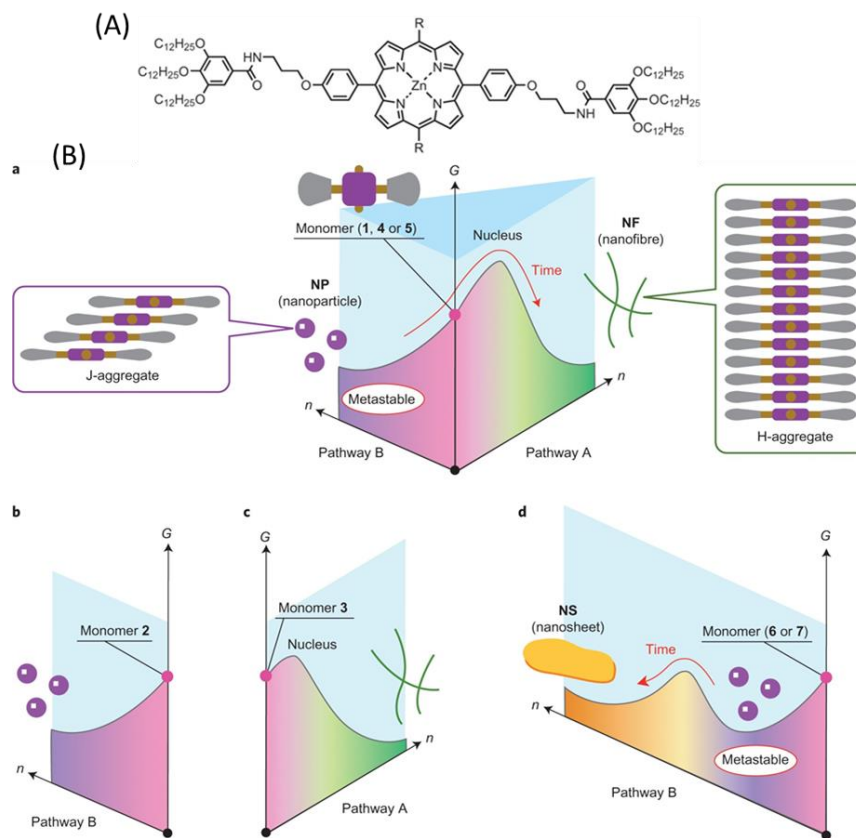


**Scheme 1.3.** Schematic representation of the spontaneous transformation of H-aggregate to J-aggregate on the addition of seeds, shown by Frank Würthner *et al.* (Reprinted with permission from reference<sup>[40]</sup>. Copyright 2017, Angewandte Chemie, Wiley).

Masayuki Takeuchi, Kazunori Sugiyasu, and coworkers have reported the metastable porphyrin derivatives supramolecular assemblies can be tuned to form 1D nanofiber (face-to-face H-aggregate) and 2D nanosheet (en route short-slipping J-aggregate) as shown in Scheme 1.4. The interplay of molecular design, molecular recognition, and pathway



complexity in the self-assembly revealed the energy landscape that showed kinetic behavior. Introducing more steric hindrance to the molecule avoids the face-to-face stacking (H-aggregate) and do not result in nanofibers and thus follow pathway B to result nanosheet.<sup>[39]</sup> The molecular design with an additional non-covalent interaction such as intramolecular

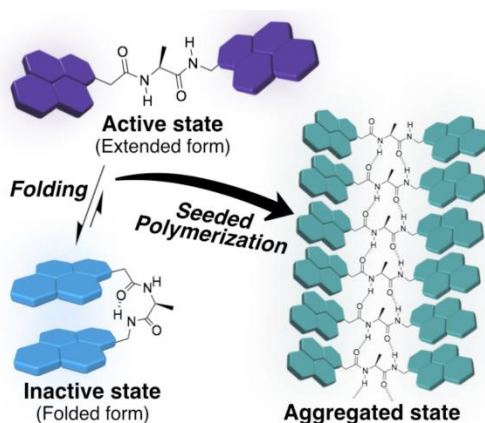


**Scheme 1.4.** (A) Chemical structure of the porphyrin derivative. (B) Self-assembly energy landscapes of porphyrin derivatives. (a-d) Self-assembled energy landscapes for a range of porphyrin derivatives. Red arrows show the transformation on time lag: (a) metastable nanoparticles are kinetically formed and they transformed into (a) nanofiber and (d) nanosheet after an incubation period shown by Masayuki Takeuchi, Kazunori Sugiyasu and coworkers. (Reprinted with permission from reference<sup>[39]</sup>. Copyright 2018, Springer Nature).

hydrogen bonding is a suitable approach to produce aggregation. For instance, Miyajima, Aida, and co-workers have demonstrated that a spontaneous polymerization of a bowl-shaped corannulene derivative bearing five amide groups is retarded in nonpolar solvent. This arrested monomeric state in an intramolecular hydrogen-bonded conformation and its

chain-growth polymerization can be initiated by the addition of a non-hydrogen bonded derivative.<sup>[41,42]</sup>

Takeuchi and Sugiyasu showed the photo-switching of azobenzene from *cis* to *trans* form which results in the formation of the supramolecular polymer. The inactive dormant monomer can be activated by UV irradiation and if seed solution is also present, it will trigger the growth through seeded supramolecular polymerization.<sup>[43]</sup> The interplay of dynamic covalent chemistry and self-replication was used by Sijbren Otto *et al.* to grow kinetically controlled fibers in an aqueous milieu from metastable macrocycles with an excellent length control.<sup>[44]</sup> Ogi, Yamaguchi and coworker reported that the interplay of folding and aggregation of a pyrene-substituted diamide was exploited to achieve seed-mediated supramolecular polymerization (Scheme 1.5). Thermodynamic and time-dependent studies revealed that the folding of the diamide moiety as a result of intramolecular hydrogen bonds retarded spontaneous nucleation required for supramolecular



**Scheme 1.5.** Schematic representation of the spontaneous formation of aggregated state on the addition of seeds to the active state shown by Ogi, Yamaguchi, and coworker. (Reprinted with permission from reference<sup>[45]</sup> Copyright 2018, Angewandte Chemie, Wiley).

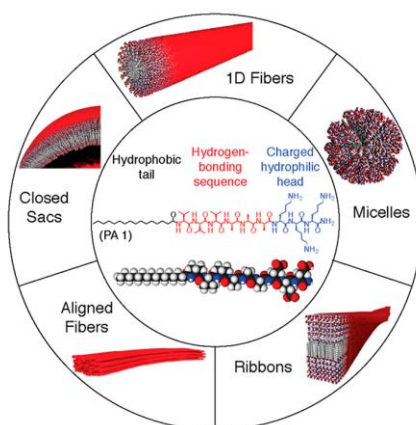
polymerization. The addition of seeds solution effectively initiated the supramolecular polymerization in such out-of-equilibrium conditions. Thus, these results provided the efficacy of such amino acid-based diamides in controlling the seed-mediated supramolecular polymerizations.<sup>[45]</sup> Suhrit Ghosh *et al.* showed that naphthalene-diimide derivatives revealed a useful approach to arrest monomers in its inactive dormant state and introducing

active seed solution initiated supramolecular polymerization with perfect control by a chain-growth mechanism.<sup>[46,47]</sup> The nucleation-elongation model in amyloid fibril formation, as observed in prion infection,<sup>[48,49]</sup> provides a vital cue to study the pathway complexity to get an insight into the fibrillation.<sup>[50,51]</sup>

### 1.3. Peptide as a building block for self-assembly:

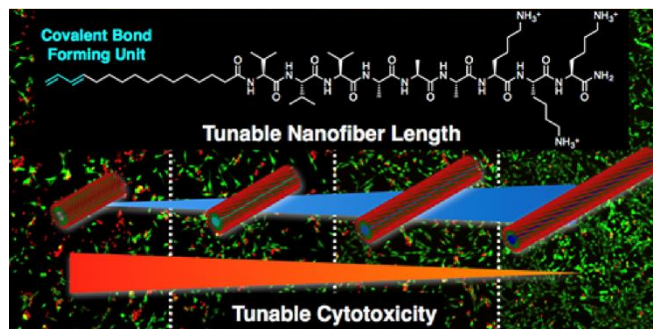
The fabrication of new materials using natural building blocks, such as phospholipids, oligosaccharides, oligonucleotides, proteins, and peptides, has become a subject of major interest.<sup>[52]</sup> Among them, peptides have drawn significant attention due to their simple structure, relative chemical, and physical stability, diversity in sequences and shapes, and the feasibility to synthesize them in large amounts. Also, peptides are known as interesting building blocks for creating self-assembled nanostructures in biomedical applications due to their intrinsic biocompatibility, biodegradability as well as ease of availability.<sup>[53]</sup>

Samuel I. Stupp and coworkers focus on supramolecular chemistry and materials science, learning towards the functional aspect of the designed bio-material. Group has the expertise in designing peptide amphiphiles that are capable to self-assemble to result in a range of hierarchical structures (Scheme 1.6). Further, these hierarchical structures were investigated towards its bioactivity studies.<sup>[54]</sup> Recently, the group has shown a strategy to



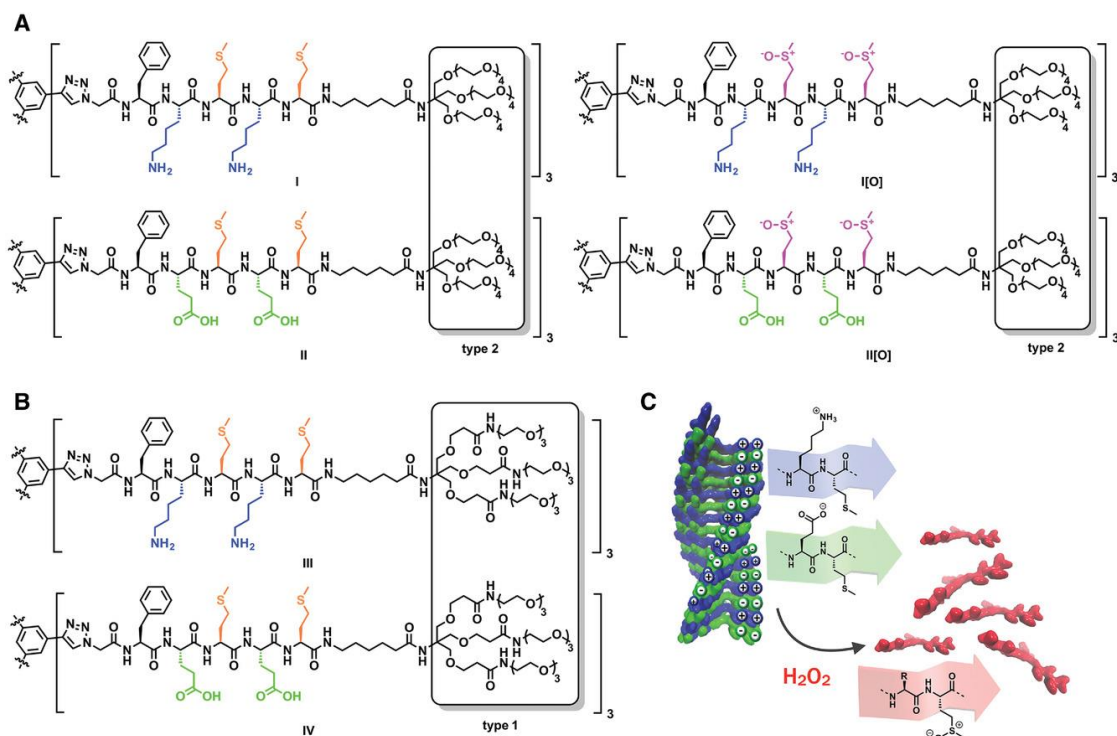
**Scheme 1.6.** Chemical structure of a peptide amphiphile (center) surrounded by a range of supramolecular nanostructures that is a result of self-assembly shown by Samuel I. Stupp *et al.* (Reprinted with permission from reference<sup>[54]</sup>. Copyright 2017, American Chemical Society).

have perfect control over the length of supramolecular assemblies. On irradiation of light at a wavelength of 365 nm, the covalent bond formation among photoactive moieties in the peptide amphiphiles takes place leading to covalently fixated fibers length (Scheme 1.7). They further investigated the cell viability study depending on the length of the fiber and found that as the length of the fiber is increasing, the cytotoxicity is reducing.<sup>[55]</sup>



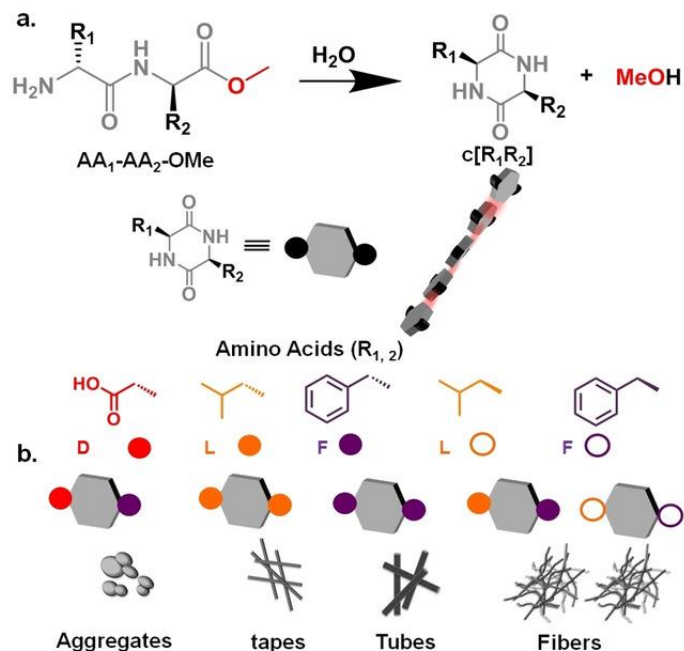
**Scheme 1.7.** Representative scheme showing the perfect length control over the fibers with tunable cytotoxicity explained by Samuel I. Stupp *et al.* (Reprinted with permission from reference<sup>[55]</sup>. Copyright 2017, American Chemical Society).

Pol Besenius and coworkers demonstrated the synthesis of peptide-based copolymers that self-assembled to form nanorods in water. The incorporation of methionine as hydrophobic amino acid supports  $\beta$ -sheet formation, but oxidation of the thioether moiety to a sulfoxide group destabilizes nanorods (Scheme 1.8). Further, to stabilize the assembly, they introduced a Newkome type dendron owing to its good water solubility. The group monitored the oxidation kinetics using hydrogen peroxide as reactive oxygen species. They reported that the oxidative disassembly of charged ampholytic copolymers is up to two times faster as compared to neutrally charged homopolymers. This work finds its importance in view of tuning the oxidation induced disassembly which tends to be extremely slow and requires high concentrations of reactive oxygen species and acidic media.<sup>[56]</sup> Further, they reported pH-responsive self-assembly of peptide-based copolymer systems using diethoxy substituted naphthalene diimide (NDI). The study demonstrated the importance of molecular design on their structure that directs the functional properties.<sup>[57]</sup>



**Scheme 1.8.** Schematic representation of FKMKM peptide-motif containing monomers **I** and **III**, of the FEMEM containing monomers **II** and **IV**, and the oxidized monomers **II[O]** and **III[O]** with the dendron (A) type 2, (B) type 1. (C) A representative scheme showing the oxidative disassembly, shown by Pol Besenius *et al.* (Reprinted with permission from reference<sup>[56]</sup>. Copyright 2019, Wiley).

Dipeptides are known to spontaneously cyclize to result diketopiperazines and triggers the self-assembly to yield nanostructures. Rein Ulijn *et al.* demonstrated *in situ* cyclization of dipeptide methyl esters by intramolecular aminolysis in buffer solution. The *in situ* cyclization leads to the formation of a variety of supramolecular nanostructures (Scheme 1.9). The nature of the amino acid at the side chain functionality directs the nanostructures. Cyclized **LF** resulted in the formation of supramolecular gels, and mechanical properties of the formed hydrogels can be tuned by varying the concentration of the precursor molecules.<sup>[58]</sup> Prashant Kumar Das *et al.* demonstrated elaborate expertise in designing molecules that exhibit self-assembling behavior. The materials find a wide variety of applications ranging from biocatalysis to biomedical that includes cargo delivery, biosensing, and antimicrobial tissue engineering.<sup>[59,60]</sup>



**Scheme 1.9.** (A) Reaction scheme showing aminolysis of dipeptide methyl esters molecules resulted in cyclization in phosphate buffer, pH 8.0 at 25 °C. Chemical structures of the various dipeptide methyl ester and their cyclized products with the different amino acids at the side chain functionality represented by a single letter code. (B) Scheme showing different cyclized products and their self-assembly through the mediation of H-bonding resulted in various nanostructures, shown by Rein Ulijn *et al.* (Reprinted with permission from reference<sup>[58]</sup>. Copyright 2020, Wiley).

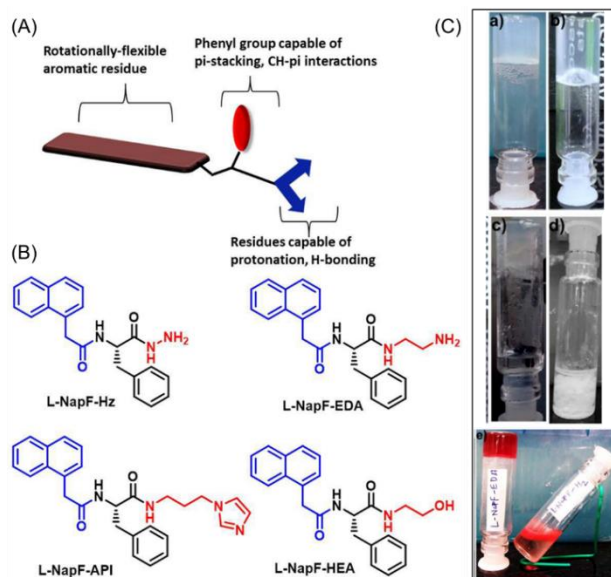
#### 1.4. Peptide-based hydrogels and their applications:

Supramolecular peptide-based hydrogels are fascinating to attract worldwide attention for various biological applications such as drug delivery, tissue engineering, biosensing, wound healing, bioimaging, nanomedicine *etc.* owing to their biocompatibility, biodegradability and low toxicity.<sup>[61,62]</sup> These hydrogels consisting of three-dimensional network of self-assembled peptides are semi-solid viscous like biomaterials with more than 90% of water. Bing Xu *et al.* in 2005 reported controlled release of pamidronate drug from amino acids based hydrogel (Fmoc-Leu-OH and Fmoc-Lys-OH). The *in-vivo* study performed in mice showed the significant recovery of uranium-infected skin wounds when treated with pamidronate drug entrapped in the hydrogel network.<sup>[63]</sup> In 2014, Charlotte A.E. Hauser *et al.* designed a hydrogel system from the self-assembly of two hexapeptides,



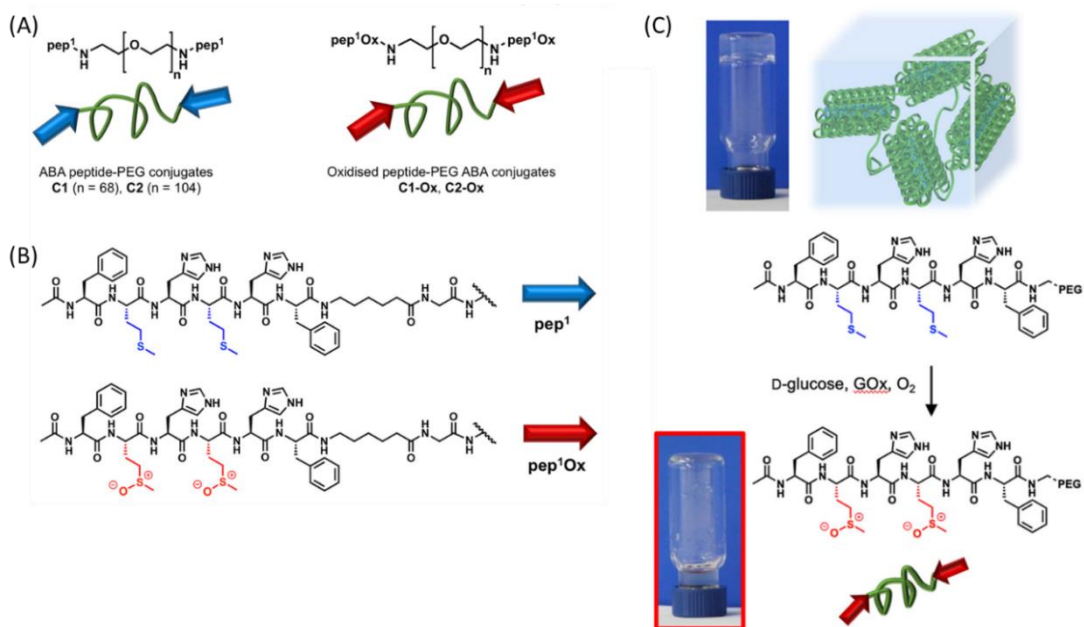
ILVAGK and LIVAGK, for application towards skin wounds. They exhibited remarkable recovery of the burn wounds mediated by the hydrogels.<sup>[64]</sup> Zhibo Li *et al.* in 2017, reported the antimicrobial application of cationic peptide amphiphiles based hydrogels.<sup>[65]</sup> Further, the development of peptide hydrogel-based biosensors is an expeditiously broadening field of research. In this regard, Wensheng Yang *et al.* reported a dipeptide based (Fmoc-FF) self-assembled hydrogel that forms a smart bio interface for enzyme-based electrochemical biosensing application. They demonstrated the use of dipeptide based hydrogel as a host for horseradish peroxidase (HRP) enzyme and showed the detection of hydrogen peroxide levels released from HeLa cells in *in-vitro* experimental conditions.<sup>[66]</sup>

Aasheesh Srivastava *et al.* demonstrated the self-assembly of short derivatives of *L*-phenylalanine and *L*-alanine anchored with rotationally-flexible 1-naphthaleneacetyl (1-Nap) as a protecting group at N-terminal. The C-terminal ends were tethered with a range of amines functionality molecules such as hydrazine (Hz), ethylenediamine (EDA), 3-aminopropylimidazole (API), and hydroxyethyl amine (HEA) to result in *L*-NapF-Hz, *L*-NapF-EDA, *L*-NapF-API, and *L*-NapF-HEA respectively (Scheme 1.10). Their variable



**Scheme 1.10.** (A) Structural motif and (B) chemical structures of different derivatives of *L*-NapF, (C) Digital images of the hydrogels from a) *L*-NapF-Hz, b) *L*-NapF-EDA, c) *L*-NapF-API, d) precipitates of *L*-NapF-HEA, e) Doxorubicin encapsulated gels from *L*-NapF-EDA, while sol from *L*-NapF-Hz shown by Aasheesh Srivastava *et al.* (Reprinted with permission from reference<sup>[66]</sup>. Copyright 2020, Wiley).

self-assembly resulted in the formation of rigid rods, helical nanofibers, and spherulites. Thus, they demonstrated the importance of flexible motif attached within the designed molecules that promotes design of proficient hydrogelators which can trap/release drug molecules on demand.<sup>[67]</sup> D.J. Pochan *et al.* designed an injectable thermo-responsive peptide-based hydrogel for drug delivery applications that self-assemble into a hydrogel with an increase in temperature, and completely dissolved by reverting the temperature back to room temperature.<sup>[68]</sup> Yashveer Singh *et al.* developed peptides based on natural and unnatural amino acids conjugated with chitosan (Boc-*D*-Phe- $\gamma^4$ -*L*-Phe-PEA (NH007)/chitosan and Boc-*L*-Phe- $\gamma^4$ -*L*-Phe-PEA (NH009)/chitosan) which self-assembled to form gels. The resulted peptide composites hydrogel possess a good antibacterial property that prevented biomaterial-related infections.<sup>[69]</sup> Pol Besenius *et al.* demonstrated the synthesis of hexapeptide-poly(ethylene glycol) conjugates with an alternating amino acid in the sequence (ABA-type) based on Phe-Met-His (Scheme 1.11) that exhibit multi-stimuli



**Scheme 1.11.** (A) Chemical structure and a representation of ABA-type polymer peptide conjugates (C1, C2) and its oxidized conjugates (C1-Ox, C2-Ox). (B) Chemical structure of the deprotected peptide strand (pep1) and respective oxidized peptide (pep1Ox). (C) Physical cross-linking of the nanorods mediated hydrogel that on oxidation triggered disassembly of the nanorods resulting gel to sol transition, shown by Pol Besenius *et al.* (Reprinted with permission from reference<sup>[69]</sup>. Copyright 2019, European Polymer Journal).



responsive behavior. The self-assembly of the designed system results in the formation of nanorods that were stabilized by the shielding corona of PEG, a hydrophilic polymer. The physical cross-linking of the nanorods network results in the formation of hydrogels at physiological pH, 25 °C. The presence of thioether functionality of methionine group in the peptide motif show oxidation responsive behavior. The group has nicely demonstrated the production of reactive oxygen species triggered by glucose molecules.<sup>[70]</sup>

The design and construction of injectable new hydrogel for biomedical applications still remains a challenge to researchers. Arindam Banerjee and coworkers designed a tripeptide that resulted in the formation of the hydrogel at physiological pH, 25°C. Moreover, the hydrogel exhibited thixotropic behavior and thus was used for injectability. This hydrogel encapsulated antibiotic vancomycin and vitamin B12 that showed its slow release behavior. Pertinently, the hydrogels were performed for the cytotoxicity study and it showed that 100 % cell viability indicating it as non-toxic hydrogel material.<sup>[71]</sup> The group has also demonstrated amphiphilic tyrosine-based self-healable, multi-stimuli responsive metallo-gels that exhibit multi-stimuli responsive behavior. The formation of the hydrogels from the tyrosine molecule is highly selective towards Ni<sup>2+</sup> ions. The mechanical stiffness and self-healing behavior can be tuned by varying the aliphatic chain anchored at N-terminal to the amino acid.<sup>[72,73]</sup>

We believe that a profound understanding is required regarding the self-assembly process and the gelation properties of peptide amphiphiles which helps in programming the peptides for diverse biomedical applications. To assist a better control over the gelation properties for biomedical studies, it is important to understand the self-assembly process of the peptides which can result in hydrogel formation. There is a need for designing a hydrogel system that can be modified easily with no compromise over biocompatibility.

### **1.5. Self-assembled peptide nanostructures in catalysis:**

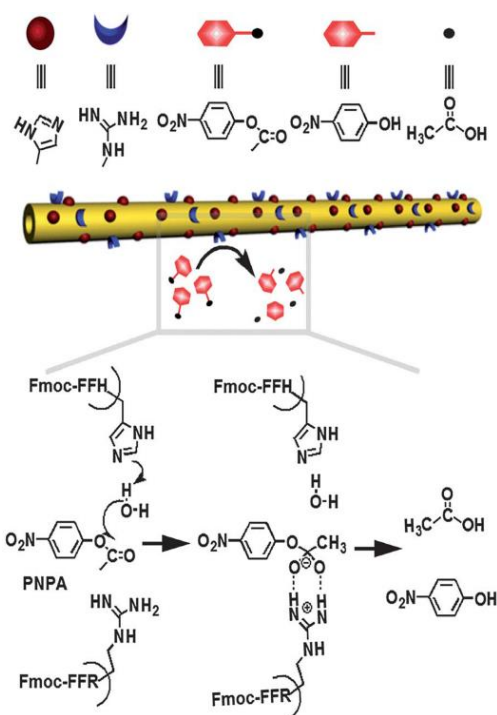
Enzymes are natural biocatalysts that accelerate the rate of several biochemical reactions with high efficiency and selectivity under ambient conditions that make life

sustainable. Hydrolytic enzymes or hydrolases are particularly an important class of enzymes responsible for the catalytic disintegration of a range of unique chemical bonds.<sup>[74-76]</sup> There are several distinct hydrolases including proteases, lipases, nucleases, and amylases, each possessing a specific biochemical function.<sup>[76]</sup> The serine proteases are the well-studied and biological significant class of hydrolase enzymes<sup>[87-89]</sup> with a single active site that contributes towards their catalytic activity. The three amino acids present on the active site that cooperatively drive the catalysis are Serine (Ser, S), Histidine (His, H), and Aspartic acid (Asp, D).<sup>[79,80]</sup> This triad of Ser-His-Asp motif is one of the thoroughly studied and characterized catalytic triads, among the other known triad Cys-His-Asp, Ser-His-His, and Ser-Glu-Asp in natural hydrolytic enzymes.<sup>[81]</sup> The region known as the binding pocket surrounds the active site, that can attract, react, and bind with specific substrates, as well as enable the discharge of products. Protein binding pocket dynamics are important for their interaction specificity with the incoming substrate molecule. The presence of functional groups and their orientation ('lock') on the active site interact with the substrates of a certain shape/size ('key') via an induced fit model, thereby enabling highly specific target structures of the parent enzyme.<sup>[82-84]</sup> Effective covalent interaction between the substrate transition states during catalysis, and residues in the vicinity of the active site, lower the activation energy and thus is the driving force for the formation of the transition state. Stabilization of the transition state depends on the binding efficacy of the enzyme with the transition state during catalysis than binding to the substrate/reactant in the ground state. H-bonding and directional electric fields due to charged functional groups also help in stabilizing the transition state.<sup>[85,86]</sup>

The key structural aspect of catalysis are considered to establish the criteria for designing synthetic or *de novo* enzyme mimics.<sup>[87-91]</sup> The aim of the synthesized bio-inspired materials is to generate artificial catalyst that can mimic the natural enzyme with respect to catalytic activity with comparable reaction kinetics. The catalytic amino acid residues of the active site contribute to the hydrolytic reaction of interest.<sup>[92]</sup> However, it is precise structural conformations, local ambient conditions in the vicinity of the active site that give rise to the proficient catalysis that is observed for these materials. Numerous research efforts

considerably lifted up this vast area in the past to artificially construct catalytic features using various biomolecules, particularly for mimicking the catalytic triad.<sup>[93–95]</sup>

While these synthetic molecules based artificial enzymes show catalytic activity, they also overcome the shortcoming of natural enzymes, such as instability, low activity, and poor reusability under non-ambient conditions. Many synthetic materials like nucleic acid complexes,<sup>[96–98]</sup> metal nanoparticles,<sup>[99,100]</sup> metal-organic frameworks,<sup>[101,102]</sup> macrocyclic compounds,<sup>[103,104]</sup> *etc.* have been created that showed altered catalytic efficiency. The evolution of supramolecular chemistry promotes the prosperity of functional supramolecular materials.<sup>[105]</sup> Among various other self-assembled systems, the self-assembly of peptide-based supramolecular materials have gained much attention in the biomedical field owing to their tunable well-ordered structures and good biocompatibility.<sup>[106–110]</sup> Peptide-based supramolecular materials have fetched massive attention for biochemists. Zupeng Huang *et al.* constructed a novel hydrolase model *via* self-



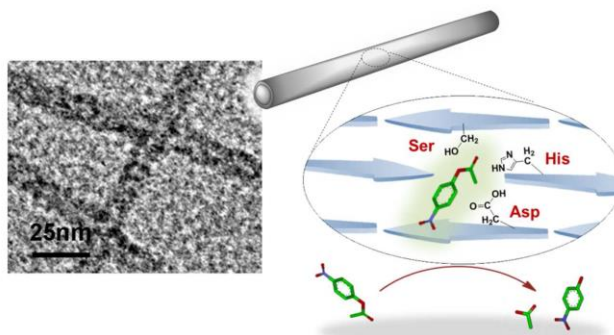
**Scheme 1.12.** A scheme illustrating the peptide nanotube-based hydrolytic property shown by Huang *et al.* (Reprinted with permission from reference<sup>[111]</sup>. Copyright 2013, American Chemical Society).

assembly of a synthetic amphiphilic short peptide Fmoc-FFH-CONH<sub>2</sub> into nanotubes. The peptide-based self-assembled nanotubes (PepNTsHis) with imidazolyl groups as the catalytic centers exhibit high catalytic activity for *p*-nitrophenyl acetate (*p*-NPA) hydrolysis. Substituting histidine with arginine peptide Fmoc-FFR-CONH<sub>2</sub>, and their co-assembly with Fmoc-FFH-CONH<sub>2</sub> significantly improved the catalytic efficiency. A mechanistic scheme is discussed showing catalytic behavior (Scheme 1.12).<sup>[111]</sup>

Meital Reches and Ehud Gazit first reported self-assembly of diphenylalanine dipeptides into nanotubes in water to eventually harvest discrete silver nanowires.<sup>[112]</sup> Even very short peptides can self-assemble into “protein-like” supramolecular aggregates that possess enantio-selectivity towards catalysis.<sup>[113]</sup> Thus, short peptides can promote distinct chemical reactions with a high order of magnitude in the catalytic rate that could be beneficial for its industrial applications. Samuel Stupp and Mustafa O. Guler reported peptide amphiphiles (PAs) based nanofiber which exhibits considerable enhancement in hydrolytic rate.<sup>[114]</sup> The advancement of enzyme-inspired catalysts enhances understanding of the sequence-to-structure/function relationships in proteins.<sup>[115]</sup> Peptide self-assembled nanofibers are considered to be promising supramolecular frameworks for constructing artificial enzymes and share basic features as natural proteins.<sup>[116–118]</sup> Furthermore, self-assembled nanofibers through the mediation of non-covalent interactions can create amphiphilic architectures and brings functional groups in close proximity generating additional non-covalent interactions that could contribute towards the enhancement in catalytic rate. Zhimin He *et al.* developed an artificial hydrolytic enzyme by generating the catalytic triad Ser-His-Asp using co-assembly of the peptides into nanofibers (CoAHSD).<sup>[119]</sup> The co-assembled peptide Fmoc-Phe-Phe-His-COOH (Fmoc-FFH), Fmoc-Phe-Phe-Ser-COOH (Fmoc-FFS), and Fmoc-Phe-Phe-Asp-COOH (Fmoc-FFD) at a ratio of 40:1:1 resulted in nanofibers exhibited improved hydrolase-like activity and selectivity toward *p*-NPA.

Chunqiu Zhang *et al.* explored a variety of self-assembled peptide nanofibers towards ester hydrolysis (Scheme 1.13).<sup>[120]</sup> The catalytic sites embedded in a matrix of peptide self-assembled nanofibers showed much higher catalytic efficiency than the peptide

nanofibers without the catalytic sites, revealing the significance of well-ordered nanostructures in designing new artificial enzymes.

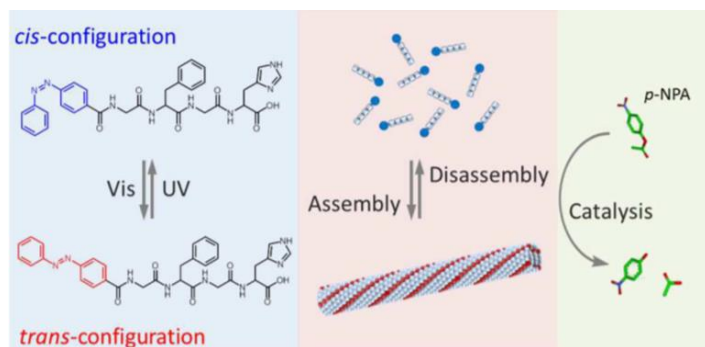


**Scheme 1.13.** Peptide fiber-based hydrolytic enzyme mimics. The well-ordered amphiphilic nanofiber exposed with serine and aspartate residues synergistically contributes to the enhancement in catalytic activity shown by Zhang *et al.* (Reprinted with permission from reference<sup>[120]</sup>. Copyright 2016, American Chemical Society).

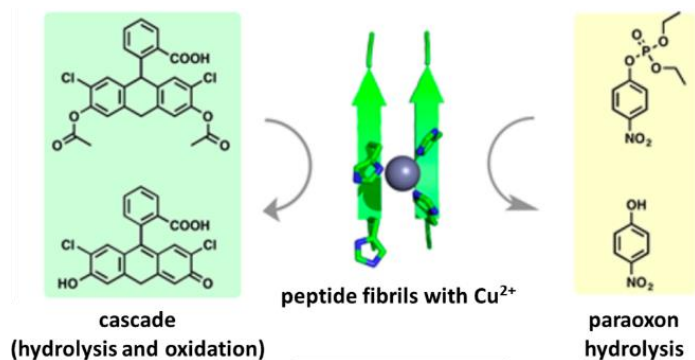
M. P. Friedmann *et al.* have amenable to high-throughput methodologies that allowed to find several peptides and peptide mixtures with their higher stability in a wide range of conditions and their potential as catalysts with low sequence specificity.<sup>[121]</sup> Derek N. Woolfson *et al.* designed stable heptameric  $\alpha$ -helical barrel protein containing seven Cys-His-Glu catalytic triad combinations that showed good advancement in the hydrolytic rates.<sup>[122]</sup>

Wang, Qi and co-workers designed catalytic histidine tethered self-assembled peptide fibers containing photoresponsive azobenzene moiety capable of *cis-trans* isomerization.<sup>[123]</sup> On exposure to light, the change in the stereo configuration of the azobenzene moiety trigger assembly/disassembly of the peptide molecules, thus present an *on-off* behavior to the hydrolytic activity (Scheme 1.14).

H. Christopher Fry *et al.* designed an artificial peroxidase with adjustable catalytic activity by controlling the peptide sequence and supramolecular structure of assemblies.<sup>[124]</sup> Ivan V. Korendovych *et al.* have shown that catalytic amyloids can efficiently hydrolyze paraoxon, a toxic organophosphate pesticide (Scheme 1.15). Finally, functional catalytic amyloids based self-assembled fibrils promote tandem hydrolysis/oxidation reactions.<sup>[125]</sup>



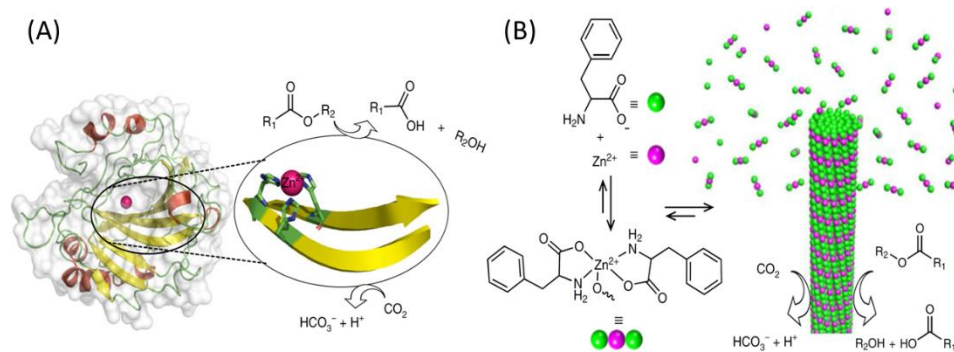
**Scheme 1.14.** A representative scheme showing the photo-mediated *cis-trans* isomerization of the azobenzene anchored peptide. Assembled nanotubes show catalytic on-off behavior as shown by Wang, Qi and co-workers. (Reprinted with permission from reference<sup>[123]</sup>. Copyright 2018, Royal Society of Chemistry).



**Scheme 1.15.** A representative catalysis scheme in the presence of Cu(II) mediated peptide nanofibers shown by Ivan V. Korendovych *et al.* (Reprinted with permission from reference<sup>[125]</sup>. Copyright 2018, Catalysis, American Chemical Society).

The proficiency to orient catalytic groups within an appropriate binding pocket to achieve selective substrate catalysis has also been demonstrated by Gorin and coworkers.<sup>[126]</sup> They immobilized catalytic imidazole moiety with DNA aptamer which acts as a substrate recognition domain, thus enable selective substrate catalysis.

Recently, Ehud Gazit *et al.* have shown the ability of a single amino acid phenylalanine molecules coordinate with zinc ions self-assemble to form a robust, layered, supramolecular amyloid-like ordered architecture that exhibits remarkable carbonic anhydrase-like catalytic activity (Scheme 1.16).<sup>[127]</sup>



**Scheme 1.16.** A) The structure of human carboxy anhydrase CA II, which shows a zinc-coordinated at the catalytic center synergistically triggers the hydrolytic catalysis. B) Chemical structure of phenylalanine complexed with Zn(II) ions act a minimalistic catalyst, shown by Gazit *et al.* (Reprinted with permission from reference<sup>[127]</sup>. Copyright 2019, Nature Catalysis).

Several reports have shown that the ability of self-assembled peptidic architecture to promote catalysis is not-limited to hydrolytic reactions. Beatriu Escuder *et al.* developed proline-containing peptide assemblies for an enantioselective aldol reaction.<sup>[128]</sup> Dibyendu Das *et al.* demonstrated a catalytic potential of short peptide-based cross- $\beta$  amyloid nanotubes with surface-exposed histidine that have been shown to be capable of binding with hemin and showing facile cascade reactions playing the dual roles of hydrolase and peroxidases, two of the most important enzymes in extant biology.<sup>[129,130]</sup>

While the catalytic effect of a variety of synthetic systems continues to be lagging behind natural enzymes, progress is still being made in creating hydrolase-inspired catalysts by imitating and incorporating specific features as observed in the native protein structures. The development of such enzyme-inspired bio-materials promises more robust and industrially relevant alternatives to enzymatic catalysis, as well as provide deeper insights into the function of native enzymes.

## 1.6. Self-assembled organic-inorganic hybrid, bioactive glass:

Hybrid materials formed by the combination of both organic and inorganic constituents, have recently evolved as an effective and promising class of composites due to the diverse properties. In that regard, bioactive glasses (bioglass, BG) have emerged as a

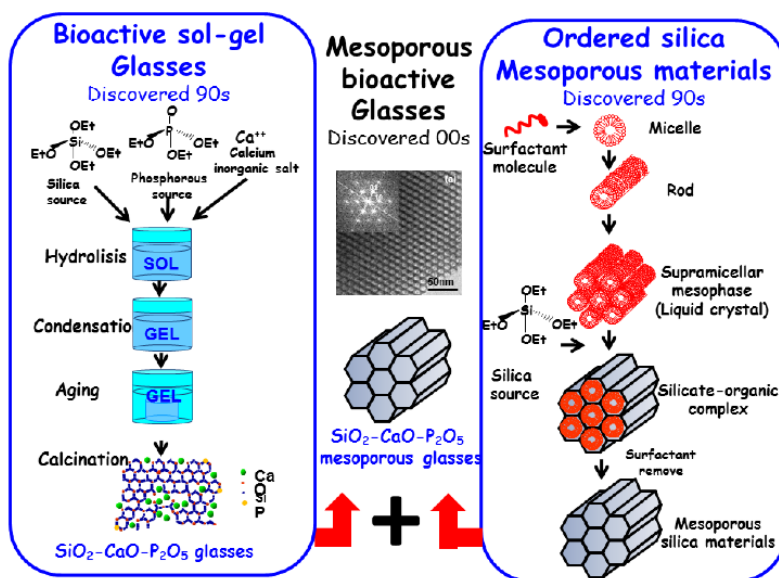
potential composite biomaterial demonstrating interesting applications as bone cementing materials in prosthetic medical implants and drug delivery. Owing to lower silica content (<60%), the BG materials shows interesting bioactivity property thereby, producing different forms of hydroxyapatite (HAp) eventually promotes natural adhesion by means of morphological and biological fixation. A third-generation biomaterial was for the first time accidentally discovered by Larry L. Hench in 1969.<sup>[131–134]</sup> They are well known to elicit a positive response on coming in contact with the biological fluid via the formation of a bone-like apatite layer on its surface along with simultaneous activation of genes for bone regeneration through its constituent ions. Till date, many techniques such as melt-derived, sol-gel method,<sup>[135–137]</sup> double-polymer templating, evaporation-induced self-assembly,<sup>[138]</sup> coaxial electrospinning,<sup>[139]</sup> cathodic electrophoretic deposition<sup>[140]</sup> to direct writing fabrication including robocasting<sup>[141]</sup> and 3D-Printing<sup>[142]</sup> have been widely explored. Several molecules were followed as the templates for the synthesis of bioactive glass such as non-ionic block copolymers<sup>[143–146]</sup> polyurethane sponge,<sup>[147]</sup> polystyrene, polyester,<sup>[148]</sup> and ionic surfactant.<sup>[146,149]</sup> Only limited biotemplates have been reported to direct the synthesis of bioactive glass such as natural mediterranean sea sponge.<sup>[150]</sup>

The techniques discussed above suffer from various individual shortcomings. Isabel Izquierdo-Barba and María Vallet-Regí demonstrated that the mesoporous bioactive glasses (MBGs) establish a new generation of nanostructured bioceramics with exceptional bioactivity in comparison to the conventional bioactive glasses such as melt and sol-gel method based bioactive glasses (Scheme 1.17). Although the mesoporous bioactive materials possess compositional similarity towards the conventional sol-gel bioactive glasses, the MBGs possess enhanced *in vitro* bioactivity owing to their high surface area and pore volume than conventional ones.<sup>[151]</sup>

Bioactive glass nanofibers derived from the electro-spinning process degrade rapidly to hydroxyapatite; thus, they are useful only in the healing of soft tissues. After the electrospinning step, the nanofibrous scaffold has to always pass through thermal treatment in order to decompose residual organic or inorganic groups. Bio-inspired methodology comprises of few simple, eco-friendly procedures along with the omission for



calcination.<sup>[152,153]</sup> Organic molecules based templates are chosen as they are well known to retain their originality and to induce crystallization of inorganic molecules from the solution phase in ambient conditions. Thus, it helps to achieve superior textural properties at ambient conditions.<sup>[152]</sup> Herein, self-organization and directed assembly of biological macromolecule based templates helps in the creation of hierarchical nanostructured materials as found in



**Scheme 1.17.** A representative scheme elucidating the synthesis of mesoporous bioactive glasses using the combination of sol-gel and silica mesoporous materials, shown by Isabel Izquierdo-Barba and María Vallet-Regí. (Reprinted with permission from reference<sup>[150]</sup>. Copyright 2015, American Chemical Society).

nature.<sup>[154–157]</sup> Recently, synthesis of third-generation bioactive glass materials using organic templates such as dendrimer, CTAB, cellulose, gelatin as a template at ambient conditions have been shown.<sup>[158–160]</sup> However, the degradability of such scaffolds remains an issue as they are difficult to resorb and eventually forms a hybrid material with bone resulting in loss of dynamic nature of bone tissues. Such challenges with the sustainable healing ability of bones along with a reduction in the requirement of exogenous osteogenic factors can be circumvented by using supramolecular constructs as a template for bioglass materials that degrades and resorb completely over time only to be replaced by pure bone tissues.

Interestingly, peptide amphiphile templated hydroxyapatite and calcium phosphate mineralization<sup>[161–164]</sup> have found its relevance owing to its structural analogy with collagen

template mineralization in tendon and ligaments. However, the literature lacks in evaluating supramolecular scaffolds as a template for the bioactive glass synthesis.

### **1.7. Scope of Research:**

There are ample opportunities to design supramolecular self-assembled networks in a judicious manner followed by imparting functional characteristics that may already be a leap forward from the serendipitous discovery of self-assembled structures, as has been the trend till the last decade.

In this regard, Chapter 2 is devoted to the self-assembly of single amino acids based hydrogel which possesses stimuli-responsive behavior. The designed hydrogel circumvented a long procedure for the synthesis of peptide amphiphiles to result in hydrogels.

Chapter 3 demonstrates the self-assembly of short peptide fragments inspired by amyloid nucleating core in an aqueous medium. This may act as a model system to study kinetically and thermodynamically controlled living supramolecular polymerization and seeded supramolecular polymerization in water. The formation of metastable nanoparticles is governed by low temperature and solvent mixture which eventually produces kinetically controlled nanofibers and thermodynamically stable twisted helical bundles. Introducing short nanofiber seeds to the metastable nanoparticles allows access to kinetic nanofibers with excellent length control. To the best of my knowledge, it was the first system where the native amyloid short peptide is studied for self-assembly under kinetic and thermodynamic conditions to have supramolecular polymerization in an aqueous medium.

In chapter 4, short amyloid peptide-based self-assembled pathway-dependent divergent nanostructures are discussed in detail and were employed to mimic the hydrolytic catalysis.

In chapter 5, a successful attempt has been made for the first time using bio-inspired peptide-based nanostructures as a template for the formation of bioactive glass composite at ambient conditions without compromising the mechanical strength and bioactivity. Moreover, the tuned morphological variations in bioactive glass are discussed in detail. It

was found that the collagen mimicking twisted bundle morphology was a promising template for the formation of BG with increased mechanical strength.

## 1.8. References:

- [1] H. B. D. Staudinger, "Hermann Staudinger Foundation of Polymer Science - Landmark - American Chemical Society," **1920**.
- [2] W. H. Carothers, *Chem. Rev.* **1931**, 8, 353.
- [3] J. M. Lehn, *Polym. Int.* **2002**, 51, 825.
- [4] G. Armstrong, M. Buggy, *J. Mater. Sci.* **2005**, 40, 547.
- [5] A. Harada, A. Hashidzume, Y. Takashima, *Adv. Polym. Sci.* **2006**, 201, 1.
- [6] A. Ciferri, *J. Macromol. Sci. Part C Polym. Rev.* **2003**, 43, 271.
- [7] G. Ten Brinke, J. Ruokolainen, O. Ikkala, *Adv. Polym. Sci.* **2007**, 207, 113.
- [8] L. Bouteiller, *Adv. Polym. Sci.* **2007**, 207, 79.
- [9] L. S. Shimizu, *Polym. Int.* **2007**, 56, 444.
- [10] M. Szwarc, M. Levy, R. Milkovich, *J. Am. Chem. Soc.* **1956**, 78, 2656.
- [11] G. Odian, F. Group, *Principles of Polymerization, 4th Edition*, **2004**.
- [12] O. W. WEBSTER, *Science (80-. )*. **1991**, 251, 887.
- [13] J. J. L. M. Cornelissen, M. Fischer, N. A. J. M. Sommerdijk, R. J. M. Nolte, *Science (80-. )*. **1998**, 280, 1427.
- [14] J. Ruokolainen, R. Mäkinen, M. Torkkeli, T. Mäkelä, R. Serimaa, G. Ten Brinke, O. Ikkala, *Science (80-. )*. **1998**, 280, 557.
- [15] H. Cui, Z. Chen, S. Zhong, K. L. Wooley, D. J. Pochan, *Science* **2007**, 317, 647.
- [16] D. J. Pochan, Z. Chen, H. Cui, K. Hales, K. Qi, K. L. Wooley, *Science* **2004**, 306, 94.
- [17] V. Percec, A. E. Dulcey, V. S. K. Balagurusamy, Y. Miura, J. Smidrkal, M. Peterca, S. Hummelin, U. Edlund, S. D. Hudson, P. A. Heiney, H. Duan, S. N. Magonev, S. A. Vinogradov, *Nature* **2004**, 430, 764.
- [18] M. Weck, *Polym. Int.* **2007**, 56, 453.
- [19] C. Tang, E. M. Lennon, G. H. Fredrickson, E. J. Kramer, C. J. Hawker, *Science* **2008**, 322, 429.
- [20] X. Wang, G. Guerin, H. Wang, Y. Wang, I. Manners, M. A. Winnik, *Science* **2007**, 317, 644.
- [21] K. E. Feldman, M. J. Kade, T. F. A. De Greef, E. W. Meijer, E. J. Kramer, C. J. Hawker, *Macromolecules* **2008**, 41, 4694.
- [22] J. B. Gilroy, T. Gädt, G. R. Whittell, L. Chabanne, J. M. Mitchels, R. M. Richardson, M. A. Winnik, I. Manners, *Nat. Chem.* **2010**, 2, 566.
- [23] S. K. Patra, R. Ahmed, G. R. Whittell, D. J. Lunn, E. L. Dunphy, M. A. Winnik, I. Manners, *J. Am. Chem. Soc.* **2011**, 133, 8842.
- [24] H. Qiu, G. Russo, P. A. Rugar, L. Chabanne, M. A. Winnik, I. Manners, *Angew. Chemie. Int. Ed.* **2012**, 51, 11882.
- [25] P. A. Rugar, L. Chabanne, M. A. Winnik, I. Manners, *Science* **2012**, 337, 559.
- [26] Z. M. Hudson, C. E. Boott, M. E. Robinson, P. A. Rugar, M. A. Winnik, I. Manners,

- Nat. Chem.* **2014**, *6*, 893.
- [27] W. Zhang, W. Jin, T. Fukushima, A. Saeki, S. Seki, T. Aida, *Science* **2011**, *334*, 340.
- [28] L. Brunsveld, B. J. B. Folmer, E. W. Meijer, R. P. Sijbesma, *Chem. Rev.* **2001**, *101*, 4071.
- [29] T. Aida, E. W. Meijer, S. I. Stupp, *Science* **2012**, *335*, 813.
- [30] C. Rest, R. Kandanelli, G. Fernández, *Chem. Soc. Rev.* **2015**, *44*, 2543.
- [31] P. A. Korevaar, S. J. George, A. J. Markvoort, M. M. J. Smulders, P. A. J. Hilbers, A. P. H. J. Schenning, T. F. A. De Greef, E. W. Meijer, *Nature* **2012**, *481*, 492.
- [32] P. A. Korevaar, C. J. Newcomb, E. W. Meijer, S. I. Stupp, *J. Am. Chem. Soc.* **2014**, *136*, 8540.
- [33] A. Sorrenti, J. Leira-Iglesias, A. J. Markvoort, T. F. A. De Greef, T. M. Hermans, *Chem. Soc. Rev.* **2017**, *46*, 5476.
- [34] J. S. Valera, R. Gómez, L. Sánchez, *Small* **2018**, *14*, 1870012.
- [35] E. Mattia, S. Otto, *Nat. Nanotechnol.* **2015**, *10*, 111.
- [36] S. Ogi, K. Sugiyasu, S. Manna, S. Samitsu, M. Takeuchi, *Nat. Chem.* **2014**, *6*, 188.
- [37] S. Ogi, V. Stepanenko, K. Sugiyasu, M. Takeuchi, F. Würthner, *J. Am. Chem. Soc.* **2015**, *137*, 3300.
- [38] S. Ogi, V. Stepanenko, J. Thein, F. Würthner, *J. Am. Chem. Soc.* **2016**, *138*, 670.
- [39] T. Fukui, S. Kawai, S. Fujinuma, Y. Matsushita, T. Yasuda, T. Sakurai, S. Seki, M. Takeuchi, K. Sugiyasu, *Nat. Chem.* **2017**, *9*, 493.
- [40] W. Wagner, M. Wehner, V. Stepanenko, S. Ogi, F. Würthner, *Angew. Chemie - Int. Ed.* **2017**, *56*, 16008.
- [41] J. Kang, D. Miyajima, Y. Itoh, T. Mori, H. Tanaka, M. Yamauchi, Y. Inoue, S. Harada, T. Aida, *J. Am. Chem. Soc.* **2014**, *136*, 10640.
- [42] J. Kang, D. Miyajima, T. Mori, Y. Inoue, Y. Itoh, T. Aida, *Science* **2015**, *347*, 646.
- [43] M. Endo, T. Fukui, S. H. Jung, S. Yagai, M. Takeuchi, K. Sugiyasu, *J. Am. Chem. Soc.* **2016**, *138*, 14347.
- [44] A. Pal, M. Malakoutikhah, G. Leonetti, M. Tezcan, M. Colomb-Delsuc, V. D. Nguyen, J. van der Gucht, S. Otto, *Angew. Chemie Int. Ed.* **2015**, *54*, 7852.
- [45] S. Ogi, K. Matsumoto, S. Yamaguchi, *Angew. Chemie Int. Ed.* **2018**, *57*, 2339.
- [46] D. S. Pal, H. Kar, S. Ghosh, *Chem. Commun.* **2018**, *54*, 928.
- [47] G. Ghosh, P. Dey, S. Ghosh, *Chem. Commun.* **2020**, DOI 10.1039/d0cc02787a.
- [48] F. Chiti, C. M. Dobson, *Annu. Rev. Biochem.* **2006**, *75*, 333.
- [49] I. W. Hamley, *Chem. Rev.* **2012**, *112*, 5147.
- [50] P. N. Cheng, C. Liu, M. Zhao, D. Eisenberg, J. S. Nowick, *Nat. Chem.* **2012**, *4*, 927.
- [51] I. V. Baskakov, G. Legname, M. A. Baldwin, S. B. Prusiner, F. E. Cohen, *J. Biol. Chem.* **2002**, *277*, 21140.
- [52] G. M. Whitesides, J. P. Mathias, C. T. Seto, *Science* **1991**, *254*, 1312.
- [53] D. Mandal, A. Nasrolahi Shirazi, K. Parang, *Org. Biomol. Chem.* **2014**, *12*, 3544.
- [54] M. P. Hendricks, K. Sato, L. C. Palmer, S. I. Stupp, *Acc. Chem. Res.* **2017**, *50*, 2440.
- [55] K. Sato, W. Ji, L. C. Palmer, B. Weber, M. Barz, S. I. Stupp, *J. Am. Chem. Soc.* **2017**, *139*, 8995.
- [56] C. M. Berac, L. Zengerling, D. Straßburger, R. Otter, M. Urschbach, P. Besenius, *Macromol. Rapid Commun.* **2020**, *41*, 1900476.

- [57] A. Sarkar, J. C. Kölsch, C. M. Berač, A. Venugopal, R. Sasmal, R. Otter, P. Besenius, S. J. George, *ChemistryOpen* **2020**, *9*, 346.
- [58] C. Pappas, N. Wijerathne, J. K. Sahoo, A. Jain, D. Kroiss, I. R. Sasselli, A. Pina, A. Lampel, R. V Ulijn, **n.d.**, DOI 10.26434/chemrxiv.11637312.v1.
- [59] T. Kar, S. Debnath, D. Das, A. Shome, P. K. Das, *Langmuir* **2009**, *25*, 8639.
- [60] S. Debnath, A. Shome, D. Das, P. K. Das, *J. Phys. Chem. B* **2010**, *114*, 4407.
- [61] X. Du, J. Zhou, J. Shi, B. Xu, *Chem. Rev.* **2015**, *115*, 13165.
- [62] A. Sharma, A. Gupta, N. Khan, A. DuttKonar, *New J. Chem.* **2020**, DOI 10.1039/d0nj01583k.
- [63] Z. Yang, K. Xu, L. Wang, H. Gu, H. Wei, M. Zhang, B. Xu, *Chem. Commun.* **2005**, 4414.
- [64] Y. Loo, Y. C. Wong, E. Z. Cai, C. H. Ang, A. Raju, A. Lakshmanan, A. G. Koh, H. J. Zhou, T. C. Lim, S. M. Moochhala, C. A. E. Hauser, *Biomaterials* **2014**, *35*, 4805.
- [65] Y. Wan, L. Liu, S. Yuan, J. Sun, Z. Li, *Langmuir* **2017**, *33*, 3234.
- [66] M. Lian, X. Chen, Y. Lu, W. Yang, *ACS Appl. Mater. Interfaces* **2016**, *8*, 25036.
- [67] S. D. Bhagat, A. Srivastava, *CrystEngComm* **2016**, *18*, 4369.
- [68] D. J. Pochan, J. P. Schneider, J. Kretsinger, B. Ozbas, K. Rajagopal, L. Haines, *J. Am. Chem. Soc.* **2003**, *125*, 11802.
- [69] K. Malhotra, S. Shankar, N. Chauhan, R. Rai, Y. Singh, *Mater. Sci. Eng. C* **2020**, *110*, 110648.
- [70] R. Otter, C. M. Berac, S. Seiffert, P. Besenius, *Eur. Polym. J.* **2019**, *110*, 90.
- [71] A. Baral, S. Roy, A. Dehsorkhi, I. W. Hamley, S. Mohapatra, S. Ghosh, A. Banerjee, *Langmuir* **2014**, *30*, 929.
- [72] S. Basak, J. Nanda, A. Banerjee, *Chem. Commun.* **2014**, *50*, 2356.
- [73] J. Nanda, A. Biswas, A. Banerjee, *Soft Matter* **2013**, *9*, 4198.
- [74] A. Danchin, *Biochimie* **1993**, *75*, 501.
- [75] D. C. Whitcomb, M. E. Lowe, *Dig. Dis. Sci.* **2007**, *52*, 1.
- [76] A. Neuberger, K. (Keith) Brocklehurst, *Hydrolytic Enzymes*, Elsevier, **1987**.
- [77] X. S. Puente, L. M. Sánchez, C. M. Overall, C. López-Otín, *Nat. Rev. Genet.* **2003**, *4*, 544.
- [78] R. M. Stroud, *Sci. Am.* **1974**, *231*, 74.
- [79] G. Dodson, A. Wlodawer, *Trends Biochem. Sci.* **1998**, *23*, 347.
- [80] A. R. Buller, C. A. Townsend, *Proc. Natl. Acad. Sci. U. S. A.* **2013**, *110*, E653.
- [81] Ö. D. Ekici, M. Paetzel, R. E. Dalbey, *Protein Sci.* **2008**, *17*, 2023.
- [82] D. E. Koshland, *Proc. Natl. Acad. Sci.* **1958**, *44*, 98.
- [83] D. E. Koshland, *The Key-Lock Theory and the Induced Fit Theory*, **n.d.**
- [84] E. Fischer, *Berichte der Dtsch. Chem. Gesellschaft* **1894**, *27*, 3479.
- [85] K. Fodor, V. Harmat, R. Neutze, L. Szilágyi, L. Gráf, G. Katona, *Biochemistry* **2006**, *45*, 2114.
- [86] A. Warshel, F. Sussman, *Proc. Natl. Acad. Sci. U. S. A.* **1986**, *83*, 3806.
- [87] E. Kuah, S. Toh, J. Yee, Q. Ma, Z. Gao, *Chem. - A Eur. J.* **2016**, *22*, 8404.
- [88] M. Raynal, P. Ballester, A. Vidal-Ferran, P. W. N. M. Van Leeuwen, *Chem. Soc. Rev.* **2014**, *43*, 1734.
- [89] T. R. Simmons, G. Berggren, M. Bacchi, M. Fontecave, V. Artero, *Coord. Chem. Rev.*

2014, 270–271, 127.

- [90] R. Ragg, M. N. Tahir, W. Tremel, *Eur. J. Inorg. Chem.* **2016**, 2016, 1906.
- [91] G. Wulff, *Chem. Rev.* **2002**, 102, 1.
- [92] X. Zhang, K. N. Houk, *Acc. Chem. Res.* **2005**, 38, 379.
- [93] R. Wieczorek, K. Adamala, T. Gasperi, F. Polticelli, P. Stano, *Life* **2017**, 7, DOI 10.3390/life7020019.
- [94] Y. Maeda, N. Javid, K. Duncan, L. Birchall, K. F. Gibson, D. Cannon, Y. Kanetsuki, C. Knapp, T. Tuttle, R. V. Ulijn, H. Matsui, *J. Am. Chem. Soc.* **2014**, 136, 15893.
- [95] Y. Li, Y. Zhao, S. Hatfield, R. Wan, Q. Zhu, X. Li, M. McMills, Y. Ma, J. Li, K. L. Brown, *Bioorg. Med. Chem.* **2000**, 8, 2675.
- [96] A. J. Camden, S. M. Walsh, S. H. Suk, S. K. Silverman, *Biochemistry* **2016**, 55, 2671.
- [97] Y. Lee, P. C. Klauser, B. M. Brandsen, C. Zhou, X. Li, S. K. Silverman, *J. Am. Chem. Soc.* **2017**, 139, 255.
- [98] Y. Wu, D. Wang, I. Willner, Y. Tian, L. Jiang, *Angew. Chemie - Int. Ed.* **2018**, 57, 7790.
- [99] K. Fan, H. Wang, J. Xi, Q. Liu, X. Meng, D. Duan, L. Gao, X. Yan, *Chem. Commun.* **2017**, 53, 424.
- [100] A. A. Vernekar, T. Das, S. Ghosh, G. Mugesh, *Chem. - An Asian J.* **2016**, 11, 72.
- [101] Y. Huang, M. Zhao, S. Han, Z. Lai, J. Yang, C. Tan, Q. Ma, Q. Lu, J. Chen, X. Zhang, Z. Zhang, B. Li, B. Chen, Y. Zong, H. Zhang, *Adv. Mater.* **2017**, 29, DOI 10.1002/adma.201700102.
- [102] Y. Wang, Y. Zhu, A. Binyam, M. Liu, Y. Wu, F. Li, *Biosens. Bioelectron.* **2016**, 86, 432.
- [103] B. Zhang, R. Breslow, *J. Am. Chem. Soc.* **1997**, 119, 1676.
- [104] Y. Zhao, Y. Huang, H. Zhu, Q. Zhu, Y. Xia, *J. Am. Chem. Soc.* **2016**, 138, 16645.
- [105] M. Grzelczak, J. Vermant, E. M. Furst, L. M. Liz-Marzán, *ACS Nano* **2010**, 4, 3591.
- [106] M. Zhu, M. Wang, W. Qi, R. Su, Z. He, *J. Mater. Chem. B* **2019**, 7, 3804.
- [107] J. Kong, Y. Wang, J. Zhang, W. Qi, R. Su, Z. He, *Angew. Chemie - Int. Ed.* **2018**, 57, 14032.
- [108] M. Vestergaard, T. Hamada, M. Takagi, *Biotechnol. Bioeng.* **2008**, 99, 753.
- [109] A. Lakshmanan, S. Zhang, C. A. E. Hauser, *Trends Biotechnol.* **2012**, 30, 155.
- [110] Y. Jin, X.-D. Xu, C.-S. Chen, S.-X. Cheng, X.-Z. Zhang, R.-X. Zhuo, *Macromol. Rapid Commun.* **2008**, 29, 1726.
- [111] Z. Huang, S. Guan, Y. Wang, G. Shi, L. Cao, Y. Gao, Z. Dong, J. Xu, Q. Luo, J. Liu, *J. Mater. Chem. B* **2013**, 1, 2297.
- [112] M. Reches, E. Gazit, *Science* **2003**, 300, 625.
- [113] B. Lewandowski, H. W. *Current opinion in chemical biology*, 2014, Elsevier.
- [114] M. O. Guler, S. I. Stupp, *J. Am. Chem. Soc.* **2007**, 129, 12082.
- [115] N. Singh, M. Kumar, J. F. Miravet, R. V. Ulijn, B. Escuder, *Chem. - A Eur. J.* **2017**, 23, 981.
- [116] Z. Dong, Yongguo Wang, Y. Yin, J. Liu, *Curr. Opin. Colloid Interface Sci.* **2011**, 16, 451.
- [117] V. Köhler, Y. M. Wilson, M. Dürrenberger, D. Ghislieri, E. Churakova, T. Quinto, L. Knörr, D. Häussinger, F. Hollmann, N. J. Turner, T. R. Ward, *Nat. Chem.* **2013**, 5, 93.

- [118] F. Pu, J. Ren, X. Qu, *Chem. Soc. Rev.* **2018**, *47*, 1285.
- [119] M. Wang, Y. Lv, X. Liu, W. Qi, R. Su, Z. He, *ACS Appl. Mater. Interfaces* **2016**, *8*, 14133.
- [120] C. Zhang, X. Xue, Q. Luo, Y. Li, K. Yang, X. Zhuang, Y. Jiang, J. Zhang, J. Liu, G. Zou, X. J. Liang, *ACS Nano* **2014**, *8*, 11715.
- [121] M. P. Friedmann, V. Torbeev, V. Zelenay, A. Sobol, J. Greenwald, R. Riek, *PLoS One* **2015**, *10*, e0143948.
- [122] A. J. Burton, A. R. Thomson, W. M. Dawson, R. L. Brady, D. N. Woolfson, *Nat. Chem.* **2016**, *8*, 837.
- [123] Y. Zhao, B. Lei, M. Wang, S. Wu, W. Qi, R. Su, Z. He, *J. Mater. Chem. B* **2018**, *6*, 2444.
- [124] L. A. Solomon, J. B. Kronenberg, H. C. Fry, *J. Am. Chem. Soc.* **2017**, *139*, 8497.
- [125] Z. Lengyel, C. M. Rufo, Y. S. Moroz, O. V. Makhlynets, I. V. Korendovych, *ACS Catal.* **2018**, *8*, 59.
- [126] M. Flanagan, A. Arguello, D. Colman, ... J. K.-C., undefined 2018, *pubs.rsc.org* **n.d.**
- [127] P. Makam, S. S. R. K. C. Yamijala, K. Tao, L. J. W. Shimon, D. S. Eisenberg, M. R. Sawaya, B. M. Wong, E. Gazit, *Nat. Catal.* **2019**, *2*, 977.
- [128] C. Berdugo, J. F. Miravet, B. Escuder, *Chem. Commun.* **2013**, *49*, 10608.
- [129] A. Chatterjee, S. P. Afrose, S. Ahmed, A. Venugopal, D. Das, *Chem. Commun.* **2020**, DOI 10.1039/d0cc00279h.
- [130] S. Bal, K. Das, S. Ahmed, D. Das, *Angew. Chemie - Int. Ed.* **2019**, *58*, 244.
- [131] L. L. Hench, R. J. Splinter, W. C. Allen, T. K. Greenlee, *J. Biomed. Mater. Res.* **1971**, *5*, 117.
- [132] L. L. Hench, in *J. Mater. Sci. Mater. Med.*, J Mater Sci Mater Med, **2006**, pp. 967–978.
- [133] L. L. Hench, *J. Am. Ceram. Soc.* **1998**, *81*, 1705.
- [134] L. L. Hench, J. Wilson, *Science.* **1984**, *226*, 630.
- [135] R. Li, A. E. Clark, L. L. Hench, *J. Appl. Biomater.* **1991**, *2*, 231.
- [136] G. Poologasundarampillai, P. D. Lee, C. Lam, A. M. Kourkouta, J. R. Jones, *Int. J. Appl. Glas. Sci.* **2016**, *7*, 229.
- [137] S. L. Greasley, S. J. Page, S. Sirovica, S. Chen, R. A. Martin, A. Riveiro, J. V. Hanna, A. E. Porter, J. R. Jones, *J. Colloid Interface Sci.* **2016**, *469*, 213.
- [138] X. Yan, C. Yu, X. Zhou, J. Tang, D. Zhao, *Angew. Chemie. Int. Ed.* **2004**, *43*, 5980.
- [139] Y. Z. Zhang, X. Wang, Y. Feng, J. Li, C. T. Lim, S. Ramakrishna, *Biomacromolecules* **2006**, *7*, 1049.
- [140] K. D. Patel, A. El-Fiqi, H. Y. Lee, R. K. Singh, D. A. Kim, H. H. Lee, H. W. Kim, *J. Mater. Chem.* **2012**, *22*, 24945.
- [141] S. Eqtesadi, A. Motealleh, P. Miranda, A. Lemos, A. Rebelo, J. M. F. Ferreira, *Mater. Lett.* **2013**, *93*, 68.
- [142] C. Wu, Y. Luo, G. Cuniberti, Y. Xiao, M. Gelinsky, *Acta Biomater.* **2011**, *7*, 2644.
- [143] P. Fabbri, V. Cannillo, A. Sola, A. Dorigato, F. Chiellini, *Compos. Sci. Technol.* **2010**, *70*, 1869.
- [144] M. N. Rahaman, D. E. Day, B. Sonny Bal, Q. Fu, S. B. Jung, L. F. Bonewald, A. P. Tomsia, *Acta Biomater.* **2011**, *7*, 2355.

- [145] H. S. Yun, S. E. Kim, Y. T. Hyeon, *Chem. Commun.* **2007**, 2139.
- [146] Y. Deng, X. Li, Q. Li, *Ind. Eng. Chem. Res.* **2009**, *48*, 8829.
- [147] Y. Zhu, C. Wu, Y. Ramaswamy, E. Kockrick, P. Simon, S. Kaskel, H. Zreiqat, *Microporous Mesoporous Mater.* **2008**, *112*, 494.
- [148] G. Wei, X. Yan, J. Yi, L. Zhao, L. Zhou, Y. Wang, C. Yu, *Microporous Mesoporous Mater.* **2011**, *143*, 157.
- [149] H. suk Yun, S. hyun Kim, S. Lee, I. hyuck Song, *Mater. Lett.* **2010**, *64*, 1850.
- [150] H. Wang, X. Gao, Y. Wang, J. Tang, C. Sun, X. Deng, X. Niu, *Mater. Lett.* **2012**, *76*, 237.
- [151] I. Izquierdo-Barba, M. Vallet-Regi, *Biomed. Glas.* **2015**, *1*, 140.
- [152] D. Santhiya, H. K. Alajangi, F. Anjum, S. Murugavel, M. Ganguli, *J. Mater. Chem. B* **2013**, *1*, 6329.
- [153] L. P. Bauermann, J. Bill, F. Aldinger, *J. Phys. Chem. B* **2006**, *110*, 5182.
- [154] H. Cölfen, S. Mann, *Angew. Chemie - Int. Ed.* **2003**, *42*, 2350.
- [155] P. Fratzl, *J. R. Soc. Interface* **2007**, *4*, 637.
- [156] M. Hildebrand, B. E. Volcani, W. Gassmann, J. I. Schroeder, *Nature* **1997**, *385*, 688.
- [157] D. J. Belton, O. Deschaume, C. C. Perry, *FEBS J.* **2012**, *279*, 1710.
- [158] N. Gupta, D. Santhiya, A. Aditya, K. Badra, *RSC Adv.* **2015**, *5*, 56794.
- [159] N. Gupta, D. Santhiya, *Mater. Lett.* **2017**, *188*, 127.
- [160] N. Gupta, D. Santhiya, *Mater. Sci. Eng. C* **2017**, *75*, 1206.
- [161] L. C. Palmer, C. J. Newcomb, S. R. Kaltz, E. D. Spörke, S. I. Stupp, *Chem. Rev.* **2008**, *108*, 4754.
- [162] S. Segman-Magidovich, H. Grisar, T. Gitli, Y. Levi-Kalisman, H. Rapaport, *Adv. Mater.* **2008**, *20*, 2156.
- [163] S. S. Lee, B. J. Huang, S. R. Kaltz, S. Sur, C. J. Newcomb, S. R. Stock, R. N. Shah, S. I. Stupp, *Biomaterials* **2013**, *34*, 452.
- [164] R. J. Mart, R. D. Osborne, M. M. Stevens, R. V. Ulijn, *Soft Matter* **2006**, *2*, 822.



## Chapter 2

# Chirality control to multi-stimuli responsive and self-healing supramolecular metallo-hydrogels

*In this chapter, a metallo-hydrogel based on chiral amino acid, histidine and  $Zn^{2+}$  ions is designed using coordination driven self-assembly. The hydrogel formation was instantaneous and exhibited stimuli-responsive behaviour with respect to pH, heat and external chemicals. The gelation ability depends on the optical purity and enantiomeric excess of the amino acids. The supramolecular chirality mediated by Zn-Histidine complex and subsequent fiber formation showed sign inversion of CD signal with respect to that of native amino acids (L- or D-) and can be tuned by changing the ratio of two chiral species, L-, D- amino acids. Job's plot from the circular dichroism probing supramolecular chirality confirms 1:1 complex of Zn and histidine. The viscoelastic property and kinetics of the hydrogel could conveniently be tuned by changing its enantiomeric excess (ee%), concentration and the ratio of Zn and histidine. Moreover, the resulting metallo-hydrogel was thixotropic and exhibits instantaneous, intrinsic self-healing behavior.*

### 2.1. Introduction

Stimuli-responsive and self-healing materials have widespread applications in many fields such as sensing, shape memory devices, biomedicine, biomaterials, tissue engineering, pollutant removal, and smart interface materials.<sup>[1-7]</sup> Supramolecular metal-organic gels that result from a combination of various non-covalent interactions<sup>[8-12]</sup> including coordination interaction are envisaged as smart stimuli-responsive and self-healing materials.<sup>[13-15]</sup> Metallogels can be deformed and recovered reversibly in response to external stimuli such as heat, pH variation, the addition of external chemicals and mechanical forces due to the dynamic and reversible nature of metal coordination, leading to gel-sol transition. Such engineered intrinsic self-healing materials are fascinating because they resemble the natural self-healing phenomena as the presence of sacrificial noncovalent interactions plays a

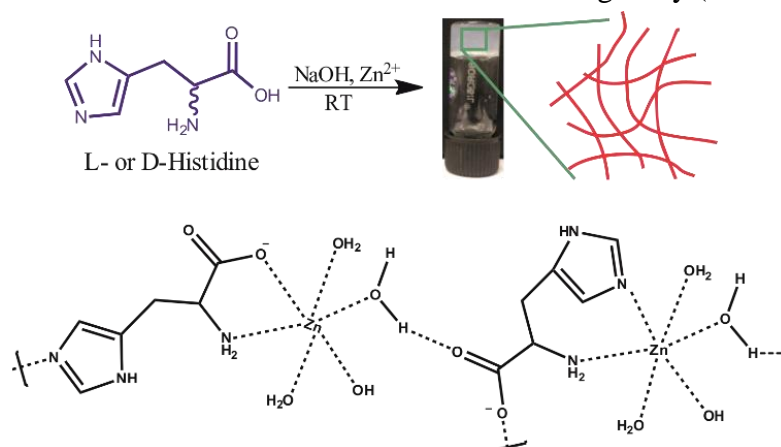
pivotal role by allowing breaking of the material and further reformation for the repair of the damaged material.<sup>[16,17]</sup> The reversible nature of metal coordination bond, endows self-healing property in the metallogels. The generation of metallogels is often tedious and time consuming due to cumbersome synthesis and special requirements for the design of ligands that coordinate with metal ions to form gels.<sup>[18,19]</sup> Furthermore, biological applications of these materials require them to be constructed using benign ligands. Therefore, the use of readily available and economical biomolecules as ligands for the generation of metallogels has been a focal point of gel research. To date, there are only a handful of reports realizing the potential of pure, naturally available, unsubstituted biomolecules to form metallogels.<sup>[20–24]</sup>

Chiral interactions have important applications in biological processes, chemistry, and medicine.<sup>[25–29]</sup> In general, supramolecular chirality refers to the induction of chirality in supramolecular assemblies formed by non-covalent interactions such as hydrogen bonding, metal coordination,  $\pi$ - $\pi$  stacking, *etc.* A preference for a particular supramolecular chirality, e.g., *P* or *M* type can be tuned by the relative proportion of the optically active monomer units.<sup>[30–32]</sup> While, studies on the chirality inversion induced by pH, host-guest interactions, solvent, temperature, anions *etc.* for peptide gelators and large dendritic molecules have been performed,<sup>[20,33–37]</sup> only a few reports on the metal-mediated supramolecular chirality in small molecule self-assembling systems exist.<sup>[38,39]</sup> Furthermore, only a few groups worldwide, have shown the formation of metallogels controlled by ee% of the ligand.<sup>[40]</sup> Also, the stimuli-responsive and self-healing behavior of metallogels constructed using optically pure, unsubstituted biomolecules has not been studied before.

## 2.2. Results and Discussion

The stereo-selective self-assembly of metal-based hydrogel in a single step was performed using naturally occurring, inexpensive, amino acid, histidine with  $\text{Zn}^{2+}$  ions. It is to be noted that although histidine based polymers are known to form gels,<sup>[41–45]</sup> the use of unsubstituted histidine to form metallogels has not been explored yet. Moreover, the resulting hydrogel showed multi-stimuli response towards pH, heat, and additives. Detailed

studies revealed that the properties of the resulted Zn-His hydrogel could be tuned by varying the ee% of the histidine. The hydrogel formation was accompanied by the tunability of the supramolecular chirality with respect to the chiral ligand. The viscoelastic properties and kinetics of the metallogel can be conveniently tuned and the thixotropic results showed excellent self-healing behavior. Mixing an aqueous solution of  $\text{Zn}(\text{NO}_3)_2$  (100 mM) with an alkaline deprotonated solution of histidine ( $\text{pH} \approx 12.3$ ) (100 mM) in a 1:1 molar ratio resulted in self-standing stable Zn-His hydrogel. The formation of the gel was ascertained by inverting the vial which did not allow the mass to flow under gravity (Scheme 2.1).



**Scheme 2.1.** Formation of supramolecular metallo-hydrogel upon the interaction of histidine with  $\text{Zn}^{2+}$  ions in alkaline medium results in nanofibrillar morphology and proposed structure of the complex formed upon the interaction of histidine with  $\text{Zn}^{2+}$  ions.

Instantaneous formation of the metallogel indicates fast coordination kinetics for Zn and Histidine, which resulted in the formation and further crosslinking of the fibers. The formed hydrogel was highly stable as no disruption of the fibrous gel was observed even on keeping the vial inverted for three months or upon bath sonication for 6 h. Moreover, unlike most of the reported metallogels,<sup>[46-48]</sup> this Zn-His coordinated metallogel was spontaneously formed at room temperature without the assistance of any external force such as heating/cooling or sonication.

### 2.2.1. Control over gelation:

Several experiments were performed in order to understand the conditions required for the formation a stable gel. Alkaline pH was a must for the formation of the gels. Sodium

hydroxide was added to make the pH of the histidine solution alkaline which effectively coordinated with Zn salt resulted in fiber morphology entangled to form a stable hydrogel. Upon changing the base from NaOH to NH<sub>4</sub>OH, similar results were obtained. This emphasizes that the base does not affect the process of gelation. However, under neutral conditions, the addition of Zn<sup>2+</sup> ions did not completely coordinate with histidine groups which resulted in a clear free-flowing solution (Figure 2.1) which can be attributed to the protonation of basic nitrogen groups in histidine.<sup>[49]</sup>

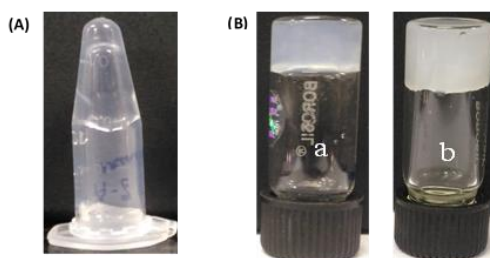


**Figure 2.1.** (A) Digital image of the clear free flowing solution obtained upon the addition of Zn(NO<sub>3</sub>)<sub>2</sub> to an aqueous neutral solution of *L*-histidine. (B) Digital images of the stable hydrogel formed from Zn(NO<sub>3</sub>)<sub>2</sub> and an alkaline solution of *L*-histidine prepared using (a) sodium hydroxide and (b) ammonia solution, showing that change of base does not affect gelation.

The solvent system plays a crucial role in the self-assembly mechanism. The presence of water molecules was critical towards the formation of the gel. The mixture of methanol-water or acetonitrile-water did not result in the proper coordination of Zn-His which led only to the formation of a white precipitate (Figure 2.2). Anions of the metal salts had little effect on the formation of the gel as the change of metal salt from Zn(NO<sub>3</sub>)<sub>2</sub> to ZnCl<sub>2</sub> or Zn(CH<sub>3</sub>COO)<sub>2</sub> also led to the formation of a stable hydrogel. Furthermore, the gelation was found to be specific to histidine and Zn<sup>2+</sup> ions out of a variety of amino acids such as

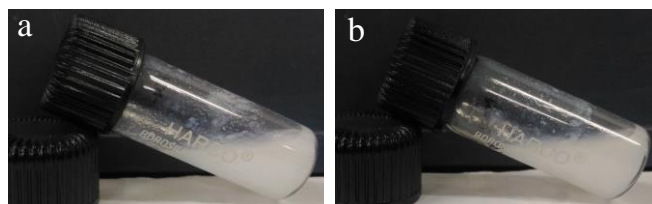


**Figure 2.2.** Digital images of the precipitate obtained upon the addition of Zn(NO<sub>3</sub>)<sub>2</sub> in (a) methanol and (b) acetonitrile to an aqueous alkaline solution of *L*-histidine.

arginine, glutamic acid, and lysine (Figure 2.3). It is imperative to mention that a 1:1 molar ratio of  $Zn^{2+}$  ions and histidine was important for the formation of stable metallogels, as a change in the molar ratio of one of the components led to the formation of clear solutions or weak gels (Table 2.1 & Figure 2.4).

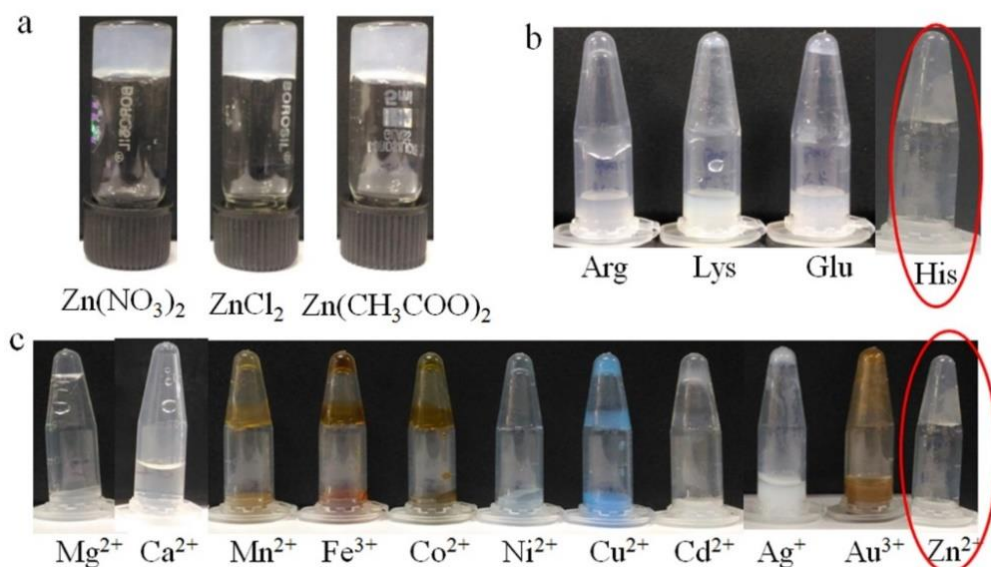


**Figure 2.3.** Digital images showing (a) the formation of stable gels upon changing of metal counter ions, (b) the formation of precipitates upon the interaction of arginine, lysine and glutamic acid with  $Zn^{2+}$  ions and (c) the specificity of  $Zn^{2+}$  ions towards the formation of hydrogel upon interaction with histidine.

**Table 2.1.** Interaction of *L*-histidine with  $Zn^{2+}$  ions with varying molar ratio of metal ion: ligand.

Histidine (M)	$Zn(NO_3)_2$ (M)	Result
0.1	0.1	Stable gel
0.1	0.05	Slightly turbid solution
0.1	0.025	Clear solution
0.1	0.01	Clear solution
0.05	0.1	Weak gel
0.025	0.1	Clear solution
0.01	0.1	Clear solution
0.05	0.05	Stable gel

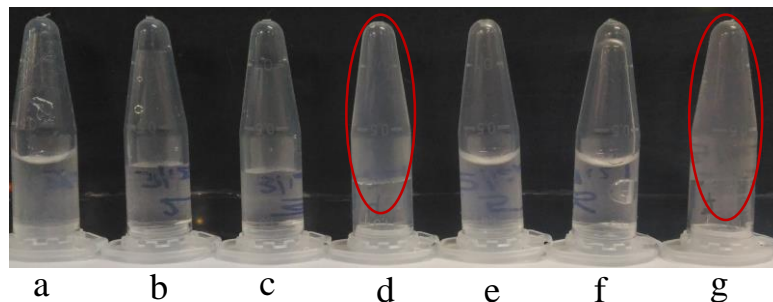


**Figure 2.4.** Digital images of the turbid and clear solutions as well as gels formed with varying molar ratios of *L*-histidine:  $Zn^{2+}$  ions, (a) 0.1M: 0.05M, (b) 0.1M: 0.025M, (c) 0.1M: 0.01M, (d) 0.05M: 0.1M, (e) 0.025M: 0.1M, (f) 0.01M: 0.1M, (g) 0.05M: 0.05M. (Red circles indicate the concentrations at which gel formation occurred).

When there is enough 3D fibrous network that are entangled to each other to hold water molecules, it results in the formation of hydrogel. It was found that the minimum gelation concentrations of histidine with Zn were 15 mM, below which gel formation was not evident (Figure 2.5).

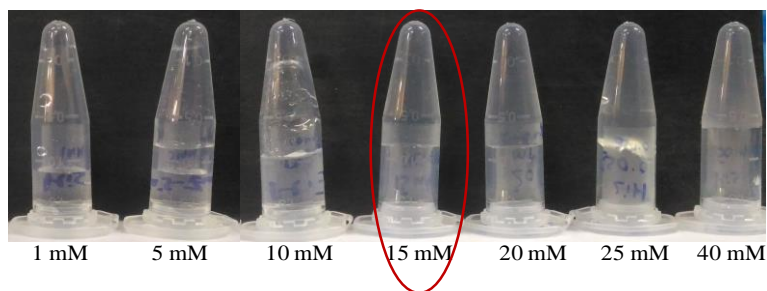


**Figure 2.5.** Digital images showing the interaction of  $Zn^{2+}$  with *L*-histidine at different molar concentrations of the reactants. The minimum gelation concentration was found to be 15 mM.

### 2.2.2. Multi-stimuli response of the hydrogel:

Since metallogels are formed as a result of weak non-covalent interactions that can be modulated upon application of appropriate external stimuli, we next investigated the stimuli-responsive nature of the Zn-His metallogel (Figure 2.6). The addition of a few drops of 1M  $HNO_3$  to the hydrogel led to the collapse of the gel, resulting in a clear solution within a few minutes. Restoration of the gel phase was possible upon the addition of 1M NaOH to the solution to surpass pH 12.5. Similar clear solution formation and gel restoration could

be obtained upon addition of 1M trifluoroacetic acid and 1M ammonia solution respectively. This indicates bond breakage between the histidine and  $Zn^{2+}$  ions upon the addition of acid, which could be reformed upon the addition of a base, leading to the restoration of the gel phase. The pH-responsive reversible gel to sol transition could be repeated several times without any observed change in the gel structure. The Zn-His gel was also found to be thermo-responsive and upon heating at a temperature of 135 °C, the gel was collapsed to give an opaque sol. The recovery to the gel state upon cooling to room temperature was however not observed. Furthermore, the addition of a strong metal-chelating ligand EDTA led to the dissolution of the gel to form a clear solution. This could be attributed to the displacement of histidine by EDTA in the coordination polymer backbone. Similar results (clear solution) were obtained upon the addition of  $Na_2S$  to the hydrogel. Interestingly, it was found that the chirality of histidine also plays an important role in affecting the metallogel formation.

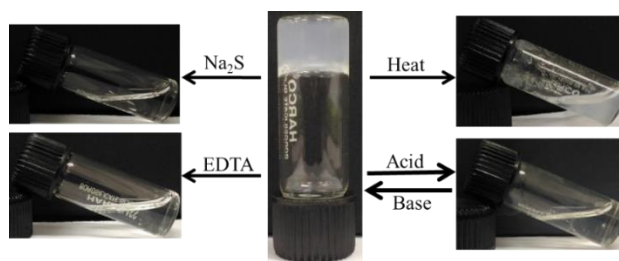


**Figure 2.6** Chemical, thermal, and pH stimuli triggered gel-sol transition of the Zn-His metallogel.

A 100% enantiomeric excess (ee) of *L*- or *D*-histidine led to the formation of a stable metallogel, however, a racemic mixture of the ligands only led to the formation of a turbid sol (Figure 2.7). The ee% of histidine was then varied and it was observed that with an

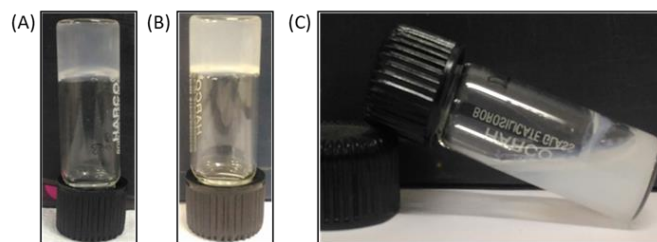


**Figure 2.7.** Digital image of the hydrogel and turbid sol formed upon addition of  $Zn^{2+}$  ions to (a) *L*-Histidine, (b) *D*-Histidine and (c) a 1:1 racemic mixture of histidine (*DL*-histidine).

increasing ee% of the ligand (for either of *L* or *D* enantiomers), the ability of the Zn-His system towards gelation was enhanced (Figure 2.8 and Table 2.2). The system lost its gelation ability, whenever ee% was less than 40%. These results probably arise from the stereoselectivity of inter-ligand interactions as the intermolecular H-bonding or hydrophobic interactions involved in the formation of the supramolecular assemblies might be weakened upon lowering the ee%.



**Figure 2.8.** Digital images of the precipitates and hydrogels formed by histidine and  $Zn^{2+}$  ions with varying ee % of *D*-histidine. Partial gel formed upon addition of  $Zn^{2+}$  ions to a 30% ee solution of *D*-histidine.

**Table 2.2** Control of gelation by varying the enantiomeric excess of *L*- or *D*- forms of histidine. Final concentration was 100 mM of Zn(II) and 100 mM of Histidine.

<i>L</i> - Histidine (0.2M)	<i>D</i> -Histidine (0.2M)	$Zn(NO_3)_2 \cdot 6H_2O$ (0.2M)	ee (%)	Result
0.5 ml	0 mL	0.5 mL	100 (L)	Gel
0.437 mL	0.063 mL	0.5 mL	75 (L)	Gel
0.375 mL	0.125 mL	0.5 mL	50 (L)	Weak gel
0.312 mL	0.188 mL	0.5 mL	25 (L)	Turbid Sol
0.275 mL	0.225 mL	0.5 mL	10 (L)	Turbid Sol
0 ml	0.5 mL	0.5 mL	100 (D)	Gel
0.063 mL	0.437 mL	0.5 mL	75 (D)	Gel
0.125 mL	0.375 mL	0.5 mL	50 (D)	Weak gel
0.188 mL	0.312 mL	0.5 mL	25 (D)	Turbid Sol
0.225 mL	0.275 mL	0.5 mL	10 (D)	Turbid Sol



### 2.2.3. Structural characterizations of the hydrogel:

Fourier-transform infrared spectroscopy (FTIR) spectrum of pure histidine<sup>[49]</sup> showed peaks at 1631  $\text{cm}^{-1}$  and 1415  $\text{cm}^{-1}$  due to antisymmetric and symmetric C-O stretching of the  $\text{COO}^-$  group respectively, which got shifted to 1602  $\text{cm}^{-1}$  and 1382  $\text{cm}^{-1}$  in Zn-*L*-His complex (Figure 2.9), indicating the involvement of the carboxylate group in H-bonding.

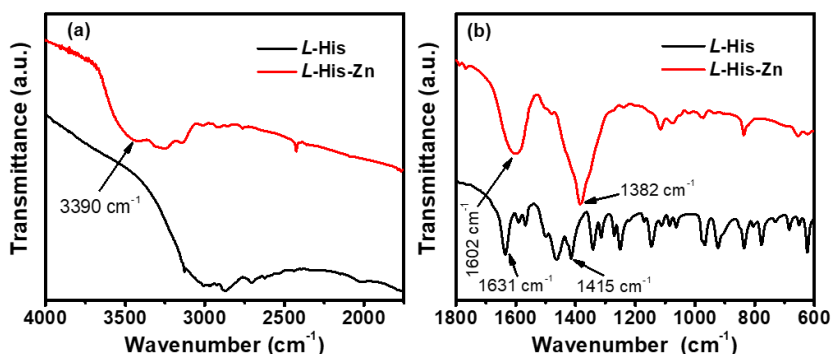


**Figure 2.9.** FTIR spectrum of *L*-histidine and Zn-*L*-histidine xerogel in (a) 4000-1800  $\text{cm}^{-1}$  region and (b) 1800-400  $\text{cm}^{-1}$  region respectively.

Selected area electron diffraction (SAED) performed on the dried gel fibers suggested that the fibers were crystalline in nature (Figure 2.10a). Energy-dispersive X-ray (EDX) analysis revealed the involvement of different elements, Zn, C, N and O along with their percentage in the hydrogel matrix thereby suggesting the coordination of histidine to  $\text{Zn}^{2+}$  ions. Elemental analysis of the freeze dried Zn-His gel suggested 25.06% carbon,

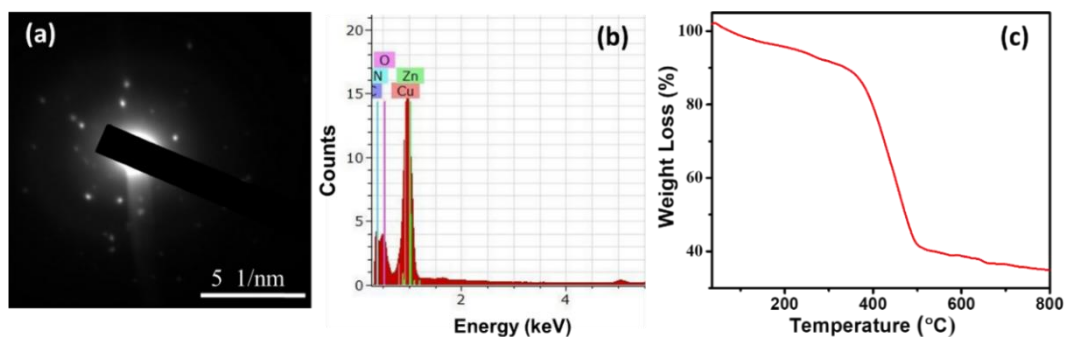


**Figure 2.10.** (a) Selected area electron diffraction (SAED) pattern of the Zn-*L*-histidine gel fibers. (b) EDX spectrum of the Zn-histidine hydrogel, showing the presence of C, N, O and Zn. (Cu indicated in the spectrum is due to the copper TEM grid. (c) TGA analysis of the freeze dried Zn-*L*-Histidine metallohydrogel.

14.56% nitrogen and 3.94% hydrogen in the coordination complex (Figure 2.10b and Table 2.3). These elemental analysis results together with the EDX analysis indicated a 1:1 complex between histidine and  $Zn^{2+}$  ions, which corroborated the requirement of 1:1 metal:ligand ratio for stable gel formation.

Thermogravimetric analysis of the freeze dried xerogel showed two distinct weight losses of 12.7% and 47.1% in the temperature range of 25-350 °C and 355-500 °C respectively, presumably due to the loss of water molecules and  $CO_2$ ,  $N_2$  and other organic moieties respectively (Figure 2.10c). All these results together enabled us to suggest tentatively the formation of  $[Zn(His)(H_2O)_3(OH)]$  complex to result chains of metallo-supramolecular polymer.

**Table 2.3.** Experimental and theoretical elemental composition of the  $[Zn(His)(H_2O)_3(OH)]$  complex formed upon the interaction of  $Zn^{2+}$  ions to aqueous alkaline histidine solution.

	<b>C (%)</b>	<b>N (%)</b>	<b>H (%)</b>
Experimental	25.06	14.56	3.94
Theoretical	24.80	14.47	5.11

#### **2.2.4. Microscopic Characterizations:**

These initially formed chains of the metal coordinated complex under the influence of multiple H-bonding interactions can undergo consecutive self-assembly to form nanofibrils,<sup>[49]</sup> which entangle into dense three-dimensional fibrillar network as confirmed by field emission scanning electron microscopic (FESEM) studies. Such a dense nanofibrous network of Zn-L-His gel can eventually trap large volume of water resulting in the formation of hydrogel (Figure 2.11a). The transmission electron microscopic (TEM) studies performed on the hydrogel from Zn-His complex further confirmed the nanofibrillar morphology of the gel (Figure 2.11b-c). The nanofibers are intertwined around themselves to form helical fibers which were hundreds of nanometer in length, the average diameter of the fibers as calculated from the TEM image varied between 15-50 nm. On the other hand, TEM studies performed

on the Zn-*DL*-His turbid sol revealed the formation of chains of small, irregular shaped nanoparticles (Figure 2.11d), due to the orderless stacking in the racemic mixture. These nanoparticles, understandably, could not trap water molecules, resulting in the formation of a precipitate rather than a gel.

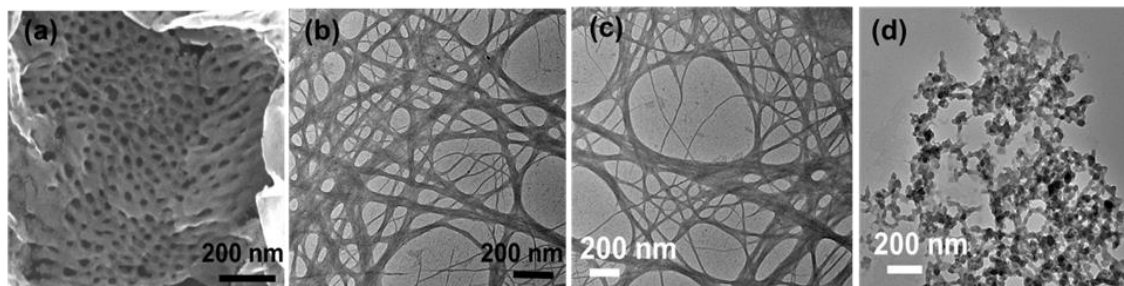


**Figure 2.11.** (a) FESEM image of Zn-*L*-His metallogel and TEM image of (b) Zn-*L*-His metallogel, (c) Zn-*D*-His metallogel from 1:1 Zn and histidine showing nanofibrous morphology. (d) Turbid sol from 1:1 racemic mixture of *DL*-histidine with Zn(II).

### 2.2.5. Supramolecular Chirality:

Development of functional supramolecular materials mediated by chirality are essential for molecular recognition and chiral sensing applications.<sup>[50,51]</sup> Circular dichroism (CD) studies demonstrated the binding of Zn<sup>2+</sup> to histidine led to an inversion of chirality in the complex with respect to the used amino acid. Whereas *L*-histidine showed a positive cotton band at 216 nm, the diluted Zn-*L*-His hydrogel showed a negative band at 217 nm (Figure 2.12a), suggesting a modulation in the supramolecular chirality for the complex. Similar sign inversion was observed for the hydrogel formed from *D*-histidine. Although, change in CD signal of metal complexes and supramolecular assemblies in response to external stimuli such as anions, solvent or pH are known,<sup>[52,53]</sup> the present work is the first report showing the metal mediated modulation in chirality of supramolecular assemblies generated using native amino acid molecules. The addition of EDTA solution to the gel state led to dissolution of the gel due to strong metal-EDTA complexation, resulting histidine being free. The CD spectrum of this solution reverts back to the one akin to that of native histidine, confirming that the supramolecular chirality of the helical fibers complex is opposite to that of the amino acids (Figure 2.12b). The signal, however, was blue shifted by

5 nm, which might be due to Zn-EDTA complex in the solution. Job's plot using the molar ellipticity for the Zn-*L*-His complex with variation of [*L*-Histidine] at 217 nm, (Figure 2.12c & d), indicated a 1:1 metal:ligand stoichiometry, consistent with the elemental analysis results. Supramolecular chirality of the complex can be tuned based on the ee% of either enantiomer in a 1:1 mixture of Zn and *L*-histidine and *D*-histidine as depicted by the change in magnitude of molar ellipticity with increasing ee% (Figure 2.13a & b). The magnitude of supramolecular chirality showed linear behavior at higher ee% and deviate from linearity at lower ee%.

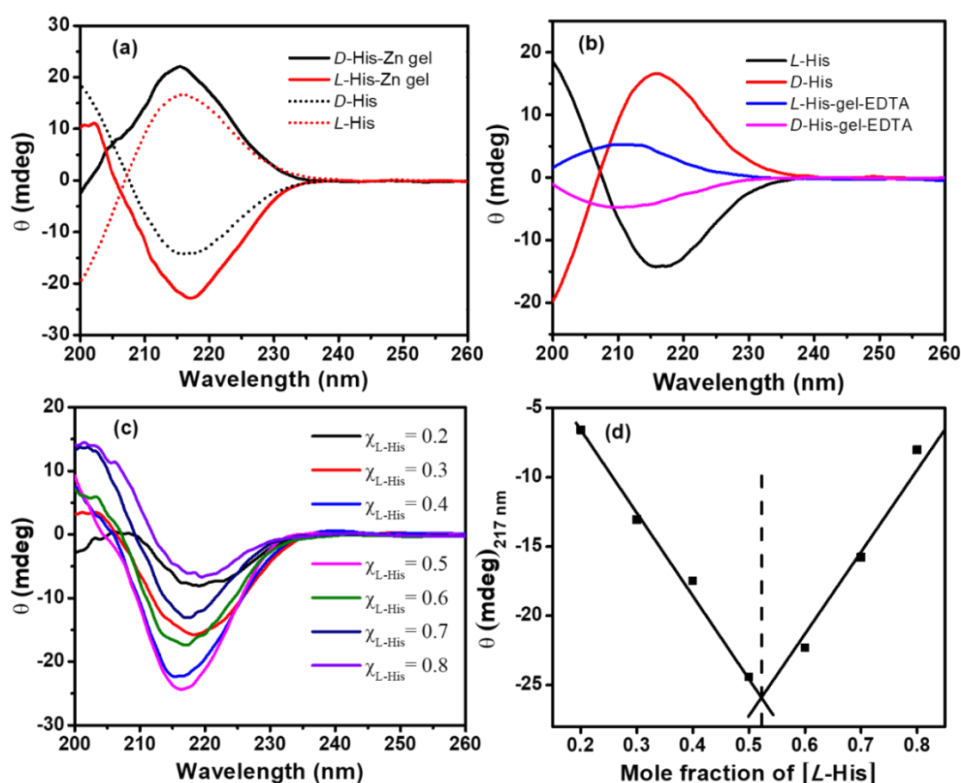


**Figure 2.12.** CD spectra of the (a) diluted Zn-*L*-His metallogel and Zn-*D*-His metallogel in water showing opposite sign with respect to pure *L*-histidine and *D*-histidine (concentration of 2.5 mM and pH = 12 were maintained for pure histidine and histidine in Zn-his complex), (b) sol obtained after addition of EDTA to *L*-histidine-Zn gel and *D*-histidine-Zn gel, showing signals similar to pure *L*- and *D*-histidine respectively with slight blue shift, (c) CD spectra of the supramolecular assembly with varying mole fraction of *L*-histidine to form Zn-*L*-Histidine, (d) Job's plot of CD signal at 217 nm versus mole fraction of *L*-histidine, showing 1:1 metal: ligand stoichiometry.

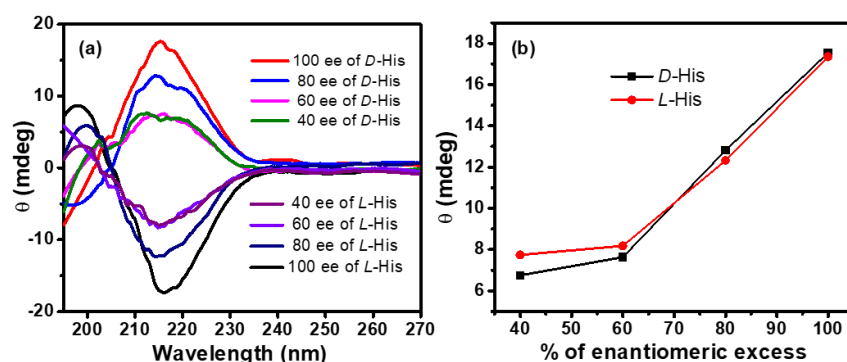


**Figure 2.13** (a) CD spectra of the supramolecular assembly with varying % of ee of either *D*-histidine or *L*-histidine, (b) plot of molar ellipticity with ee of either *D*-histidine or *L*-histidine (1.25 mM of Zn(II): His).

### 2.2.6. Rheological Investigation:

The dynamic amplitude sweep rheological experiment performed on the Zn-His gel showed the dominance of storage modulus,  $G'$  over the loss modulus,  $G''$  till a critical strain

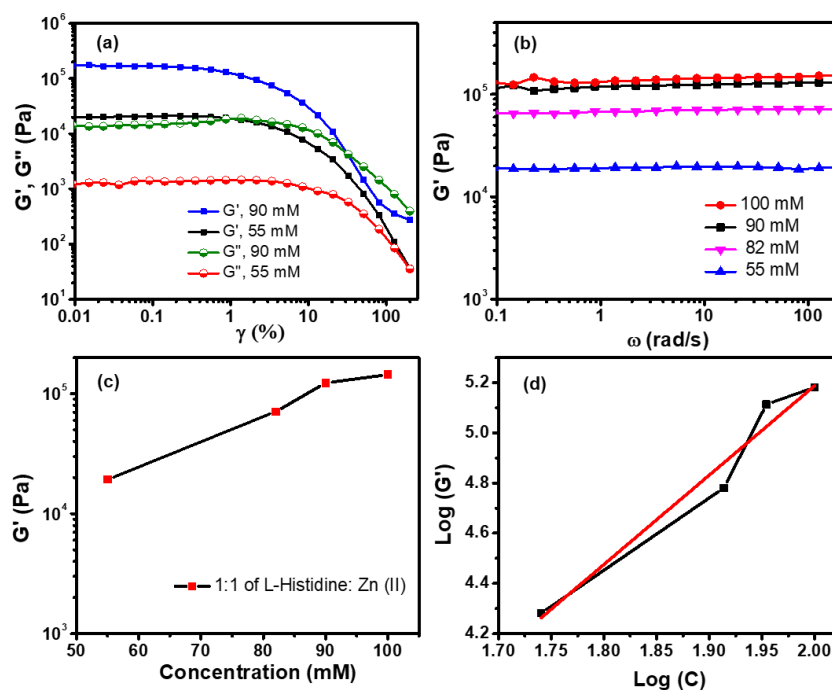


**Figure 2.14.** (a) Dynamic strain amplitude rheological experiment for Zn-*L*-histidine in 90 mM and 55 mM. (b) Dynamic frequency sweep rheology of the Zn-*L*-histidine metallogel at a constant strain of 0.1% for Zn-*L*-histidine in 100, 90, 82 and 55 mM. (c) Plot of  $G'$  with concentration of Zn-*L*-Histidine in 1:1 ratio for 100, 90, 82, 55 mM. (d) Logarithmic plot of  $\text{Log}(G')$  and  $\text{Log}(C)$  with linear fit having slope of 3.5.

( $\gamma$ ) percentage beyond which the gel network starts to yield and flow (Figure 2.14a).

Dynamic frequency sweep experiments performed at a constant strain of 0.1% further showed that  $G'$  was higher than  $G''$  by a factor of  $\sim 10$  in the complete range of angular frequency with frequency independent behavior, suggesting viscoelastic solid-like nature of the metalgel. Also,  $G'$  values for the hydrogels from different concentration of histidine gradually increases and scaled as the power of the gelator concentration ( $G' \propto c^m$ ) with an exponent of 3.5 (Figure 2.14b-d), which is in agreement with the other amino acid based gels.<sup>[54]</sup>

The hydrogels exhibit increased elastic moduli with increasing ee% of the *L*-histidine with respect to *D*-histidine in the Zn-Histidine complex in a frequency sweep experiment (Figure 2.15a & b). Time sweep rheological experiment can exhibit the gel formation from the sol phase and subsequent increase in elastic modulus. Alkaline solution of Zn(II) and 100% ee or 75% ee of *L*-histidine with respect to *D*-Histidine was mixed on rheometer plate

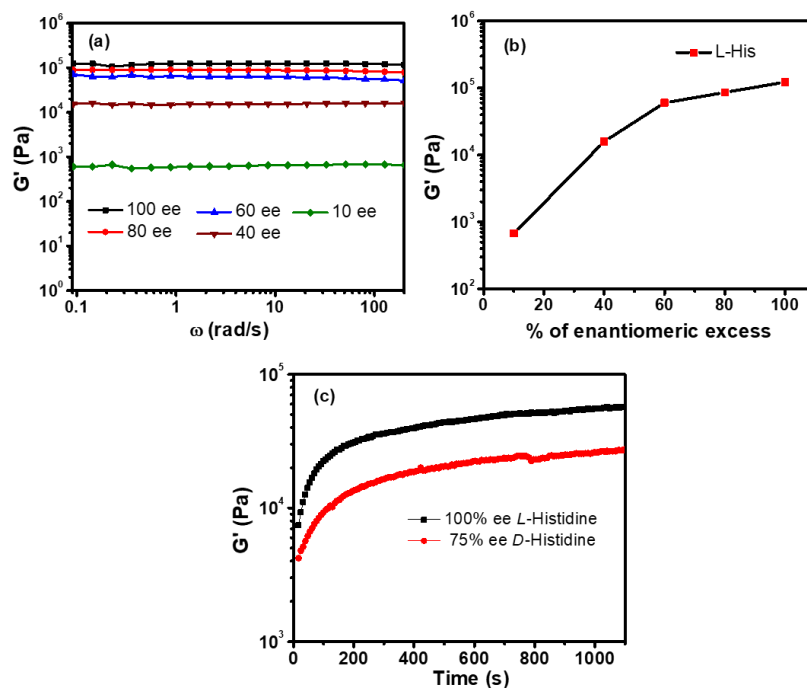


**Figure 2.15.** (a) Dynamic frequency sweep rheology for hydrogels prepared from different ee% of *L*-Histidine with respect to *D*-Histidine in a complex of Zn-His. (b) Plot of  $G'$  with enantiomeric excess of 1:1 ratio of Zn-*L*-Histidine (100 mM of Zn and mixture of *L*-Histidine and *D*-Histidine). (c) Time sweep experiments of gel formation for the hydrogels made with 100 and 75 ee% of *L*-histidine.

and the growth of  $G'$  was monitored at 0.1% constant strain and 10 rad/s frequency.  $G'$  was found to increase instantaneously and reach the saturation plateau with different final value, although the hydrogel formation from 100% ee was found to be faster than that from 75% ee of *L*-histidine (Figure 2.15c).

The self-healing property of several metallogels has been explored recently. Due to their ability to disrupt and reform the weak non-covalent interactions, metallogels are expected to possess self-healing property.<sup>[55–59]</sup> We found that the Zn-His metallogel was not only multi-stimuli responsive in nature, but it also exhibited rapid self-healing property in air at room temperature. When two blocks of the gels were brought in close contact with each other and slightly pressed, they self-healed at the place of cut within two hours to give a single block, without the use of any external healing agent. For clear visibility, one of the blocks was doped using methylene blue. Using alternate dye doped and un-doped blocks

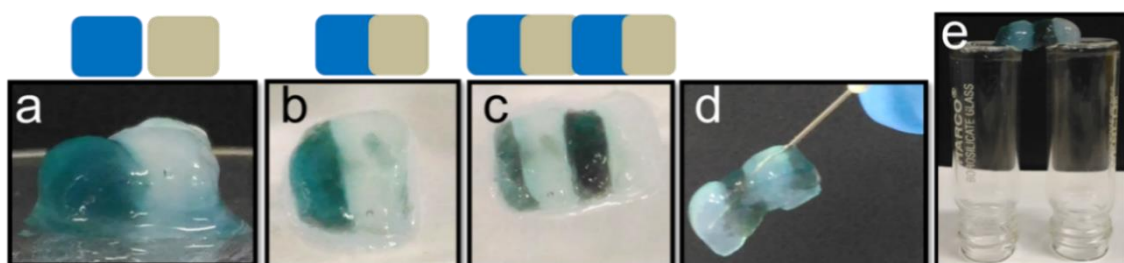


**Figure 2.16** (A) Digital images showing the self-healing property of the Zn-histidine metallogel. (a) Two blocks of the gel brought in contact with each other, (b) The two blocks self-heal to give a single block, (c) four blocks could be self-healed to give a single block, (d) the self-healed single block prepared from four blocks held vertically, (e) Self-healed single block of Zn-histidine prepared from four single gel blocks.

The self-healing property was also quantitatively studied using dynamic oscillatory rheology which involves straining of the gel until failure and then monitoring its recovery which confirmed that the gels were self-healing in nature (Figure 2.17a). A slight decrease in the value of the storage modulus after recovery was observed which was due to the loss of some amount of water from the gel. The mechanical properties of the self-healed gel were compared with that of the fresh gel and were found to be comparable to that of the fresh gel (Figure 2.17b), suggesting that the gel retains its properties even after the healing process

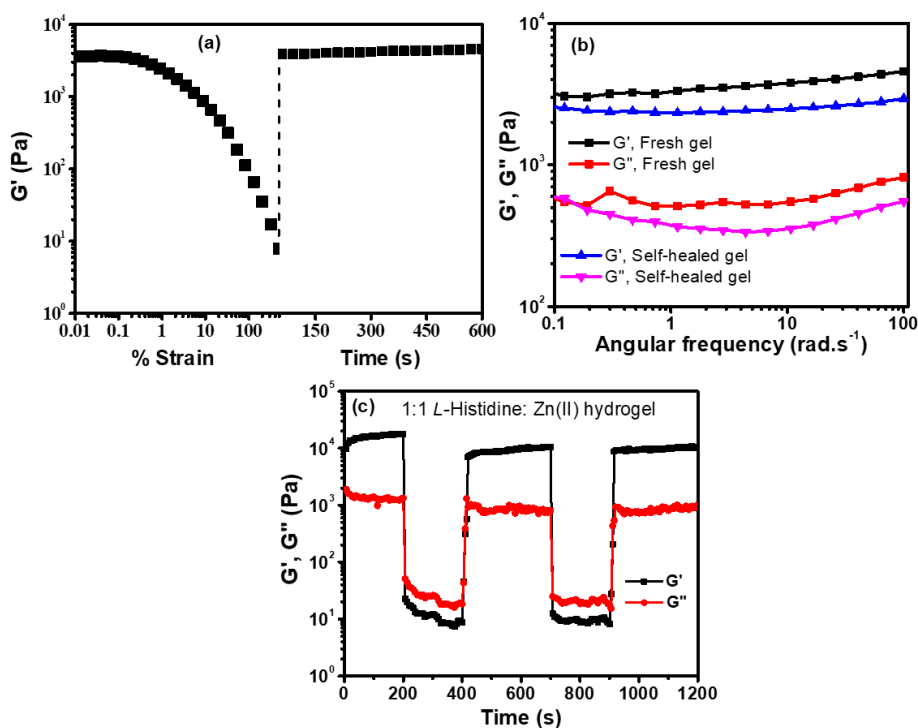


**Figure 2.17** (a) Dynamic oscillatory rheology to quantify the speed of recovery by shearing the Zn-His hydrogel at increasing strain at a frequency of 1 Hz from 0.01 until 500% strain, after which the gel recovery was monitored at 1% strain and 1 Hz. (b) Frequency sweep rheological investigation of fresh Zn-L-His gel and self-healed Zn-L-His gel. (c) Thixotropic behaviour by oscillatory rheology for three cycles with strain variation from 0.1% to 100% in periodic manner. Concentration of Histidine: Zn = 100 mM.

four blocks could be combined to give a single block. This block could be held either vertically or horizontally (Figure 2.16a-e). Thixotropic nature of the metallo-hydrogels (100 mM) were investigated by applying alternating 0.1% and 100% strain for three cycles, which exhibits instantaneous self-recovery of the network after removal of high strain (Figure 2.17c).

## 2.3. Conclusions

Thus, the study demonstrated facile preparation of a supramolecular metallo-hydrogel by mixing aqueous solutions of inexpensive and unsubstituted amino acid, histidine and  $\text{Zn}^{2+}$  ions. The gel formation was specific to both the metal ion as well as amino acid



and displayed multi-stimuli responsiveness towards gel-to-sol transition. The supramolecular chirality of the coordination polymer was modulated with respect to the chirality of the amino acid and can be tuned with the ee%. Further, the gelation properties and viscoelastic behavior of the resulting hydrogels could be conveniently modulated by varying the enantiomeric excess of the ligand. The gel showed self-recovery of the broken network due to dynamic nature of the coordination bond between metal and histidine. Such intrinsic self-healing does not require additional stimuli or healing agents. The use of native amino acids as ligands for the convenient formation of supramolecular metallogels will add to the repertoire of complex molecular architectural design using basic biological building blocks with potential application in drug delivery, sensing, encapsulation of biomolecules. The tuneable Zn-histidine metallogel with its optical purity is therefore expected to open up new areas for the development of chiral sensing and recognition platforms.

## **2.4. Experimental Section**

### **2.4.1. Materials:**

*L*-Histidine, *L*-Arginine, *L*-Lysine, *D*-Histidine and Manganese chloride were purchased from Sisco Research Laboratories (SRL), India. Zinc nitrate hexahydrate, Zinc acetate dihydrate, Zinc chloride, Calcium chloride dihydrate, Magnesium sulfate, Iron(III) nitrate nonahydrate, Cobalt chloride hexahydrate, Nickel chloride hexahydrate, Copper sulfate hexahydrate, Cadmium nitrate tetrahydrate, Sodium hydroxide, ammonia solution, Ethylenediaminetetraacetic acid (EDTA), Trifluoroacetic acid, Sodium sulfide, Nitric acid, Acetonitrile and Methanol were purchased from Merck, India. Silver nitrate, Gold(III) chloride trihydrate and Glutamic acid monosodium hydrate were purchased from Sigma Aldrich. All the chemicals were of analytical grade and were used without any further purification. Milli-Q water was used throughout the experiments.

### **2.4.2. Instrumentation:**

FTIR spectra were recorded in KBr pellet using a Cary 600 series spectrometer from Agilent

technologies. Elemental analysis was carried out on a Thermo Scientific Flash 2000 analyzer. Thermogravimetric analysis was performed using a Mettler Toledo thermal analysis system at a heating rate of 5 °C per minute under nitrogen atmosphere. Field emission scanning electron microscopy images were recorded on a JEOL 7600F microscope after gold coating. Transmission electron microscopy images were recorded on a JEOL JEM-2100 instrument at an accelerating voltage of 200 kV. Circular dichroism spectra were recorded using a JASCO J-1500 spectrometer. Rheological measurements were performed using an Anton Paar Physica MCR 302 rheometer.

### **2.4.3. Methods**

**2.4.3.1. Preparation of Zn-histidine metallogels:** A solution of *L*- or *D*-histidine (100 mM) was prepared in water by the dropwise addition of 1M NaOH solution, until the pH of the solution reached to ~12. Similarly, a solution of Zn(NO<sub>3</sub>)<sub>2</sub>·6H<sub>2</sub>O, Zn(CH<sub>3</sub>COO)<sub>2</sub>·2H<sub>2</sub>O or ZnCl<sub>2</sub> (100 mM) were prepared in water. 1.0 mL of the zinc salt was added to the above prepared histidine solution, which led to the spontaneous formation of self-standing metallo-hydrogel.

**2.4.3.2. Interaction of *L*-histidine with Zn<sup>2+</sup> ions in mixed solvent systems:** For the interaction of Zn<sup>2+</sup> ions with histidine in mixed solvent systems, *L*-histidine solution (100 mM) was prepared in water and a solution of Zn(NO<sub>3</sub>)<sub>2</sub> (100 mM) was prepared in methanol or acetonitrile. The interaction was studied by adding the Zn<sup>2+</sup> solution (0.8 mL) (in MeOH or CH<sub>3</sub>CN) to an aqueous solution (0.8 mL) of *L*-histidine, which resulted in the formation of a white precipitate.

**2.4.3.3. Stimuli responsive studies of the Zn-histidine metallogels:** Stimuli responsive nature of the Zn-histidine metallogel was studied by subjecting the gel to different stimuli. All the stimuli responsive studies were performed using 1.4 mL of the Zn-*L*-histidine gel. The thermo-responsive nature of the gel was studied by heating the vial containing the gel at a temperature of 135 °C for 20 minutes, when the gel transformed into a sol. The

reversible pH responsive nature of the gel was studied by adding 100  $\mu\text{L}$  of 1M  $\text{HNO}_3$  to the gel, which led to the formation of a clear solution within 5 minutes. To this clear solution, an equivalent amount of 1M NaOH solution was added, which led to the recovery of the gel. The chemo-responsive nature of the gel was studied by addition of EDTA,  $\text{Na}_2\text{S}$  and TFA to the gel taken in a vial prepared by the addition of 0.7 mL of  $\text{Zn}(\text{NO}_3)_2$  to 0.7 mL of *L*-histidine. The addition of EDTA (20.45 mg) to the gel state, spread over the gel in the vial, which led to the formation of clear solution within 2 minutes. Similarly, 5.45 mg of  $\text{Na}_2\text{S}$  was added to the gel, which led to the collapse of the gel. The addition of 100  $\mu\text{L}$  of 1M TFA to the gel immediately led to a clear solution. The addition of an equivalent amount of ammonia solution to this clear solution led to the reformation of the gel state.

**2.4.3.4. Transmission electron microscopic studies:** Samples for electron microscopic studies were prepared by taking a small amount of the gel in an eppendorf tube. The gel (15 mM) was diluted using water. Then the sample was drop-casted on a carbon coated copper grid for TEM analysis a followed by room temperature drying. EDAX spectrum was recorded using a Bruker X Flash 6130 EDAX instrument attached to the TEM.

**2.4.3.5. Circular Dichroism studies:** Circular dichroism spectra were recorded using a quartz cell of 1 mm path length and data pitch 0.1 nm with a scanning speed of 50 nm/min. The concentrations of the amino acids were 2.5 mM. For the CD studies of the gels, a weak gel with a concentration of 25 mM (both the reactants) was first prepared and then diluted ten times in water to get a concentration of 2.5 mM. Each spectrum is the average of two consecutive scans. Job's plot was obtained by following the CD signal of the Zn-*L*-histidine complex at 217 nm. *L*-histidine and  $\text{Zn}(\text{NO}_3)_2$  with a concentration of 2.5 mM were prepared and mixed with varying mole fractions of both the reactants such that the final volume of the solution was 1.0 mL.

**2.4.3.6. Rheological studies:** Rheological investigations were performed on the Zn-histidine metallogel by using parallel plate geometry of diameter 50 mm (PP-50). The hydrogel was

placed on the plate of the rheometer using a spatula. The temperature was maintained at 25 °C using a peltier temperature controller attached with Julabo chillar. The dynamic strain sweep experiments were performed using a constant frequency of 10 rad/s. The frequency sweep experiments were performed using a constant strain of 0.1% in the frequency range from 0.05-200 rad.s<sup>-1</sup>. For time sweep experiment, Zn and histidine were mixed onto rheometer plate and G', G'' were monitored with time using a constant strain of 0.1% and angular frequency 10 rad.s<sup>-1</sup>. Thixotropic oscillatory rheology for self-healing behavior was performed by applying alternating cycles of 0.1% and 100% strain with an angular frequency of 10 rad/s.

## 2.5. References

- [1] D. J. Cornwell, D. K. Smith, *Mater. Horizons* **2015**, *2*, 279.
- [2] B. O. Okesola, D. K. Smith, *Chem. Soc. Rev.* **2016**, *45*, 4226.
- [3] S. Mura, J. Nicolas, P. Couvreur, *Nat. Mater.* **2013**, *12*, 991.
- [4] D. Habault, H. Zhang, Y. Zhao, *Chem. Soc. Rev.* **2013**, *42*, 7244.
- [5] C. Ren, J. Zhang, M. Chen, Z. Yang, *Chem. Soc. Rev.* **2014**, *43*, 7257.
- [6] M. A. Rahim, M. Björnmalm, T. Suma, M. Faria, Y. Ju, K. Kempe, M. Müllner, H. Ejima, A. D. Stickland, F. Caruso, *Angew. Chemie - Int. Ed.* **2016**, *55*, 13803.
- [7] Z. Sun, F. Lv, L. Cao, L. Liu, Y. Zhang, Z. Lu, *Angew. Chemie Int. Ed.* **2015**, *54*, 7944.
- [8] A. Y. Y. Tam, V. W. W. Yam, *Chem. Soc. Rev.* **2013**, *42*, 1540.
- [9] P. Sutar, T. K. Maji, *Chem. Commun.* **2016**, *52*, 8055.
- [10] P. Dastidar, S. Ganguly, K. Sarkar, *Chem. An Asian J.* **2016**, *11*, 2484.
- [11] X. L. Hu, F. H. Liu, C. Qin, K. Z. Shao, Z. M. Su, *Dalt. Trans.* **2015**, *44*, 7822.
- [12] Z. Džolić, M. Cametti, D. Milić, M. Žinić, *Chem. A Eur. J.* **2013**, *19*, 5411.
- [13] S. Samai, K. Biradha, *Chem. Mater.* **2012**, *24*, 1165.
- [14] S.-C. Wei, M. Pan, K. Li, S. Wang, J. Zhang, C.Y. Su, *Adv. Mater.* **2014**, *26*, 2072.
- [15] P. S. Yavvari, S. Pal, S. Kumar, A. Kar, A. K. Awasthi, A. Naaz, A. Srivastava, A. Bajaj, *ACS Biomater. Sci. Eng.* **2017**, *3*, 3404.
- [16] S. Saha, J. Bachl, T. Kundu, D. D. Díaz, R. Banerjee, *Chemical* **2014**, *50*, 3004.
- [17] R. Roy, M. Bhagyalalitha, P. Choudhury, P. Dastidar, *Chem. Commun.* **2016**, *52*, 13811.
- [18] H. Liang, Z. Zhang, Q. Yuan, J. Liu, *Chem. Commun.* **2015**, *51*, 15196.
- [19] I. Imaz, M. Rubio-Martínez, J. An, I. Solé-Font, N. L. Rosi, D. Maspoch, *Chem. Commun.* **2011**, *47*, 7287.
- [20] H. Wu, C. Tian, Y. Zhang, C. Yang, S. Zhang, Z. Jiang, *Chem. Commun.* **2015**, *51*, 6329.
- [21] I. Imaz, M. Rubio-Martínez, W. J. Saletta, D. B. Amabilino, D. Maspoch, *J. Am.*

- Chem. Soc.* **2009**, *131*, 18222.
- [22] B. Sharma, A. Mahata, S. Mandani, T. K. Sarma, B. Pathak, *RSC Adv.* **2016**, *6*, 62968.
- [23] R. N. Das, Y. P. Kumar, S. Pagoti, A. J. Patil, J. Dash, *Chem. A Eur. J.* **2012**, *18*, 6008.
- [24] J. Dash, A. J. Patil, R. N. Das, F. L. Dowdall, S. Mann, *Soft Matter* **2011**, *7*, 8120.
- [25] P. Duan, H. Cao, L. Zhang, M. Liu, *Soft Matter* **2014**, *10*, 5428.
- [26] M. Liu, L. Zhang, T. Wang, *Chem. Rev.* **2015**, *115*, 7304.
- [27] S. Maity, P. Das, M. Reches, *Sci. Rep.* **2015**, *5*, 1.
- [28] Z. Kokan, B. Perić, M. Vazdar, Ž. Marinić, D. Vikić-Topić, E. Meštrović, S. I. Kirin, *Chem. Commun.* **2017**, *53*, 1945.
- [29] D. K. Smith, *Chem. Soc. Rev.* **2009**, *38*, 684.
- [30] A. J. Wilson, J. Van Gestel, R. P. Sijbesma, E. W. Meijer, *Chem. Commun.* **2006**, 4404.
- [31] A. R. A. Palmans, J. A. J. M. Vekemans, E. E. Havinga, E. W. Meijer, *Angew. Chemie (International Ed. English)* **1997**, *36*, 2648.
- [32] B. M. W. Langeveld-Voss, R. J. M. Waterval, R. A. J. Janssen, E. W. Meijer, *Macromolecules* **1999**, *32*, 227.
- [33] J. M. Suk, V. R. Naidu, X. Liu, M. S. Lah, K. S. Jeong, *J. Am. Chem. Soc.* **2011**, *133*, 13938.
- [34] M. Hutin, J. Nitschke, *Chem. Commun.* **2006**, *0*, 1724.
- [35] R. Katoono, S. Kawai, K. Fujiwara, T. Suzuki, *Chem. Sci.* **2015**, *6*, 6592.
- [36] M. Peterca, M. R. Imam, C. H. Ahn, V. S. K. Balagurusamy, D. A. Wilson, B. M. Rosen, V. Percec, *J. Am. Chem. Soc.* **2011**, *133*, 2311.
- [37] J. S. Shen, G. J. Mao, Y. H. Zhou, Y. B. Jiang, H. W. Zhang, *Dalt. Trans.* **2010**, *39*, 7054.
- [38] A. Longo, D. Banerjee, D. Hermida-Merino, G. Portale, P. Calandra, V. Turco Liveri, *J. Phys. Chem. C* **2015**, *119*, 18798.
- [39] J. Dubarle-Offner, J. Moussa, H. Amouri, B. Jouvelet, L. Bouteiller, M. Raynal, *Chem. - A Eur. J.* **2016**, *22*, 3985.
- [40] J. Shen, G. Mao, Y. Zhou, Y. Jiang, H. Zhang, *Dalt. Trans.* **2010**, *39*, 7054.
- [41] D. E. Fullenkamp, L. He, D. G. Barrett, W. R. Burghardt, P. B. Messersmith, *Macromolecules* **2013**, *46*, 1167.
- [42] J. Chen, T. Wang, M. Liu, *Inorg. Chem. Front.* **2016**, *3*, 1559.
- [43] A. Srivastava, N. Holten-Andersen, G. D. Stucky, J. H. Waite, *Biomacromolecules* **2008**, *9*, 2873.
- [44] Y. Liu, C. Chen, T. Wang, M. Liu, *Langmuir* **2016**, *32*, 322.
- [45] C. Chen, T. Wang, Y. Fu, M. Liu, *Chem. Commun.* **2016**, *52*, 1381.
- [46] J. M. J. Paulusse, D. J. M. Van Beek, P. P. Sijbesma, *J. Am. Chem. Soc.* **2007**, *129*, 2392.
- [47] S. Zhang, S. Yang, J. Lan, Y. Tang, Y. Xue, J. You, *J. Am. Chem. Soc.* **2009**, *131*, 1689.
- [48] P. Bairi, B. Roy, A. K. Nandi, *J. Mater. Chem.* **2011**, *21*, 11747.
- [49] L. Zhou, S. Li, Y. Su, X. Yi, A. Zheng, F. Deng, *J. Phys. Chem. B* **2013**, *117*, 8954.
- [50] M. M. Bouman, E. W. Meijer, *Adv. Mater.* **1995**, *7*, 385.

- [51] B. M. W. Langeveld-Voss, M. P. T. Christiaans, R. A. J. Janssen, E. W. Meijer, *Macromolecules* **1998**, *31*, 6702.
- [52] S. Tashiro, R. Kubota, M. Shionoya, *J. Am. Chem. Soc.* **2012**, *134*, 2461.
- [53] H. Miyake, K. Yoshida, H. Sugimoto, H. Tsukube, *J. Am. Chem. Soc.* **2004**, *126*, 6524.
- [54] S. Bhattacharya, A. Pal, *J. Phys. Chem. B* **2008**, *112*, 4918.
- [55] M. Häring, D. D. Díaz, *Chem. Commun.* **2016**, *52*, 13068.
- [56] N. Holten-Andersen, M. J. Harrington, H. Birkedal, B. P. Lee, P. B. Messersmith, K. Y. C. Lee, J. H. Waite, *Proc. Natl. Acad. Sci. U. S. A.* **2011**, *108*, 2651.
- [57] M. Krosgaard, M. A. Behrens, J. S. Pedersen, H. Birkedal, *Biomacromolecules* **2013**, *14*, 297.
- [58] S. Basak, J. Nanda, A. Banerjee, *Chem. Commun.* **2014**, *50*, 2356.
- [59] X. Yan, D. Xu, X. Chi, J. Chen, S. Dong, X. Ding, Y. Yu, F. Huang, *Adv. Mater.* **2012**, *24*, 362.

## Chapter 3

# Pathway driven self-assembly and living supramolecular polymerization in an amyloid-inspired peptide amphiphile

*In this chapter, a minimalistic peptide amphiphile is designed inspired by the  $\beta$ -amyloid nucleating core of A $\beta$ 42. The peptide demonstrates step-wise self-assembly in water. Variation of temperature or solvent composition arrests the self-assembly in metastable state to yield nanoparticles, which on gradual increase in temperature produce kinetically controlled nanofibers and eventually, thermodynamically stable twisted helical bundles. Mechanical agitation of the fibers furnishes short seeds with narrow polydispersity index, which by mediation of seeded supramolecular polymerization establishes a perfect control over the length of the nanofibers. Such pathway dependent nanostructures with precise control over length regime is exploited to tune the mechanical properties of the peptide hydrogels.*

### 3.1. Introduction

Nature is a perfect engineer to design materials having complex structure and function through the mediation of non-covalent interaction. Over recent decades, scientists have ramped up the efforts to mimic nature by designing supramolecular materials with such structure-functional control using bottom-up self-assembly.<sup>[1-3]</sup> However, unlike natural systems guided by out-of equilibrium self-assembly, most of the supramolecular polymeric processes undertaken in the laboratory are dictated by thermodynamically controlled single state and concentration-dependent self-assembly pathways.<sup>[4]</sup> Manner *et al.*, were the first to report living epitaxial crystallization mediated self-assembly in block co-polymeric micelles.<sup>[5,6]</sup> However, the recent understanding of pathway complexity, with the coexistence of multiple competitive pathways in a self-assembly process, provided a paradigm shift in the strategy and tool to control the fate of supramolecular systems under a

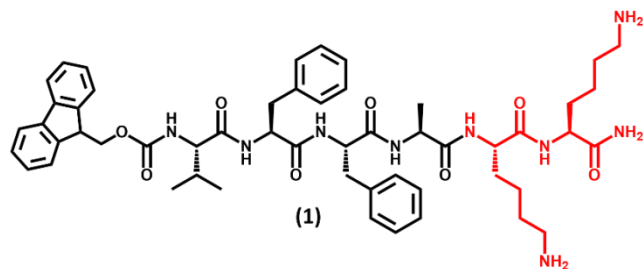
variety of conditions.<sup>[7–10]</sup> Arresting the monomer in the metastable state allows access to kinetically trapped species,<sup>[11–15]</sup> which can be employed in seeded supramolecular polymerization to control the self-assembly with structural and dimensional precision, akin to the controlled living polymerization in covalent polymers.<sup>[16]</sup> Recently, the groups of Sugiyasu, Takeuchi and Würthner demonstrated elegant examples of pathway complexity in functionalized porphyrin and perylene bisimide to form kinetically or thermodynamically controlled aggregates by tweaking the conditions, *e.g.* temperature and solvents.<sup>[17–19]</sup> In another interesting example, Aida *et al.*, demonstrated the competition between intra- vs. inter-molecular hydrogen bonding to control the opening of metastable cage to furnish 1-D self-assembly in corannulene molecules with multiple amide functionalities.<sup>[20,21]</sup> Interplay of dynamic covalent chemistry and self-replication was used by Otto *et al.*, to grow kinetically controlled fibers in aqueous milieu from metastable macrocycles with excellent length control.<sup>[22]</sup> The nucleation-elongation model in amyloid fibril formation, as observed in prion infection,<sup>[23,24]</sup> provides a vital cue to study the pathway complexity to get insight into the fibrillation.<sup>[25,26]</sup> We postulate that self-assembly of short peptide fragments inspired from an amyloid nucleating core may act as a model system to study kinetically controlled living supramolecular polymerization and formation of hierarchical structures in water.

## 3.2. Results and Discussion

### 3.2.1. Design of Peptide Amphiphile:

The peptide amphiphile **1** was designed by tethering a hydrophobic fluorenylmethyloxycarbonyl (Fmoc) group at the N-terminal and two hydrophilic lysine units at the C-terminal of a short peptide sequence <sup>N</sup>VFFA<sup>C</sup> (Scheme **3.1**). Peptide was purified using RP-HPLC and was further confirmed using ESI-MS. The Fmoc-VFFA and the protonated lysine moieties maintain hydrophobic-hydrophilic balance to make **1** to self-assemble in water (pH= 6). The attractive hydrogen bonding among the amide functionalities and  $\pi$ - $\pi$  stacking interactions among the aromatic moieties promote parallel stacking of the amphiphiles to form secondary structures. To erase any pre-assembly history, **1** was isolated from dimethyl formamide (DMF) from its molecularly dissolved state.





**Scheme 3.1.** Chemical structure of the peptide amphiphile **1**.

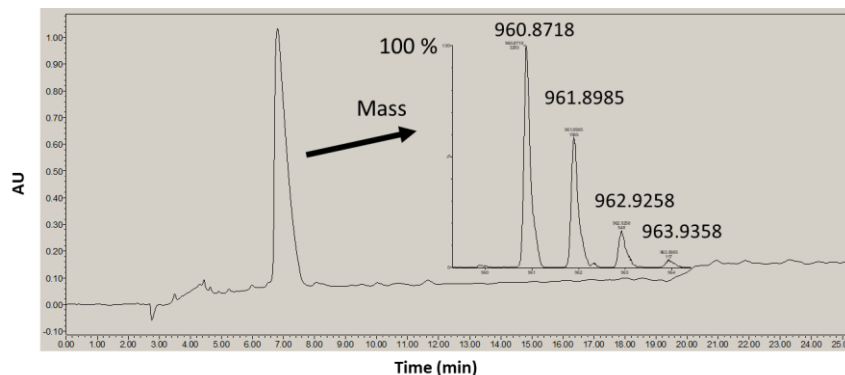


**Figure 3.1.** HPLC chromatogram showing the purity of the synthesized peptide **1** with Mass spectrometry data inset.

### 3.2.2. Self-assembly:

**3.2.2.1. Circular Dichroism (CD) Spectroscopy:** CD spectroscopy is a particularly powerful technique for studying proteins and peptides, as different types of secondary structure exhibit very different spectra in the far-UV region (190-250 nm). Left-handed and right-handed circularly-polarized light may be absorbed to different extents if the sample is optically active. This difference generates a CD spectrum containing peaks and troughs around the absorption wavelengths.

Here, temperature-dependent self-assembly of **1** in water was investigated. At 10 °C, the spectrum shows a strong negative band with multiple minima ( $\lambda = 205, 208$  and 210 nm) and a weak negative band ( $\lambda = 235$  nm) indicating a random coil structure (Fig. 3.2). With increasing temperature in the range of 25-50 °C, the CD signature changes to a characteristic  $\beta$ -sheet structure with a strong negative band at 211 nm and a positive band at 197 nm. Upon further increase in the temperature from 50 °C to 80 °C, the negative band

at 211 nm exhibits bathochromic shift to 216 nm with decrease in intensity and a strong positive band ( $\lambda = 200$  nm) appears indicating the formation of a twisted  $\beta$ -sheet secondary

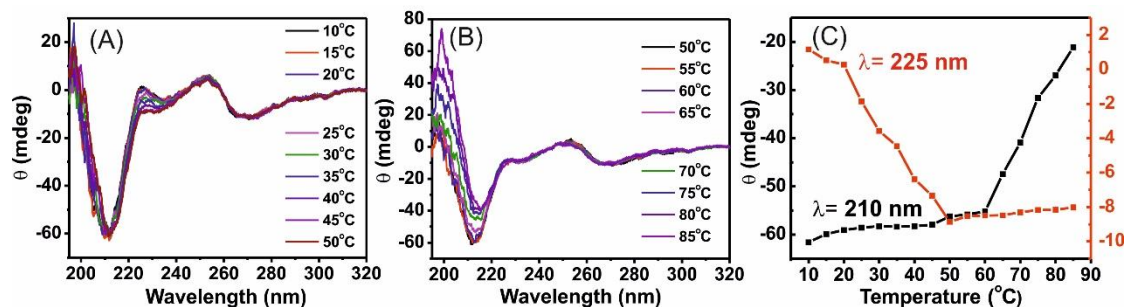


**Figure 3.2.** CD spectra of peptide **1** with a stepwise increase in temperature. CD spectra in the range of (A) 10°C to 50 °C shows a bathochromic shift at  $\lambda = 210$  nm and (B) 50°C to 85°C shows a decrease in the intensity of the CD signal at  $\lambda = 216$  nm, (C) Temperature dependent CD analysis at  $\lambda = 210$  and 225 nm.

structure (Figure 3.2B). The change in the intensity of the bands at  $\lambda = 210$  nm and 225 nm with temperature clearly indicates first transition from random coil to  $\beta$ -sheet structures at  $\sim 20$  °C and second transition from ordered  $\beta$ -sheet to twisted  $\beta$ -sheet structures in the range of 55 °C to 60 °C (Figure 3.2C).

**3.2.2.2. Microscopic investigation:** Shape of the self-assembled nanostructures were studied using Atomic Force Microscopy (AFM) which is a versatile and powerful

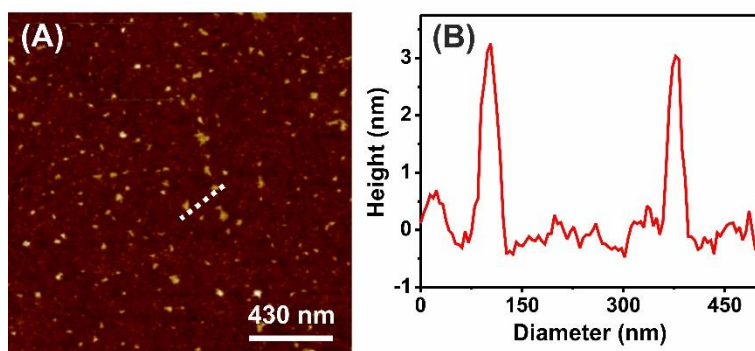


**Figure 3.3.** AFM height images recorded after incubating an aqueous solution of **1** (150  $\mu$ M) at 10 °C for 30 min (A) showing the formation of nanoparticles, (B) height profile of the nanoparticles with height of  $\sim 3-4$  nm.

microscopy technique for studying samples at nanoscale. Tapping mode AFM height images corroborated the presence nanoparticles with height of ~3-4 nm and diameter ranging from 30-40 nm at 10 °C (Figure 3.3). Time dependent stability of these nanoparticles were investigated by recording AFM images at various time intervals and it was found that the nanoparticles remain in shape (Figure 3.4) for 5-6 h at 10 °C.

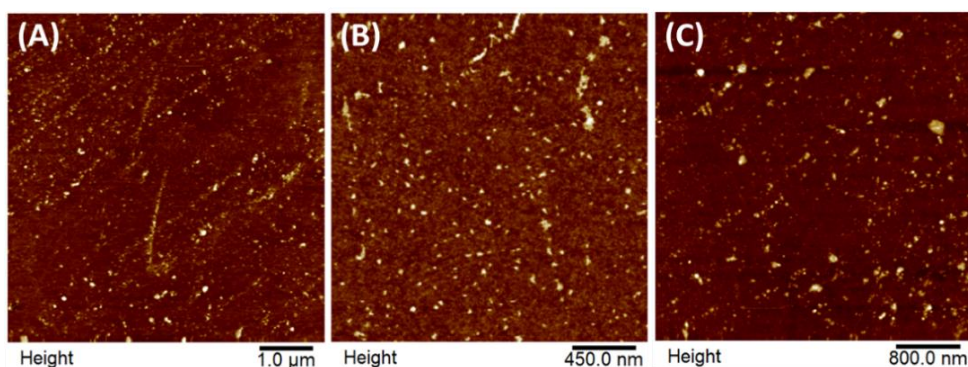


**Figure 3.4.** AFM images of peptide **1** (0.15 mM) in water at 10°C. 10  $\mu$ L of the solution was drop casted on silicon wafers after (A) 10 min (B) 2 h and (C) 6 h. The results shows the stability of the nanoparticles in water at 10°C.

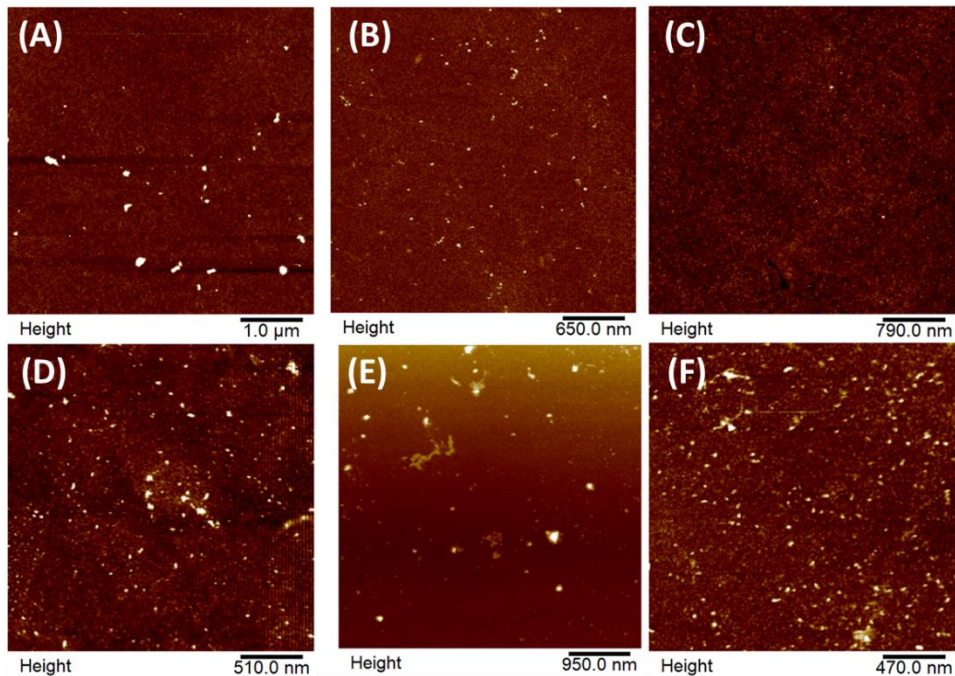


**Figure 3.5.** AFM height images of peptide **1** (0.15 mM) in a mixture of DMF-Water (A) 1:3 (B) 1:1 (C) 3:1 at 10 °C after an incubation period of 2 h and (D) 1:3 (E) 1:1 (F) 3:1 at 25 °C after an incubation period of 2 h.

Peptide was dissolved in dimethyl formamide (DMF) to form stock solution of 20 mM at 10 °C. 3.76 mL of the stock was added to 0.5 mL of water and mixture of DMF-water (v/v) in the ratio 1:3, 1:1, 3:1 at 10 °C. At this temperature in all the cases, formation of the metastable nanoparticles. However, the nanoparticles in DMF-water does not show any change in shape even at 25 °C over 24 h (Figure 3.4). As the DMF in water was increased from 1:3 to 3:1, the stability of the nanoparticles were arrested for longer time period even at 25 °C instead of 10 °C as shown in Figure 3.5. In 100% DMF, the peptide **1** was completely soluble and is in its molecularly dissolved state as a consequence of destruction of all the hydrogen bonding and hydrophobic  $\pi$ - $\pi$  interactions present between them.

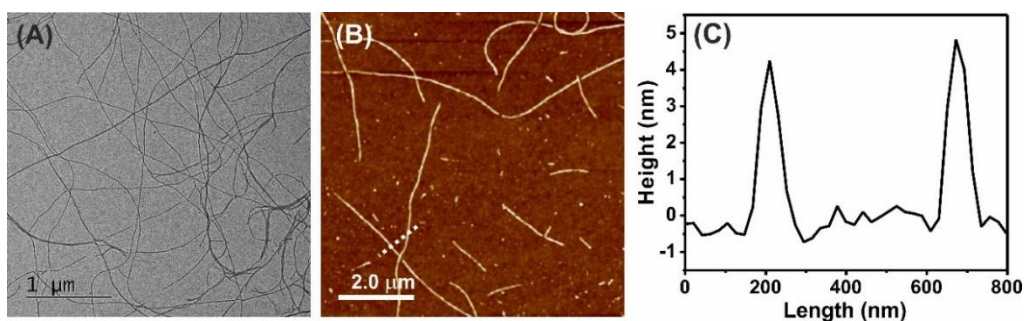


**Figure 3.6.** Single fibers of peptide **1** recorded after incubating an aqueous solution of **1** (150  $\mu$ M) at 25 °C, pH 7.0 for 30 min as shown by (A) TEM image (diameter of 8-9 nm), (B) AFM image and (C) height profile of the single fibers with height of 4-5 nm.

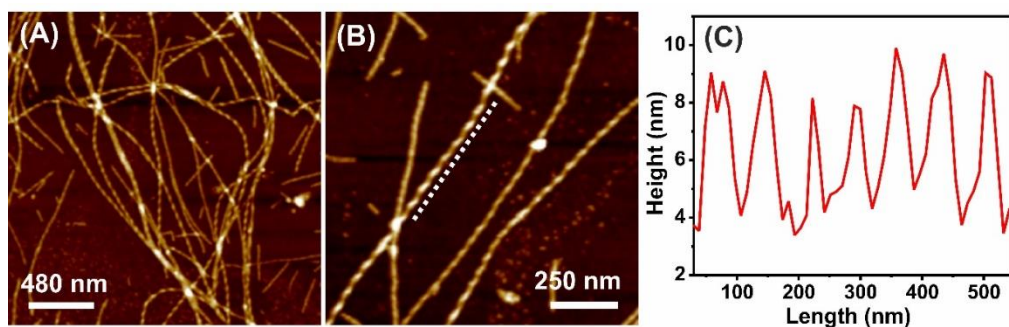


**Figure 3.7.** AFM image showing helical twisted bundle (A), and (B) of peptide **1** obtained after heating at 85 °C followed by cooling to room temperature. (C) The change of height along the bundle trajectory shows up and down by 4 nm.



Upon increasing the temperature of the peptide nanoparticle solution to 25 °C, the nanoparticles in water were transformed into nanofibers within 30 min as observed from negatively stained TEM image and AFM height image (Figure 3.6). On analysis, the nanofibers show diameter of ~ 8-9 nm and height of ~ 4-5 nm. Upon further increasing the temperature of nanofibrous solution to 70 °C, followed by a gradual cooling to 25 °C, the nanofiber turned into helical twisted bundles with its pitch of ~40-55 nm (Figure 3.7). This was in corroboration with the red shift in the CD band (Figure 3.2C), owing to the alteration in the packing of the aromatic residues.<sup>[12,27]</sup> Upon repeated heating-cooling the shape of the helical bundles remained unchanged, indicating the thermodynamic nature of the bundles. Colour contrast AFM height image shows the clear visual difference in the twisted bundles

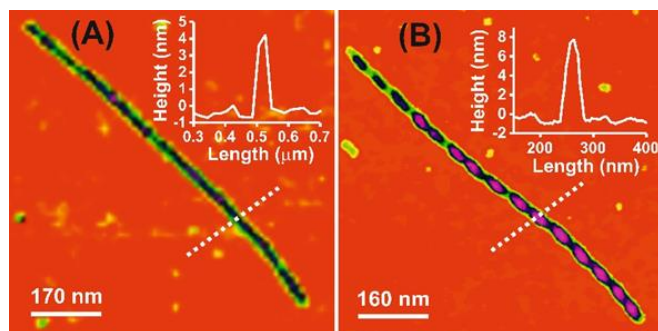


**Figure 3.8.** Comparison of colored AFM height image across the (A) nanofibers (~4 nm) (B) twisted bundles (~8 nm).

as compared to single nanofiber. Height of the twisted bundle at twisted site is ~8 nm which is double of the height of single kinetic nanofiber shown in Figure 3.8 where two fibers are inter-twinned to each other to form the helical twisted bundle.

**3.2.2.3. Binding to Thioflavin-T:** The binding of thioflavin-T (Th-T) to amyloid nanostructures can be detected using fluorescence spectroscopy. Th-T undergoes excitation at 440 nm and gives rise to enhanced emission band at 480-500 nm when bound to an ordered secondary structures of proteins, peptides. Th-T binding to one dimensional ordered supramolecular fibers, twisted bundles with  $\beta$ -sheet secondary structures showed much

higher emission intensity as compared to that of metastable nanoparticle, indicating the formation of long-ordered assemblies containing  $\beta$ -sheets (Figure 3.9).

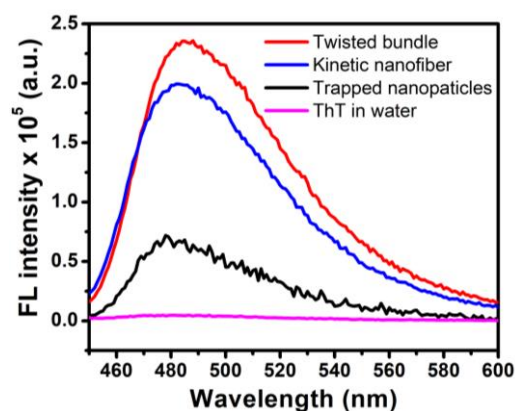


**Figure 3.9.** Fluorescence emission spectra as a consequence of Th-T binding to the twisted bundle, single nanofiber and nanoparticle (1 mM). Control experiment was performed by adding Th-T in water.

**3.2.2.4. Small angle X-ray scattering (SAXS):** The SAXS profiles obtained from nanofibers of **1** were fitted with a model for non-interacting cylinders with a monodisperse cylindrical form factor, which gave core-shell micellar rods of diameter 9.4 nm, with a core radius of 2.1 ( $\pm 0.2$ ) nm and shell thickness of 2.6 ( $\pm 0.2$ ) nm (Figure 3.10A), in agreement with the diameter observed from the microscopic images. Furthermore, the fit of the SAXS data for the twisted bundles yielded a length scale of 40 nm (Figure 3.10B) which corroborates the pitch as observed from AFM.

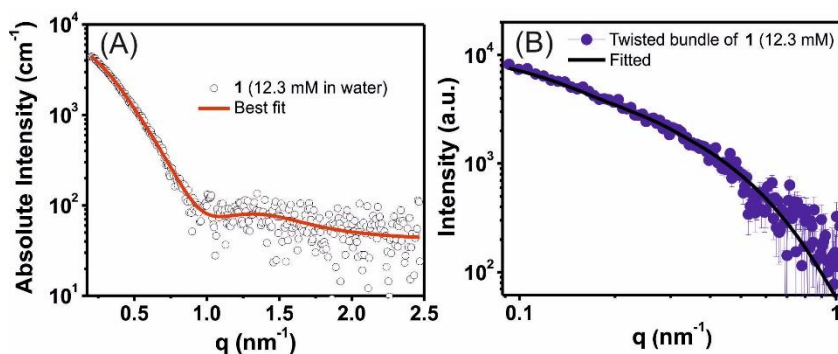


**Figure 3.10.** SAXS profile for (A) aqueous solution, (B) twisted bundle of **1** (12.3 mM) at 25 °C, pH = 7.

### 3.2.3. Nucleation mediated growth: Seeded Supramolecular Polymerization (SSP)

The length of the fibers as observed from AFM images is quite polydisperse with PDI  $\sim 1.52$  (Figure 3.11A), which is still superior to thermodynamically controlled supramolecular polymers (PDI  $\sim 2$ ). The kinetic evolution of the nanofibers prompted us to perform seeded supramolecular polymerization. In this technique, supramolecular polymers with narrow PDI can be produced by addition of short seeds to a solution of metastable species or monomers. In a bid to achieve the uniform length distribution of the fibers, we resorted to shear mediated fiber breakage to produce short nanofiber fragments with active ends. These short fragments (i.e. seeds) will act as nucleating core for the growth of supramolecular fiber. The fibrous solution was either probe-sonicated for 10 min or stirred at  $\sim 1500$  rpm for 3 days to produce shorter fibers with narrow PDI (1.05-1.08), as evident from the number average length ( $L_n$ ) and weight average length ( $L_w$ ) values albeit in different length regimes (Figure 3.11B-C). However, on heating to  $70$   $^{\circ}\text{C}$  followed by cooling to  $25$   $^{\circ}\text{C}$ , the stirred nanofiber seeds transformed into twisted bundles (Figure 3.12), with compromise in the PDI value

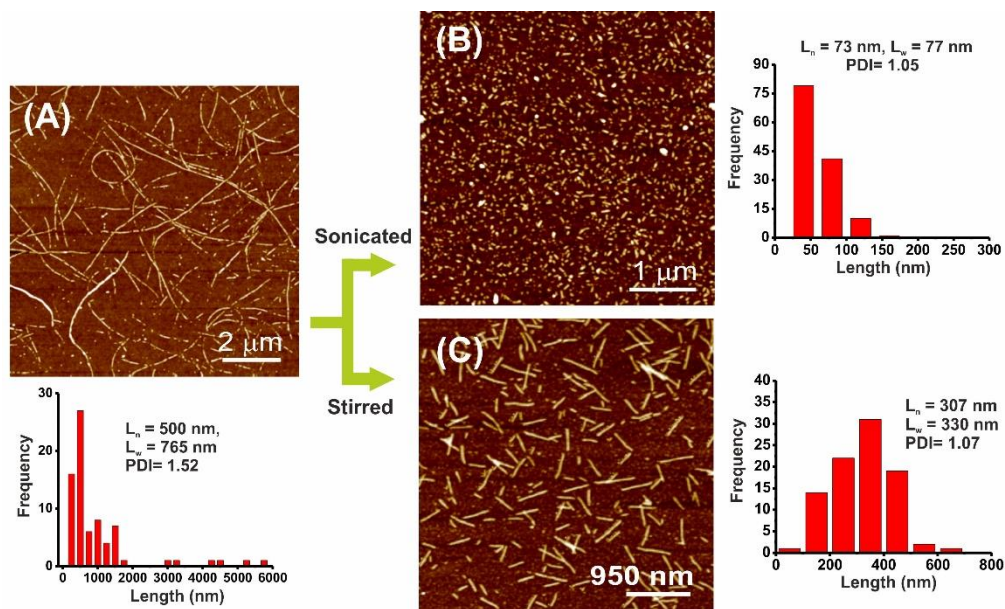


**Figure 3.11.** AFM image showing (A) polydisperse kinetic nanofibers of **1**, generation of short seeds with narrow PDI by (B) probe sonication ( $L_n = 73$  nm, PDI = 1.05) and (C) stirring in IKA magnetic stirrer at  $\sim 1500$  rpm, 3 days ( $L_n = 307$  nm, PDI = 1.07).

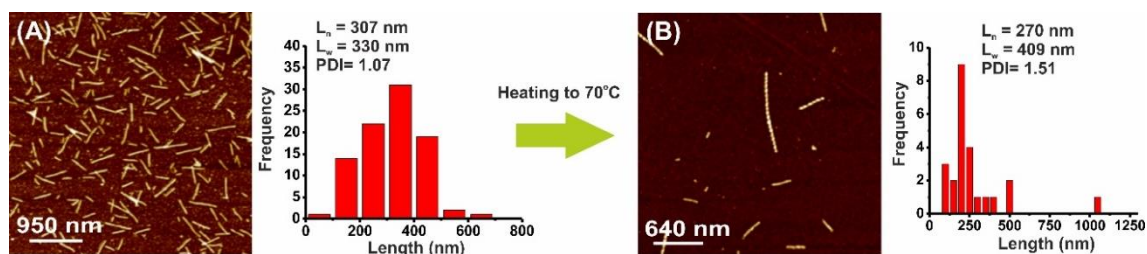


**Figure 3.12.** AFM image showing seeds obtained by (A) mechanical stirring of the nanofibrous solution of **1** generates short nanofibrous seeds ( $L_n = 307$  nm, PDI = 1.07). (B) Stirred seeds after heating at 70 °C followed by cooling it to 25 °C results in twisted bundle short seeds ( $L_n = 270$  nm, PDI = 1.51). Number average ( $L_n$ ), weight average ( $L_w$ ) lengths and PDI of the corresponding seeds were obtained from analyzing the histograms of length distribution.

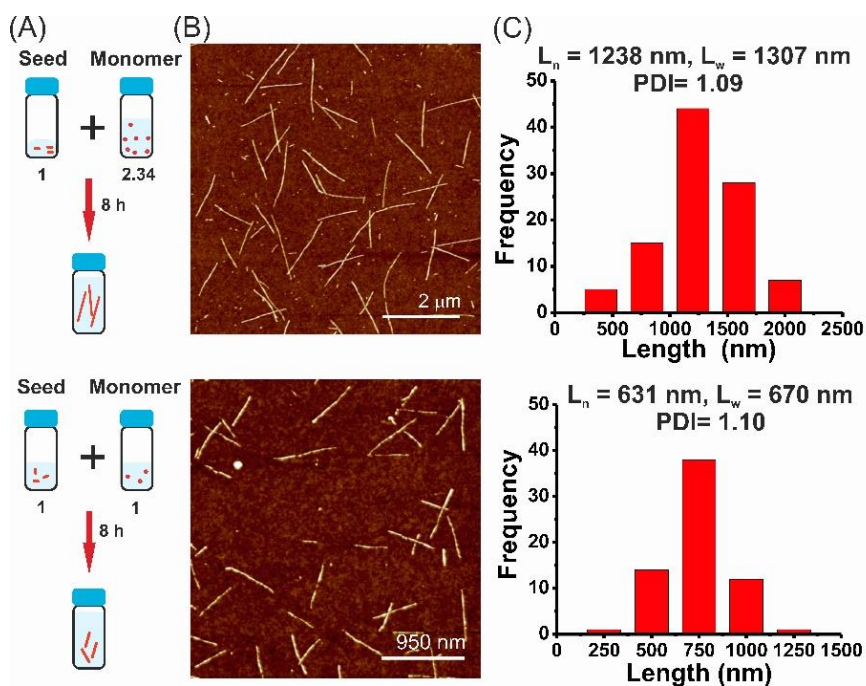


**Figure 3.13.** Nucleation mediated fiber growth using different percentage of seed to freshly prepared monomer solution of **1** in water at pH = 7 at 15 °C. (A) Cartoon image showing seeding mediated growth of the fiber, (B) weight average ( $L_w$ ) fiber length and PDI after adding and incubating 2.34 and 1 equivalent of the monomer to the seeds. AFM images of fibers and (C) histogram analyses depicting fiber length distribution with number average ( $L_n$ ) and weight average ( $L_w$ ) fiber length and PDI after adding and incubating 2.34 & 1 equiv. of the monomer to the seeds.



(1.51). This implies possible recombination of fibers during the annealing process. The length distribution of the seeds, incubated at 25 °C did not change over a period of 3 days, which provides a convenient time frame for the seed-mediated fiber growth.

Different ratios of seeds ( $L_n = 307$  nm) and monomer were mixed and the fibers were allowed to grow un-agitated at 15 °C (Figure 3.13A). Length distribution analysis based on the AFM images reveals a linear correspondence between the seed-monomer ratio and average length obtained after 8 h with PDI in the range of 1.09-1.16 (Figure 3.13B, C). For example, a 1: 2.34 ratio of seed: monomer gives a longer fiber as compared to a 1:1 ratio of seed: monomer when incubated at 15 °C without any agitation for ~8 h. Addition of metastable nanoparticles to short probe sonicated seeds ( $L_n = 73$  nm, PDI = 1.05) in different ratios of nanofiber seeds 9:1, 1:1, and 0.43:1 yield different length regimes of the nanofibers as shown in Figure 3.14.

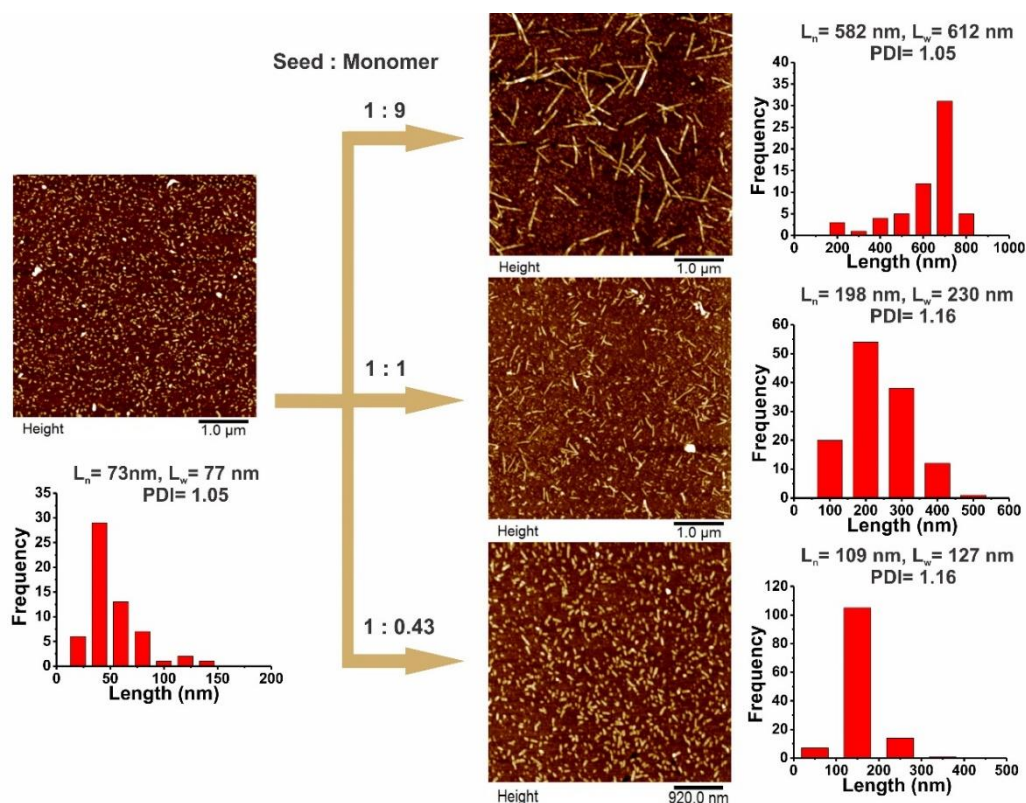


**Figure 3.14.** Seeded supramolecular polymerization (SSP) using different ratios of probe sonicated short nanofiber seeds and metastable nanoparticles of **1** to get different length distributions of fibers.

When twisted bundle seed solution was added to monomer (1:1), they furnish twisted bundles only with a higher length scale (Fig. 3.15). Thus, seed morphology plays a crucial role in deriving same kind of morphology. Addition of monomeric solution to nanofiber seeds and twisted bundled seeds results in nanofibers and twisted bundle respectively with required length distribution depending on the respective seed to monomer ratio. To ascertain the living nature of the fiber ends, nucleation and fiber elongation were performed with the

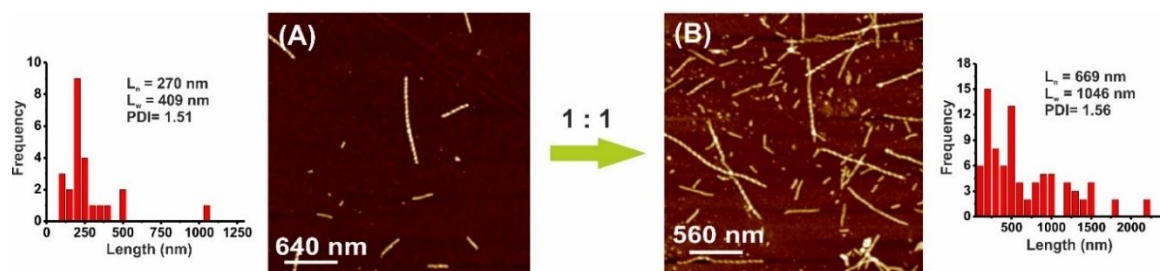


**Figure 3.15.** Seeded supramolecular polymerization (SSP) involving twisted bundle as seed with monomer in the ratio 1:1.

sequential addition of the freshly prepared monomer to fiber seeds result in a stepwise increase in the length of the fibers. The fibrous solution of **1** was probe sonicated for 5 minutes at an amplitude of 20 to obtain seeds of  $L_n = 112$  nm, PDI = 1.03. Short fiber seeds ( $L_n = 112$  nm) was incubated un-agitated with freshly dissolved peptide solution in 1:1 ratio at 15 °C for a day. The growth of the nanofibers was monitored by recording AFM at different intervals of time for 24 h (Figure 3.16). The fiber length distribution with time was analyzed to get a saturation plateau of fiber growth ( $L_n = 216$  nm, PDI = 1.05) marking as end of Cycle 1. The fibers with  $L_n = 216$  nm were used as seeds against monomer nanoparticles and entire process of fiber growth was monitored (Cycle 2) and the fiber growth levels off with  $L_n = 455$  nm, PDI= 1.06. Samples were allowed to incubate for 24 h which provide a sufficient time period for fiber length growth. The process was repeated for cycle 3 and obtained fibers with  $L_n = 808$  nm, PDI = 1.18 (Figure 3.17A). The dimensions of the monomer and seed remained constant over the same period. AFM analysis suggests two fold increase in the fiber length with a narrow PDI value with each monomer addition. This suggest that the ends of the kinetically controlled peptide nanofibers remains as active

and living end and grows upon addition of monomer.  $L_n$  and  $L_w$  of different length regimes obtained after equimolar addition of monomer to seeded cycle were plotted (Figure 3.17B)

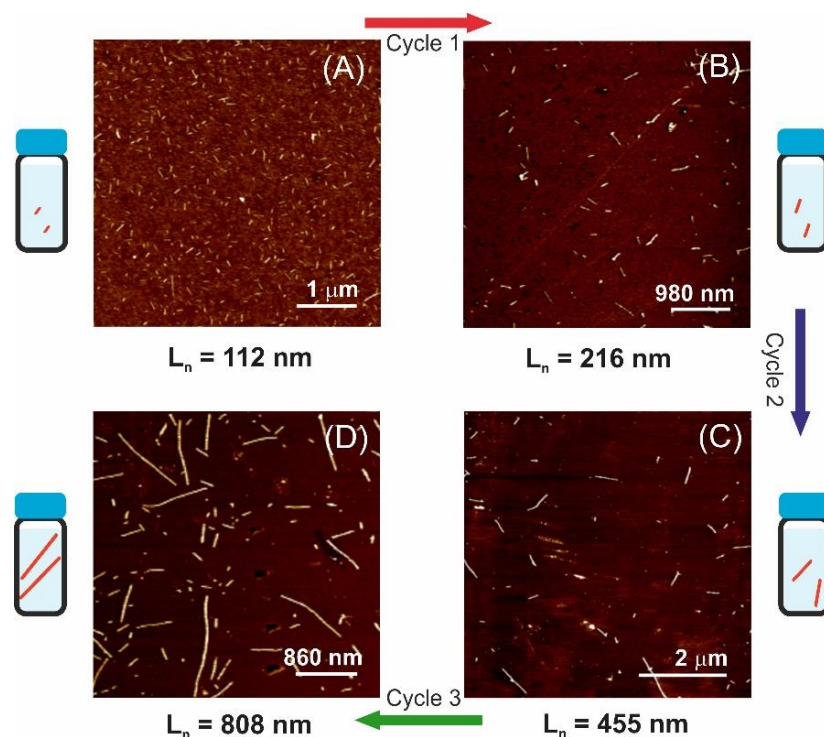


**Figure 3.16.** Living supramolecular polymerization and growth of kinetically controlled peptide nanofibers upon sequential addition of monomer to the seeds in the ratio 1:1 in water. (A-B) AFM image showing growth of the kinetically controlled nanofibers in cycle 1-3 with stepwise increase in the average length ( $L_n$ ) after a day.

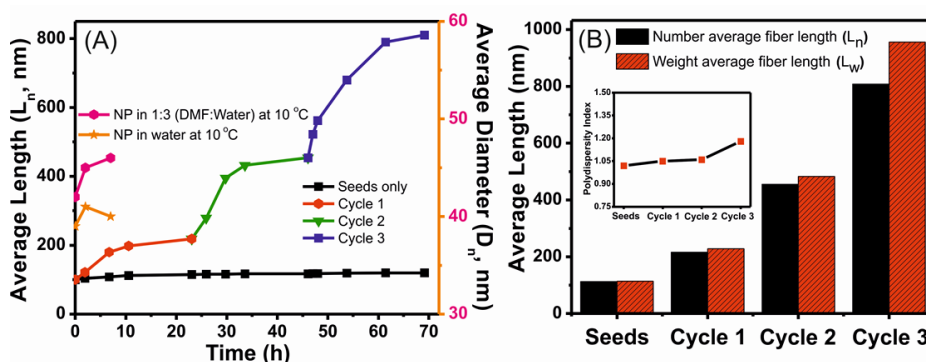


**Figure 3.17.** Living supramolecular polymerization and growth of the supramolecular fiber of **1** upon sequential addition of the monomer. (A) Average dimensions ( $D_n$  and  $L_n$ ) of nanoparticles and nanofibers with time upon sequential addition of monomer in three cycles. (B) Weight average length ( $L_w$ ) and number average length ( $L_n$ ) and PDI (inset) of the seeds and the fibers upon successive addition of the monomer.

with almost no change in the PDI (3.17B inset) provides a stability of the grown fibers with no secondary nucleation driven fiber growth.

The rate of each step depends on the number of fiber ends that remains same for all the cycles (Figure 3.18). This clearly indicates that the ends of the fibers remains active and grow via a nucleation mechanism on subsequent addition of the monomer.

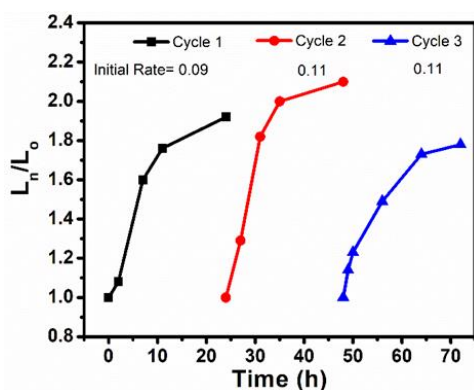
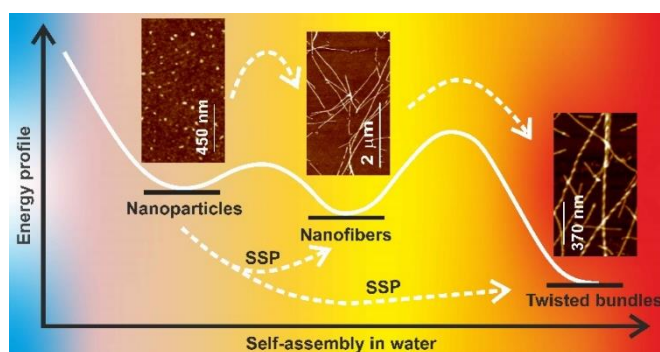


**Figure 3.18.** Calculation of initial rate from the plot of  $L_n/L_0$  vs time for the three cycles of living supramolecular polymerization.

To brief the above results, a stepwise self-assembly of peptide **1** is discussed with increase in temperature, with metastable nanoparticles at 10 °C, kinetic nanofibers at 20 °C, and twisted bundles beyond 50 °C (Scheme 3.2). Mediation of seeded supramolecular polymerization furnishes nanofibers and twisted bundles on addition of short fiber seeds and twisted bundle seeds to the metastable nanoparticles respectively with narrow polydispersity index values.



**Scheme 3.2.** A representative scheme showing the morphological change on change in temperature. Seeded supramolecular polymerization results in the formation of nanofibers and twisted bundles of **1**.

### 3.2.4. Hydrogel network formation:

The peptide fibers are positively charged at physiological pH due to protonation of lysine side chain. Addition of sodium phosphate buffer (SPB, 10 mM, pH= 7) transformed

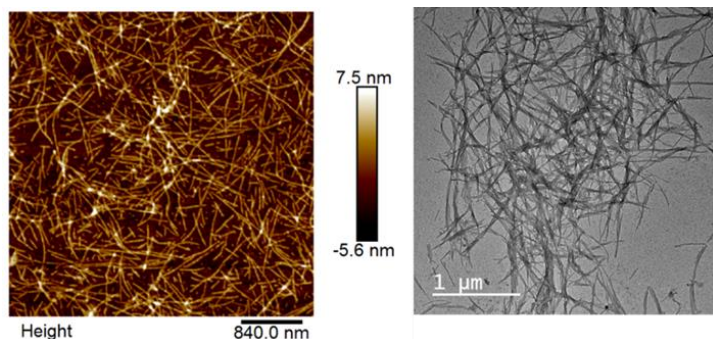


**Figure 3.19.** AFM and TEM image of the hydrogel of peptide **1** in SPB showing entanglement network of the uncontrolled peptide fibers.

the peptide solution into a hydrogel via physical cross-linking of the fibers with negatively charged counter anions.<sup>[28]</sup> The Guinier plot in the low  $q$ -regions is linear for the semi-flexible filaments of **1**; however, upon crosslinking the plot deviates from linearity (Figure 3.20), which is a characteristic signature of agglomeration mediated by interfiber ion-bridging by counter anions.<sup>[29]</sup>

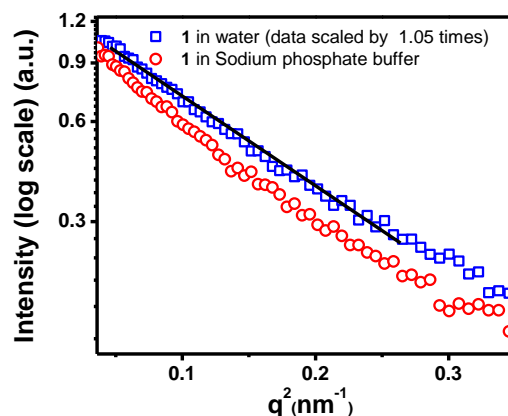


**Figure 3.20.** SAXS profile for aqueous solution and the hydrogel (12.3 mM) of **1** in 10 mM SPB.

A number of counter anions of the Hofmeister series ( $\text{SO}_4^{2-}$ ,  $\text{OAc}^-$ ,  $\text{Cl}^-$ ) ( $c = 10$  mM) with varied ionic strength were used to for crosslinking the uncontrolled peptide fibers and



investigate the cross-linking efficacy over the mechanical strength of the resulting hydrogel networks. The peptide **1** ( $c = 8.4 \text{ mM}$ ) was dissolved in different divalent or weaker ionic strength monovalent anionic solutions at pH 7. Sodium sulfate with higher ionic strength led to the entanglement of the nanofibers, turning free-flowing solution into hydrogels as depicted by frequency independent behavior in oscillatory rheological studies (Figure 3.21).

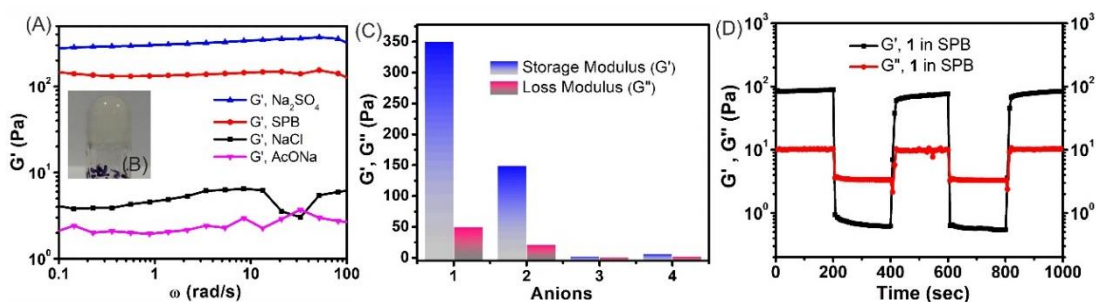


**Figure 3.21.** (A) Storage modulus ( $G'$ ) of the frequency sweep oscillatory rheology for the networks formed by addition of different counter anion (10 mM) to positively charged peptide nanofibers of **1**. (B) Inset as representative image of an inverted vial containing hydrogel of **1** in sodium phosphate buffer (10 mM). (C) Bar diagram showing comparison of storage and loss moduli for the resulting networks (1=  $\text{Na}_2\text{SO}_4$ , 2 = SPB, 3= NaOAc, 4= NaCl). (D) Thixotropic studies for the hydrogels of **1** in SPB. Black and Red color indicate storage modulus ( $G'$ , Pa) and is loss modulus ( $G''$ , Pa).

However, the addition of sodium acetate or sodium chloride solution resulted in a relatively weak gel or viscous solution. The hydrogels are self-healing in nature owing to the presence of sticky hydrophobic segments.<sup>[30]</sup> Next, the mechanical behavior of the hydrogels obtained from nanofibers and twisted bundles were compared, which showed that the  $G'$  value of

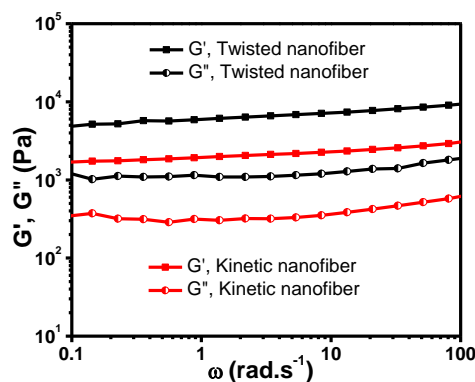


**Figure 3.22.** Frequency sweep oscillatory rheology for the hydrogels (1 w/v %, pH =7) obtained by physical cross-linking the kinetic nanofibers and thermodynamically stable twisted bundles.

the twisted helical bundles is 3 times higher than that of kinetic single fibers of **1** (Figure 3.22). The bundling increases the stiffness of the fibers resulting in enhanced elastic modulus values. Using seeded supramolecular polymerization, we grew fibers in a controlled manner with varying equivalent of monomer (0, 0.43, 1, 2.34, and 9) to achieve fibers with average lengths ( $L_n$ ) of 140, 287, 332, 622 and 1157 nm respectively.

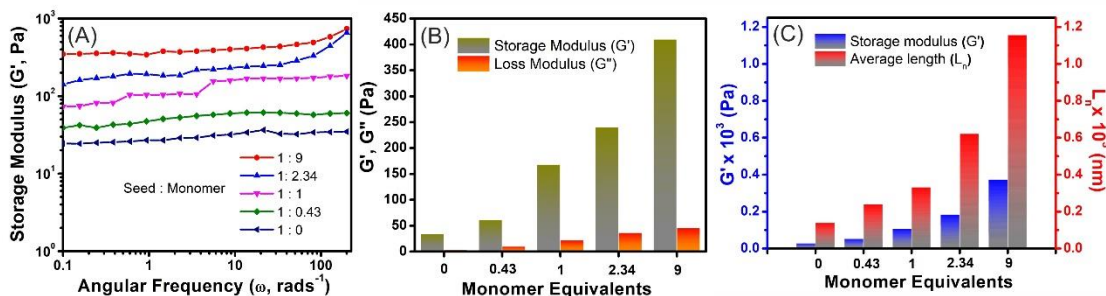


**Figure 3.23.** Rheological characterization for hydrogels of **1** after cross-linking the seeded fibers with sodium phosphate buffers at pH 7.0. (A) Storage moduli ( $G'$ ) from the frequency sweep oscillatory experiment on the hydrogels obtained from fibers seeded with monomer equivalents of 0, 0.43, 1, 2.34, and 9. (B) Bar diagram showing storage and loss moduli for the resulting hydrogel networks. It was measured using CP-25-2 on rheometer at a constant strain of 0.01% at 25 °C. (C) Bar diagram showing the correlation of average length of the nanofiber ( $L_n$ ) with the storage modulus of the cross-linked hydrogels. The fibers were grown by adding 0, 0.43, 1, 2.34 and 9 equivalent of monomers to seed. A constant angular strain was maintained at 0.1%.

The mechanical properties of the resulting hydrogels upon cross-linking the fibers, showed a direct correlation of the elastic moduli with the average length of the fibers. Longer fiber length assist hydrogel formation with higher mechanical strength due to the presence of more number of inter-fibrillar entanglement sites. Thus, 1:9 ratio of fiber seed to monomer ratio results in stronger hydrogel with storage modulus ( $G'$ , Pa) greater than loss modulus ( $G''$ , Pa) as compared to the others with shorter length regime (Figure 3.23).

The persistence length ( $L_p$ ) of the peptide fibers is  $\sim 1.4 \mu\text{m}$ , comparable to that of the actin filaments ( $1.5 \mu\text{m}$ ). When the average fiber length is more than the entanglement length ( $L_e = 756 \text{ nm}$ ), the cross-linked fibers form an efficient entangled network through increasing number of crosslinking sites as corroborated from AFM and rheology. Such interfiber

crosslinking follows a continuum model of bundling coupled with an energetic model of elastic rods. The mechanical tunability of the hydrogels is a result of the length dependent network elasticity, which is similar to natural bio-filaments e.g. collagens.<sup>[31,32]</sup>

### **3.3. Conclusions**

The study demonstrated a pathway dependent stepwise self-assembly in an amyloid inspired short peptide amphiphile. At low temperature, CD and AFM showed formation of metastable nanoparticles in an aqueous medium and mixture of water-DMF, which get converted into kinetically controlled long nanofibers upon increasing the temperature (~20 °C). The nanofibers are stable at ambient temperature, however, beyond 50 °C they transform into thermodynamically stable twisted bundles. Selection of the right kind of seeds promotes the growth of nanofibers or twisted bundles via seeded supramolecular polymerization with excellent control over the length. Importantly, these peptide fibers and bundles can further be physically cross-linked to render a hydrogel network. The length distribution and history of the peptide fibers play a significant role in determining the mechanical stiffness of the resulting hydrogels. This work establishes a new strategy to control the properties of hydrogels combining the advantages of multiple pathways and seeded supramolecular polymerization. It opens a new paradigm to relate the design and functional properties of multi-component and biologically relevant networks from short peptide fragments.

### **3.4. Experimental Section**

#### **3.4.1. Materials:**

All Fmoc protected amino acids, activator (diisopropyl carbodiimide), piperazine, triisopropylsilane, anisole, 1,2-ethanedithiol and thioflavin-T were purchased from Sigma Aldrich. Oxyma, Fmoc-Rink amide MBHA resin was purchased from Merck. HPLC grade Acetonitrile, HPLC water, ethanol and DMF were obtained from Merck. Trifluoroacetic acid was purchased from SRL. Sodium salts were purchased from HIMEDIA.



### **3.4.2. Methods:**

Solid Phase Peptide Synthesis was performed in Liberty Blue CEM, Matthews, NC, USA and the synthesized peptide was characterised using reverse phase C18 column Waters HPLC coupled with Q-TOF MS detector. CD spectra were recorded using JASCO J-1500 Circular Dichroism Spectrometer, Easton, MD, USA. The wavelength range was selected from 195 nm to 350 nm with a scan speed of 100 nm min<sup>-1</sup> using 2 mm path length CD quartz cuvette. Fluorescence emission spectras were recorded using FS5 spectrofluorometer from Edinburgh instruments. Wavelength range was selected from 450 nm to 600 nm with scan slit and offset slit of 1 mm each with dwell time of 0.1 s at 25 °C. The Samples were drop casted on silicon wafer and AFM height images were recorded using tapping mode on a Bruker Multimode 8 scanning probe microscope with silicon cantilever. TEM images were recorded using JEOL JEM 2100 TEM with a Tungsten filament at an accelerating voltage of 120 kV. SAXS experiments were carried out on SAXSess mc<sup>2</sup> instrument (Anton-Paar) with line-collimation system using a Cu K $\alpha$  source with wavelength of 1.54 Å. Perkin Elmer cyclone image plate recorder was used to record the data. SAXSQuant 2D software was used to reduce the two dimensional data to one dimensional, Intensity (I) vs scattering vector (q) plot. PDDF curves were obtained by using GIFT software. The linear viscoelastic region, storage modulus, loss modulus and thixotropic studies were calculated using a Rheoplus 302 (advanced Rheometer) device using cone plate (CP25-2) geometry at measuring distance of 0.172 mm at 25°C.

#### **3.4.2.1. Synthesis of peptide 1:**

Microwave Automated Solid Phase Peptide Synthesizer (Liberty Blue CEM, Matthews, NC, USA) was used to synthesize peptide **1**. Fmoc-Rink Amide MBHA Resin was first swelled in dimethylformamide (DMF) for 30 minutes. All Fmoc protected amino acids were weighed as per the required scale of the reaction followed by dissolving in required DMF solution. Deprotection of Fmoc group from the amino acid was achieved by using 20% piperazine in DMF containing 10% ethanol in the microwave reactor. Diisopropyl carbodiimide (DIC, activator) and Oxyma Pure (activator base) in DMF, were

used as activators for the coupling reaction between acid and amine to form the peptide bond. A cycle of coupling, deprotection steps was repeated to synthesize the required peptide anchored to the resin. The peptide was cleaved from the resin upon a slow shaking with a cocktail solution, a mixture of trifluoroacetic acid (TFA)/triisopropylsilane (TIPS)/water/1, 2-ethanedithiol (EDT) (95: 2: 2: 1, v/v/v/v) for 3 h at room temperature. The resin was then filtered off and the filtrate solution containing desired peptide was evaporated to remove the TFA. The resultant solution was dropwise added to pre-chilled diethyl ether to precipitate peptide **1** that was dried to obtain white powder. The peptide was purified using a Waters Semi-Preparative binary HPLC system using a C<sub>18</sub>-reverse phase column with an acetonitrile-water mobile phase containing 0.1% TFA. The purified peptide was confirmed by ESI-MS recorded with Waters HPLC Q-TOF mass instrument. LCMS (ESI) m/z: C<sub>53</sub>H<sub>69</sub>N<sub>9</sub>O<sub>8</sub> calculated 960.1708 g/mol; found 960.8718 g/mol.

**3.4.2.2. Atomic Force Microscopy (AFM):** Sample preparation at low temperature was performed by placing silicon wafer on a cold water maintained at 10 °C. 10 µL of 0.15 mM of the peptide solution was drop casted on silicon wafer. After 5 minutes, the silicon wafer was washed with 500 µL water using micropipette to remove excess peptide. The silicon wafer was then left to be air dried in a desiccator. AFM height images were recorded by tapping mode on a Bruker Multimode 8 scanning probe microscope with silicon cantilever (Bruker).

**3.4.2.3. Transmission Electron Microscopy (TEM):** 6 µL of 2 µM aqueous peptide solution was drop casted on a 300 mesh carbon-coated copper grid. After ~ 5 min, excess solution was blotted using watmann filter paper. 6 µL of uranyl acetate solution (1.2 w/v %) was then added for negative staining and incubated for 4-5 minutes at room temperature. Extra solution was the wicked off by watmann filter paper carefully and grid was then dried in the desiccator under vacuum. TEM images were recorded using JEOL JEM 2100 with a Tungsten filament at an accelerating voltage of 120 kV.

#### **3.4.2.4. Generation of Seeds by mechanical agitation:**

- a) Seeds from mechanical stirring:** 500  $\mu\text{L}$  of pre-assembled kinetic nanofibrous solution of peptide **1** (4 mM) was taken in 2 mL eppendorf and was kept on stirring at  $\sim 1500$  rpm for 3 days using IKA magnetic stirrer. The formation of the short seeds were monitored by checking the AFM of the samples.
- b) Seeds from probe sonication:** To get even shorter fiber seed, 500  $\mu\text{L}$  of pre-assembled nanofibrous solution of peptide **1** (4 mM) was taken in 2 mL eppendorf which was fixed with a stand in a glass beaker having ice cold water. Then probe microtip (4417 number) was dipped into the sample and was sonicated using QSonica (model number Q700, power 700 watts and frequency 20 kHz) at an amplitude of 20 % for  $\sim 10$  minutes (5 sec on and 5 sec off to avoid heating due to the probe).

**3.4.2.5. Analysis of average length from AFM images:** AFM images were recorded for the short seeds and fibers emanating from different ratio of seeds and monomers. 100 random fibers were selected from different areas of the images and a histogram was generated by choosing bin and frequency in Microsoft Excel. The average length and PDI were estimated by calculating number average fiber length ( $L_n$ ) and weight average fiber length ( $L_w$ ) and the ratio  $L_w/L_n$ .

**3.4.2.6. Seeded Supramolecular Polymerization:** Seeded supramolecular polymerization (SSP) was performed taking different ratio of the kinetic nanofiber seeds and metastable nanoparticles (Table 3.1) as monomers at  $15\text{ }^\circ\text{C}$  to furnish different length distribution of the fibers. A control experiment without the seeds yielded uncontrolled fiber lengths with high PDI value. In absence of the monomer, the length distribution of the seeds remains unchanged even after 4 days. In an separate experiment, thermodynamically controlled twisted bundle was used as seeds to the monomers with 1: 1 ratio at  $15\text{ }^\circ\text{C}$  to furnish twisted bundles with higher length scale.

**Table 3.1.** Table showing different ratios of seed and monomer of **1** taken for SSP.

S.No.	Seed : Monomer	Volume of short seed solution ( $\mu\text{L}$ )	Volume of Monomer ( $\mu\text{L}$ )	Total volume ( $\mu\text{L}$ )
1.	0 : 1	0	100	100
2.	1 : 9	10	90	100
3.	1 : 2.34	30	70	100
4.	1 : 1	50	50	100
5.	1 : 0.43	70	30	100
6.	1 : 0	100	0	100

**3.4.2.7. SAXS study:** SAXS experiments were carried out on SAXSess mc2 instrument (Anton-Paar) with line-collimation system using a Cu  $K\alpha$  source with wavelength of 1.54 Å. Perkin elmer cyclone image plate recorder was used to record the data. SAXSQuant 2D software was used to reduce the two dimensional data to one dimensional, Intensity (I) vs scattering vector (q) plot.

Small angle X-ray scattering (SAXS) profiles obtained from were fitted with a model for noninteracting long cylinders with a cylindrical form factor with a gaussian distribution of core radius. The fitting was carried out using SASfit software. Good fits were obtained for the single fiber and helical bundle SAXS data with the cylindrical model fit having core and shell radius of 2.1 ( $\pm 0.2$ ) nm and 2.6 ( $\pm 0.2$ ) nm respectively.

For the helical bundle the cyliders showed a characteristic length scale of ~40 nm. The length scale obtained for the helical bundle data matches reasonably well with the pitch of the twisted bundle as obtained from AFM data.

The intensity formula used to describe the fit for the SAXS data of the aggregates was

$$I = \int K_{Cyl}(Q, \eta_{core} - \eta_{shell}, R, L, x) + K_{Cyl}(Q, \eta_{shell} - \eta_{solv}, R + \Delta R, L, x)^2 dx \quad (1)$$

where,

$$K_{cyl}(Q, \Delta\eta, R, L, x) = 2\pi R^2 L \Delta\eta \left( \frac{J_1(QR\sqrt{1-x^2}) \sin(QLx/2)}{(QR\sqrt{1-x^2}) QLx/2} \right)$$

The calculated intensity of model (1) was fitted to the experimental data by adjusting the parameters  $R$ ,  $L$ ,  $\Delta R$  and the scattering contrasts.

### 3.5. References

- [1] T. F. A. De Greef, M. M. J. Smulders, M. Wolffs, A. P. H. J. Schenning, R. P. Sijbesma, E. W. Meijer, *Chem. Rev.* **2009**, *109*, 5687.
- [2] G. M. Whitesides, B. Grzybowski, *Science* **2002**, *295*, 2418.
- [3] J. -M Lehn, *Angew. Chemie Int. Ed. English* **1990**, *29*, 1304.
- [4] S. A. Schmid, R. Abbel, A. P. H. Schenning, E. W. Meijer, R. P. Sijbesma, L. M. Herz, *ACS Publ.* **2009**, *131*, 17696.
- [5] T. Gädt, N. S. Jeong, G. Cambridge, M. A. Winnik, I. Manners, *Nat. Mater.* **2009**, *8*, 144.
- [6] Z. M. Hudson, C. E. Boott, M. E. Robinson, P. A. Rupar, M. A. Winnik, I. Manners, *Nat. Chem.* **2014**, *6*, 893.
- [7] E. Mattia, S. Otto, *Nat. Nanotechnol.* **2015**, *10*, 111.
- [8] P. A. Korevaar, C. J. Newcomb, E. W. Meijer, S. I. Stupp, *J. Am. Chem. Soc.* **2014**, *136*, 8540.
- [9] P. A. Korevaar, S. J. George, A. J. Markvoort, M. M. J. Smulders, P. A. J. Hilbers, A. P. H. J. Schenning, T. F. A. De Greef, E. W. Meijer, *Nature* **2012**, *481*, 492.
- [10] A. Sorrenti, J. Leira-Iglesias, A. J. Markvoort, T. F. A. De Greef, T. M. Hermans, *Chem. Soc. Rev.* **2017**, *46*, 5476.
- [11] S. Ogi, K. Sugiyasu, S. Manna, S. Samitsu, M. Takeuchi, *Nat. Chem.* **2014**, *6*, 188.
- [12] B. Kemper, L. Zengerling, D. Spitzer, R. Otter, T. Bauer, P. Besenius, *J. Am. Chem. Soc.* **2018**, *140*, 534.
- [13] A. Mishra, D. B. Korlepara, M. Kumar, A. Jain, N. Jonnalagadda, K. K. Bejagam, S. Balasubramanian, S. J. George, *Nat. Commun.* **2018**, *9*, 1.
- [14] J. S. Valera, R. Gómez, L. Sánchez, *Small* **2018**, *14*, 1702437.
- [15] L. H. Beun, X. J. Beaudoux, J. M. Kleijn, F. A. De Wolf, M. A. Cohen Stuart, *ACS Nano* **2012**, *6*, 133.
- [16] K. Matyjaszewski, *Macromolecules* **2012**, *45*, 4015.
- [17] T. Fukui, S. Kawai, S. Fujinuma, Y. Matsushita, T. Yasuda, T. Sakurai, S. Seki, M. Takeuchi, K. Sugiyasu, *Nat. Chem.* **2017**, *9*, 493.
- [18] S. Ogi, V. Stepanenko, K. Sugiyasu, M. Takeuchi, F. Würthner, *J. Am. Chem. Soc.* **2015**, *137*, 3300.
- [19] G. Ghosh, S. Ghosh, *Chem. Commun.* **2018**, *54*, 5720.
- [20] J. Kang, D. Miyajima, Y. Itoh, T. Mori, H. Tanaka, M. Yamauchi, Y. Inoue, S. Harada, T. Aida, *J. Am. Chem. Soc.* **2014**, *136*, 10640.
- [21] J. Kang, D. Miyajima, T. Mori, Y. Inoue, Y. Itoh, T. Aida, *Science* **2015**, *347*, 646.
- [22] A. Pal, M. Malakoutikhah, G. Leonetti, M. Tezcan, M. Colomb-Delsuc, V. D. Nguyen, J. Van Der Gucht, S. Otto, *Angew. Chemie. Int. Ed.* **2015**, *54*, 7852.
- [23] F. Chiti, C. M. Dobson, *Annu. Rev. Biochem.* **2006**, *75*, 333.

- [24] I. W. Hamley, *Chem. Rev.* **2012**, *112*, 5147.
- [25] I. V. Baskakov, G. Legname, M. A. Baldwin, S. B. Prusiner, F. E. Cohen, *J. Biol. Chem.* **2002**, *277*, 21140.
- [26] P. N. Cheng, C. Liu, M. Zhao, D. Eisenberg, J. S. Nowick, *Nat. Chem.* **2012**, *4*, 927.
- [27] E. T. Pashuck, S. I. Stupp, *J. Am. Chem. Soc.* **2010**, *132*, 8819.
- [28] V. D. Nguyen, A. Pal, F. Snijkers, M. Colomb-Delsuc, G. Leonetti, S. Otto, J. Van Der Gucht, *Soft Matter* **2016**, *12*, 432.
- [29] Y. S. Dagdas, A. Tombuloglu, A. B. Tekinay, A. Dana, M. O. Guler, *Soft Matter* **2011**, *7*, 3524.
- [30] R. S. Jacob, D. Ghosh, P. K. Singh, S. K. Basu, N. N. Jha, S. Das, P. K. Sukul, S. Patil, S. Sathaye, A. Kumar, A. Chowdhury, S. Malik, S. Sen, S. K. Maji, *Biomaterials* **2015**, *54*, 97.
- [31] I. K. Piechocka, R. G. Bacabac, M. Potters, F. C. Mackintosh, G. H. Koenderink, *Biophys. J.* **2010**, *98*, 2281.
- [32] P. H. J. Kouwer, M. Koepf, V. A. A. Le Sage, M. Jaspers, A. M. van Buul, Z. H. Eksteen-Akeroyd, T. Woltinge, E. Schwartz, H. J. Kitto, R. Hoogenboom, S. J. Picken, R. J. M. Nolte, E. Mendes, A. E. Rowan, *Nature* **2013**, *493*, 651.

## Chapter 4

# Modulation of catalytic activities mediated by pathway driven nanostructures

*Enzymes are the most efficient natural catalysts that possess an impressive range of catalytic activities. They have evolved over the billions of years to possess an advanced unimaginable structural and functional complexity. Its complex folded structure finds a narrow stability that generates a hindrance to find their use for various applications. In this regard, peptides serve as a mimic to extant evolved enzyme through their diverse and complex hierarchical morphological transformations. Thus, a rationale design of short peptides 1-3 with temperature, additive and light acting as various stimuli alter their self-assembly patterns to result 1D and 2D morphologies. Further, these morphological variations were employed to investigate the non-covalent catalytic ability in a bid to mimic the complex hydrolase enzyme. The kinetic parameters of rate of hydrolysis of p-NPA to NP a standard model reaction were obtained when slopes of the reaction kinetics were fitted in Michaelis Menten's equation. Interestingly, we observed that the different morphologies have shown different binding capability for the substrate p-NPA which eventually resulted in altered catalytic efficiency ( $k_{cat}/K_m$ ).*

### 4.1. Introduction

Complex structured enzymes have evolved over the journey of life on earth and pay an impressive range of responsibilities in living systems, ranging from efficient and effective catalysis to specific molecular recognition. Nature's complex enzymes catalysis are a source of inspiration to the scientists to design the complex evolved proteins to target various reactions. Moreover, developing such complex artificial molecules in aqueous medium is still challenging. In this context, short self-assembled peptide nanostructures based enzyme mimics exhibits interesting approach to design *de novo* enzymes based on the active site substructures. Nature has selected specific sequence of the amino acids from a pool of library of the sequences for each particular reaction. It is plausible to mimic the complex 3D

structure of the enzyme by self-assembly of the specific amino acids present at the active site of the enzyme. Self-assembly is responsible for the formation hierarchical organized structures from small peptide molecules during the evolution of protein.<sup>[1,2]</sup> The interplay between the non-covalent interactions such as H-bonding,  $\pi$ - $\pi$  interactions, electrostatic, hydrogen bonding and van der Waals forces allows peptides to form different functional aggregations.<sup>[3,4]</sup> The amphiphilic nature of the self-assembled nanostructures provide binding pockets which facilitates the binding of the incoming substrate. For example, the amyloid architecture formed by short peptides provides a scaffold for enzyme-like catalysts, including catalyzing electrochemical reactions,<sup>[8]</sup> promoting specific enantioselective chemical reactions,<sup>[9]</sup> or enhancing ester hydrolysis.<sup>[10]</sup> In this context, Rein *et al.* have successfully shown the implication of short peptides to design a minimalistic biocatalyst.<sup>[11]</sup> Beate Koksche *et al.* have demonstrated the substrate specificity of an actively assembling amyloid catalyst.<sup>[12]</sup> The importance of the number of histidine residues in the peptide sequence for the ester hydrolysis was demonstrated by van Hest *et al.*<sup>[13]</sup> In this regard, Zhimin He *et al.* and Mustafa O. Guler *et al.* have described the enhance activity of peptide based artificial hydrolase with catalytic Ser/His/Asp triad and molecular imprinting.<sup>[14,15]</sup> Self-assembled nanostructures and their ionic interactions with metal ion play a crucial role in enhancing the catalytic activity. Thus, the self-assembled nanofibrous morphology over the monomer was successfully exploited by Samuel I. Stupp *et al.* for ester hydrolysis.<sup>[14]</sup> David G. Lynn *et al.* have used catalytic diversity in peptide self-assemblies using different peptides for modulating the kinetics of catalysis where assembly/disassembly of the nanostructures have been exploited as stimuli trigger to control the catalysis rate.<sup>[16]</sup> Kazuaki Kudo and coworker have developed the selective peptide catalysts where they have used secondary structural frameworks for the reaction catalysis.<sup>[17]</sup> L. C. Serpell *et al.* have recently shown the various amyloid architectures which provide a scaffold for enzyme catalysis.<sup>[18]</sup> The hydrolytic activity using various active peptide sequences into a completely *de novo* protein framework are successfully demonstrated by Woolfson *et al.* suggesting the role of cysteine-histidine-glutamic acid triads on each helix to hydrolyze *p*-nitrophenyl acetate with catalytic efficiencies that match the most-efficient redesigned hydrolases based



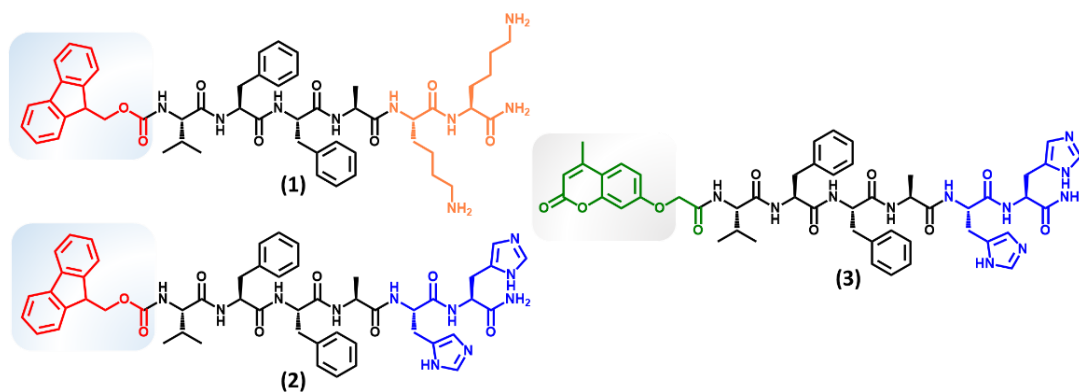
on natural protein scaffolds.<sup>[19,20]</sup> Recently, the ability of a single amino acid phenylalanine molecules coordinate with zinc ions to self-assemble to form a robust, layered, supramolecular amyloid-like ordered architecture have been shown which exhibit remarkable carbonic anhydrase-like catalytic activity.<sup>[21]</sup> Interestingly, cross- $\beta$  amyloid nanotubes with surface exposed histidine binds with heme and show facile cascade reactions to mimic dual roles of hydrolase and peroxidases, two of the most important enzymes.<sup>[22,23]</sup>

Thus, enzymatic activity is critical for various applications, however the complex extant structures of the enzymes and their narrow stability provide a hindrance in their use. It is always essential to design a robust system which can remain stable and can be employed for various applications. However, the role of inter-convertible nanostructures from the same functional moieties towards catalysis has not yet been explored, that is an important aspect in the context of enzyme-apoenzyme in presence of co-factor or external stimuli. In chapter 3, pathway dictated self-assembly has been shown using amyloid short peptides with two lysine units at C-terminal end which results in the formation of various nanostructures.<sup>[24,25]</sup> In this study, lysines were replaced with histidine at C-terminal of the amyloid short peptide sequence to investigate and access pathway dependent self-assembled nanostructures from 1D nanofibers to 2D nanosheets which was further exploited for mimicking the catalytic activity of the hydrolase enzymes.

## 4.2. Results and Discussion

### 4.2.1. Design of Peptide Amphiphiles:

Peptide amphiphiles **2** and **3** were designed by taking the inspiration from peptide **1** as discussed in chapter 3, by tethering two histidine units replacing lysine units at C-terminal and a hydrophobic aromatic fluorenylmethyloxycarbonyl (Fmoc-) and 4-methyl coumarin (photodimerizable moiety) at N-terminal to the hydrophobic A $\beta$  nucleating core VFFA, respectively (Scheme 4.1). The aromatic moieties at N-terminal along with peptide unit provide  $\pi$ - $\pi$  stacking, van der Waal's interactions and two histidines units at C-terminal imparts solubility that pave away the self-assembly of **2** and **3** in aqueous medium.



**Scheme 4.1.** Molecular structure of the peptide amphiphiles **1**, **2**, and **3**.

## 4.2.2. Self-assembly:

**4.2.2.1. Microscopic study:** Peptide **2** and **3** were dissolved in hexafluoroisopropanol (HFIP) that renders peptide amphiphiles in their monomerically dissolved state by diminishing the interactions responsible for self-assembly. Dilution of monomerically dissolved peptide **2** and **3** in aqueous medium (10 v/v% HFIP in 10 mM HEPES buffer, pH 7.4) led to the formation of metastable nanoparticles of 20-35 nm (Figure 4.1A) and of 20-40 nm (Figure 4.1B) at 10 °C, respectively.

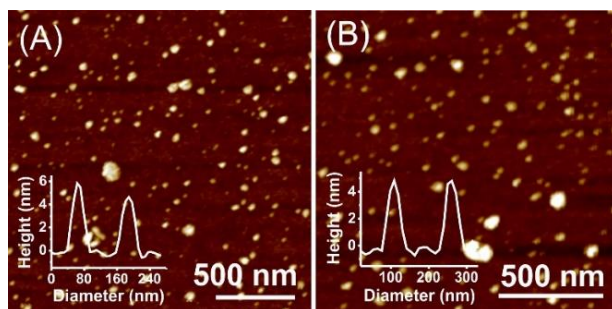


**Figure 4.1.** AFM images with height profile inset, recorded after incubating the diluted HFIP stock of peptides **2** and **3** in aqueous solution with a final concentration 250  $\mu\text{M}$ . This results in the formation of metastable nanoparticles of (A)  $2_{\text{NP}}$  and (B)  $3_{\text{NP}}$  at 10 °C.

The metastable peptide nanoparticles were stable for ~15-20 minutes at 10 °C. However, upon changing the solvent compositions metastable nanoparticles dwells in such nanostructures longer time before converting to higher order nanostructures. For peptide **2**-

**3**, 25 v/v% of HFIP in water arrests self-assembly in metastable nanoparticles for 4 h at 10 °C (Figure 4.2). On increasing the temperature to 20 °C, the diluted solution of **2**<sub>NP</sub> and **3**<sub>NP</sub>,

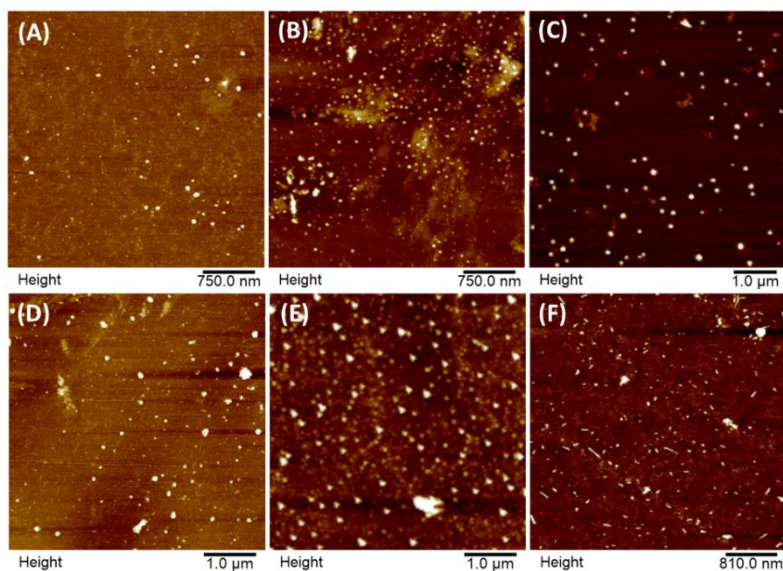


**Figure 4.2.** AFM images show the arrested metastable nanoparticles for peptide **2** (top row) (A), (B), and (C) and peptide **3** (bottom row) (D), (E), and (F) at 10 °C after 30 min, 2 h, and 4 h.

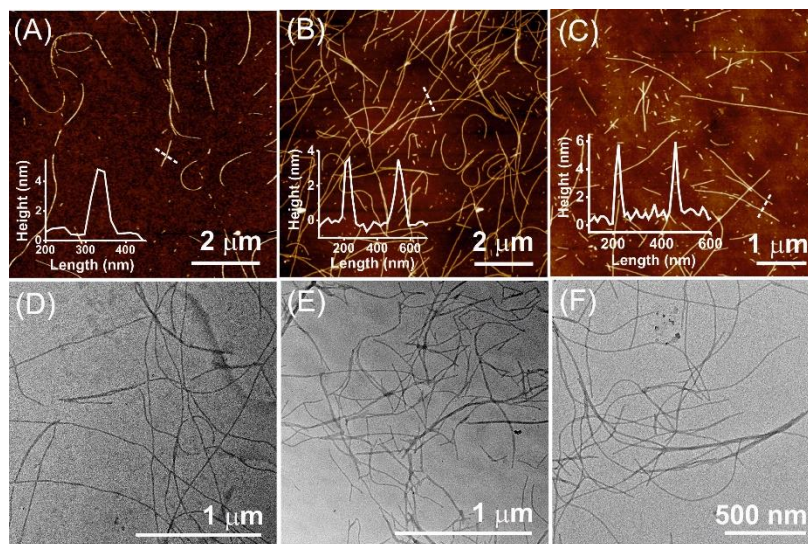


**Figure 4.3.** AFM and TEM images recorded of **1**, **2** and **3** incubated at 25 °C. AFM images with height profile inset shows (A) **1**<sub>NP</sub> with height 4-5 nm after 30 min, (B) **2**<sub>NP</sub> with height 3-4 nm after 30 min, (C) **3**<sub>NP</sub> with height 5-6 nm after 10 min. TEM images show (D) **1**<sub>NP</sub> with a diameter of ~8 nm (E) **2**<sub>NP</sub> with a diameter of 7-8 nm and (F) **3**<sub>NP</sub> with a diameter of 6-7 nm.

metastable nanoparticles eventually transform to kinetically stable nanofibers  $2_{NF}$  with height  $\sim 3$ -4 nm and diameter  $\sim 7$ -8 nm (Figure 4.3A,C) and  $3_{NF}$  with height  $\sim 4$ -5 nm and diameter of  $\sim 6$ -7 nm (Figure 4.3B, D) in  $\sim 30$  min as demonstrated by AFM and TEM images.

Interestingly, on increasing the temperature of  $2_{NF}$  solution to  $85^\circ\text{C}$  and cooling back to  $25^\circ\text{C}$  results in the formation of thermodynamically stable twisted bundle ( $2_{TB}$ ), (height 8-10 nm at the inter-twinned position with a pitch value of  $\sim 56$  nm (Figure 4.4A-C). Upon repeating the heating-cooling cycle for  $2_{TB}$  solution, no change in the formed twisted bundle morphology was observed. Thus, peptide **2** with double mutation of lysine to histidine behaves similar to **1** to forms nanofiber at  $25^\circ\text{C}$  and twisted bundle upon annealing at higher temperature (Figure 4.4).

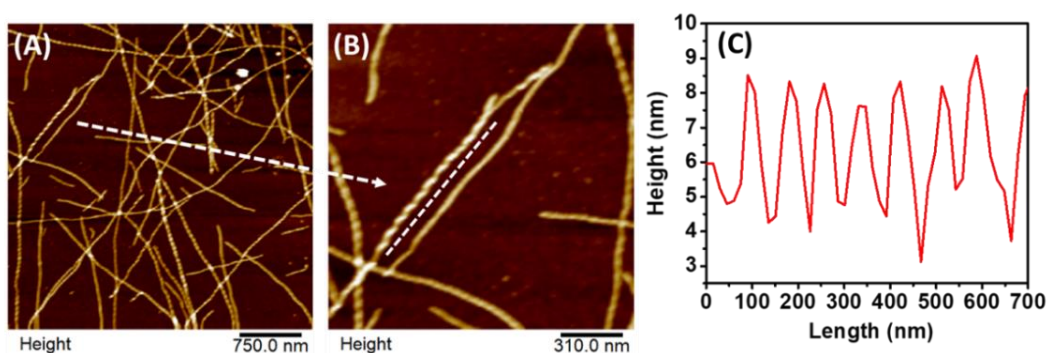


**Figure 4.4.** AFM height image showing (A) helical twisted bundle of peptide **2** ( $2_{TB}$ ) upon heating  $2_{NF}$  solution to  $85^\circ\text{C}$  followed by cooling to  $25^\circ\text{C}$ , (B) Magnified image shows the intertwining of two nanofibers, and (C) change in the height profile along the twisted bundle trajectory.

**4.2.2.2. Photo-dimerization Studies:** The addition of equimolar concentration of  $\gamma$ -cyclodextrin ( $\gamma$ -CD) solution to the metastable  $3_{NP}$ , and subsequent irradiation with UV light

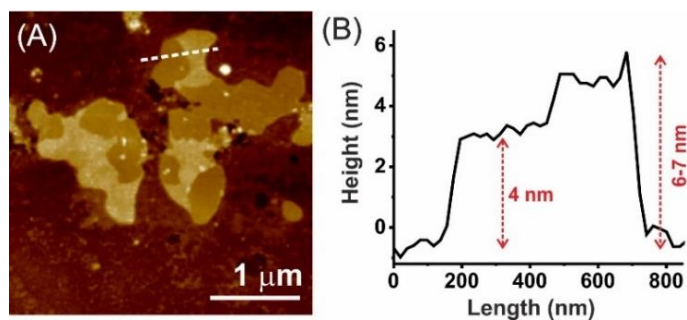
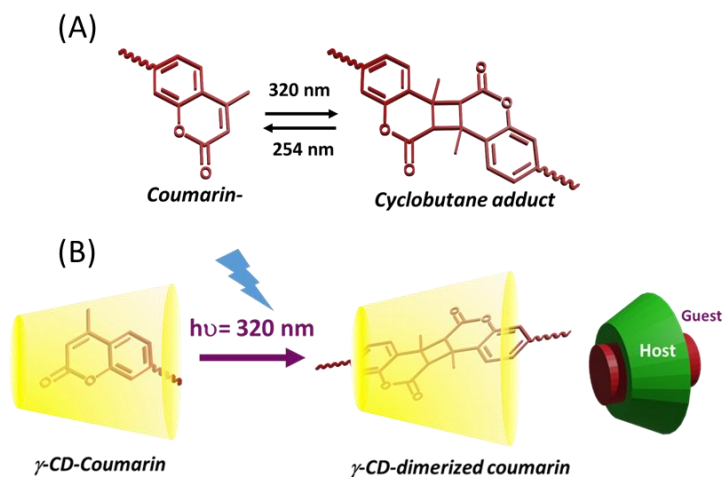


**Figure 4.5.** AFM image showing the formation of (A) 2D nanosheets ( $(di-3_C-\gamma-CD)_{NS}$ ) (B) height of 4-6 nm.

at 320 nm transforms the  $3_{NF}$  to 2-dimensional free standing nanosheets ( $(di-3_{C-\gamma-CD})_{NS}$ ) with height 4-6 nm (Figure 4.5). This morphological change was attributed owing to the formation host-guest complex between the additive  $\gamma$ -CD (host molecule) and 4-methyl coumarin moiety of  $3$  (guest molecule) and the photo-dimerization of 4-methyl coumarin unit on irradiation to form 2+2 cycloadduct (Scheme 4.2).



**Scheme 4.2.** Scheme illustrating the formation of (A) [2+2] cycloadduct from 4-methylcoumarin moiety in presence of UV light of 320 nm, (B) Host-guest complexation between  $\gamma$ -Cyclodextrin (host) and coumarin (guest) molecules followed by cycloadduct formation on irradiation.

To evaluate the photodimerization ability of 4-methyl coumarin moiety, UV spectra were recorded at various time intervals for the irradiated solutions of  $3_{NF}$  and  $(3_{C-\gamma-CD})$

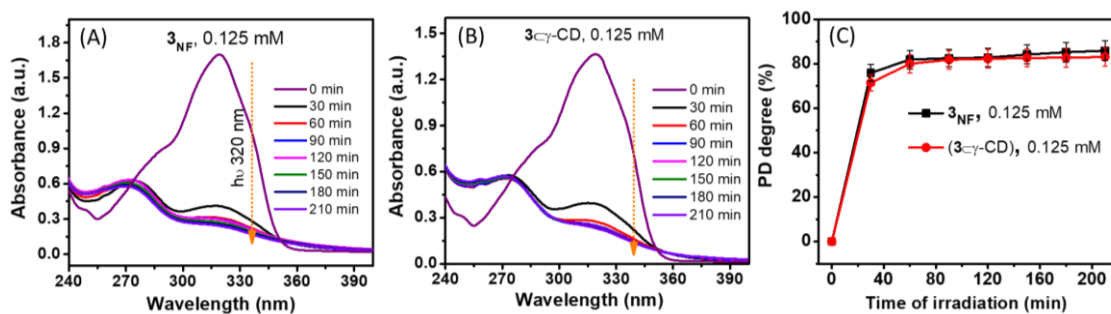


**Figure 4.6.** UV spectra show a decrease in the absorbance value upon irradiating the solutions of (A)  $3_{NF}$  (0.125 mM) (B)  $3_{C-\gamma-CD}$  using 320 nm of light (32 watt) at various time intervals. (C) Photodimerization degree was calculated to be  $\sim 84\%$  and  $\sim 83\%$  for  $3_{NF}$  and  $3_{C-\gamma-CD}$  solutions.



solutions at 320 nm. A gradual decrease in the characteristic peak was observed with the course of irradiation time at 320 nm which validated the photodimerization of the 4-methylcoumarin moiety (Figure 4.6A-B). The photodimerization degree for **3**<sub>NF</sub> and (**3**⊂ $\gamma$ -CD) was calculated to be 84% and 83% respectively (Figure 4.6C).

**4.2.2.3. Monitoring Host-Guest complexation by <sup>1</sup>H NMR Spectroscopy:** The host-guest interaction between **3** (guest) and  $\gamma$ -CD (host) to form **3**⊂ $\gamma$ -CD complex was monitored by <sup>1</sup>H NMR in D<sub>2</sub>O.

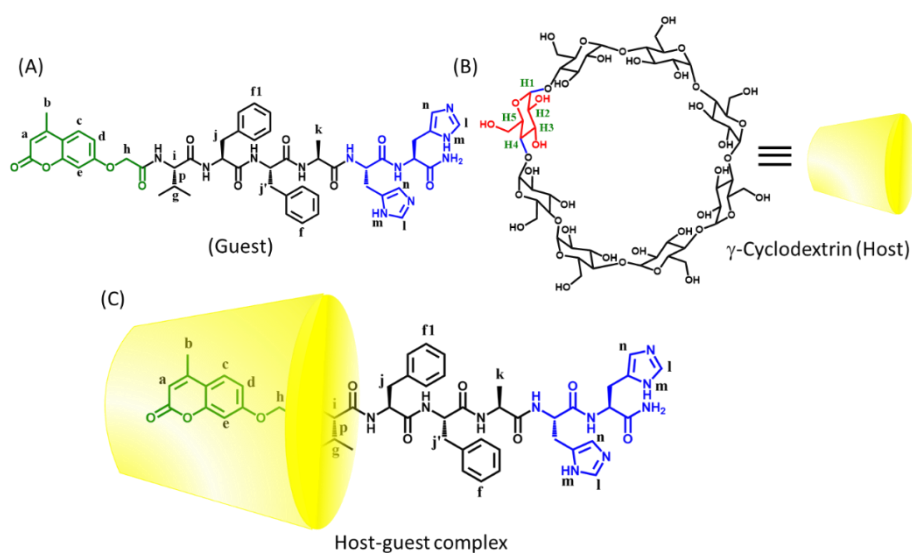


**Figure 4.7.** (A) Chemical structure of **3** (guest) with labelled protons, (B)  $\gamma$ -cyclodextrin ( $\gamma$ -CD), and (C) Inclusion complex as a result of host-guest interaction.

The peptide **3** guest was mixed with  $\gamma$ -CD host varying in host: guest ratios from 0:10, 1:9, 3:7, 5:5, 7:3, 9:1, 10:0 keeping total concentration as 10 mM. As the host concentration increases, there is an upfield shift in the coumarin protons *a*, *c*, *d*, *e* and *b* due to shielding effect of hydrophobic inner cavity of  $\gamma$ -CD on interaction with coumarin moiety in **3**⊂ $\gamma$ -CD complex (Figure 4.8). Further, the increase in splitting distance of *g* proton corresponding valine dimethyl protons (*g*) (Figure 4.9A) indicates that they are outside the cyclodextrin environment on formation of the inclusion complex (Figure 4.7C).

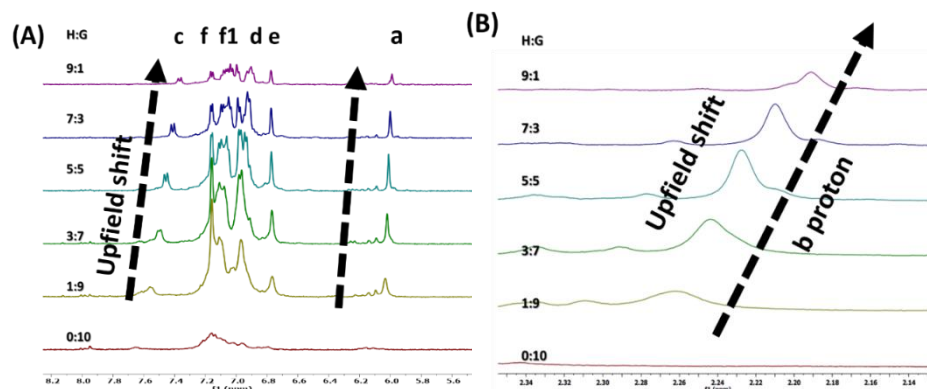


**Figure 4.8.** Partial  $^1\text{H}$  NMR spectra of **3** (guest) titrated with  $\gamma$ -CD (host) at different ratios. The total concentration was kept at 10 mM. The upfield shifts of (A) *a*, *c* protons and (B) methyl *b* protons of the 4-methylcoumarin moiety in **3** with increasing host was noted.

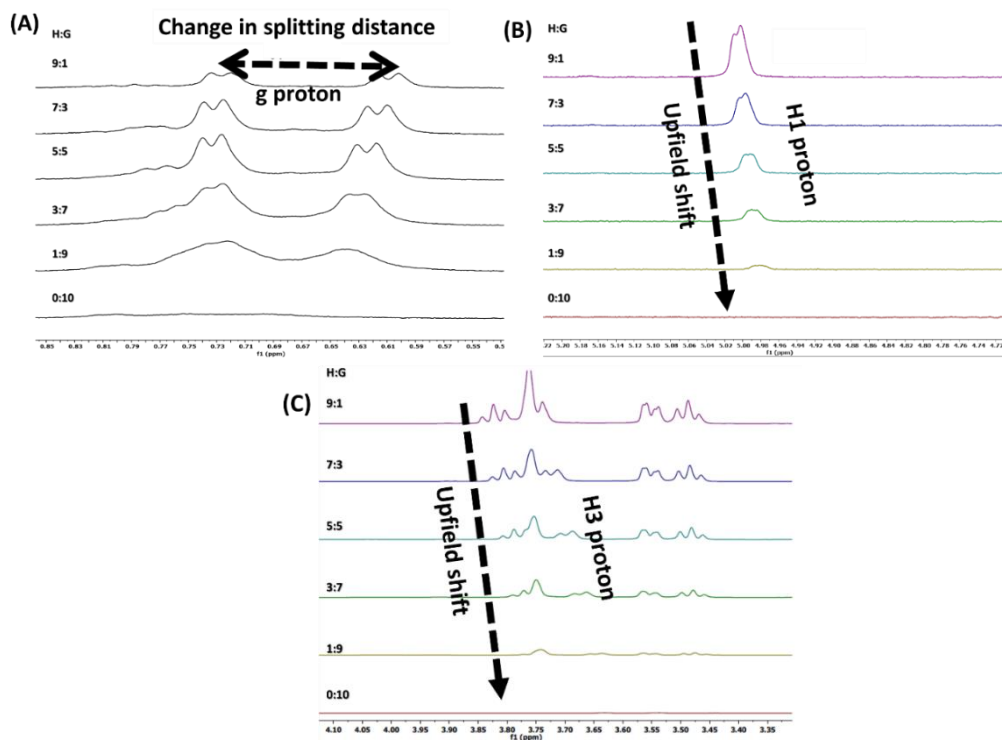


**Figure 4.9.** Partial  $^1\text{H}$  NMR spectra of  $\gamma$ -CD titrated with **3** at different ratios. The total concentration was kept at 10 mM. (A) The separation among the doublet for  $\text{H}_g$  protons of valine in **3** with increasing amount of host was noted and can be ascribed to partial inclusion of methyl groups in the cavity. (B)  $\text{H}_1$  and (C)  $\text{H}_3$  protons of the  $\gamma$ -CD (H) moiety showed upfield shift with increasing amount of guest.

Moreover, the  $\gamma$ -cyclodextrin protons H<sub>1</sub> and H<sub>3</sub> also showed upfield shift with increasing amount of guest molecule which further proved the inclusion of coumarin moiety into the host cavity. Job's plot analysis of the change in chemical shift ( $\Delta\delta$ ) corresponding to the upfield shift of coumarin protons, *a* and *b* as well as cyclodextrin protons, H<sub>1</sub> and H<sub>3</sub> with increasing molar ratio of guest and host respectively showed maximum change at 0.5 molar ratio indicating binding stoichiometry as 1:1 (Figure 4.10A & B). The binding constant or association constant ( $K_a$ ) between host ( $\gamma$ -CD) and guest molecule (**3**) was calculated using UV-vis spectroscopy. UV-vis spectra were recorded at a fixed concentration of **3** (0.25 mM) against a varied concentration of  $\gamma$ -CD. An increased in the absorbance value at 320 nm was observed with the addition of  $\gamma$ -CD solution and absorbance was saturated

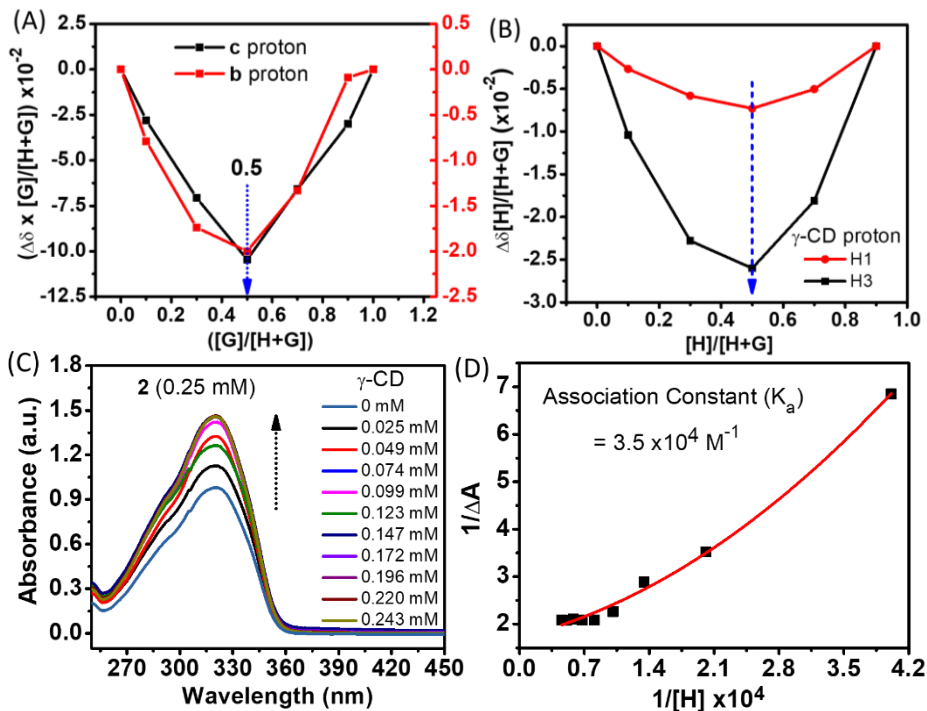


**Figure 4.10.** Job's plot obtained by titrating **3** (G) with  $\gamma$ -CD (H) at different ratio in D<sub>2</sub>O at 25 °C. The changes of chemical shifts of (A) H<sub>b</sub> and H<sub>c</sub> protons of 4-methylcoumarin moiety (B) H<sub>1</sub> and H<sub>3</sub> ring protons of  $\gamma$ -CD are plotted with the mole fraction of **3** and  $\gamma$ -CD (C) UV-vis absorbance spectra were recorded at a fixed guest (**3**) concentration (0.25 mM) against a varied concentration of  $\gamma$ -CD. (D) Association constant was calculated to be  $3.5 \times 10^4 \text{ M}^{-1}$  from a plot between change in absorbance ( $1/\Delta A$ ) against the varied concentration of  $\gamma$ -CD ( $1/[H]$ ).



after an equimolar concentration of 0.125 mM was achieved for both **3** and  $\gamma$ -CD in the solution. Binding constant or association constant ( $K_a$ ) was calculated to be  $3.5 \times 10^4 \text{ M}^{-1}$  from a plot between inverse of change in absorbance ( $1/\Delta A$ ) against inverse in the concentration of  $\gamma$ -CD ( $1/[H]$ ) (Figure 4.10C-D).

**4.2.2.4. UV Spectroscopy:** UV spectra for different morphological states for peptide **2** and **3** were recorded at a concentration of 0.1 mM at 25 °C. Spectra showed a deviation in the

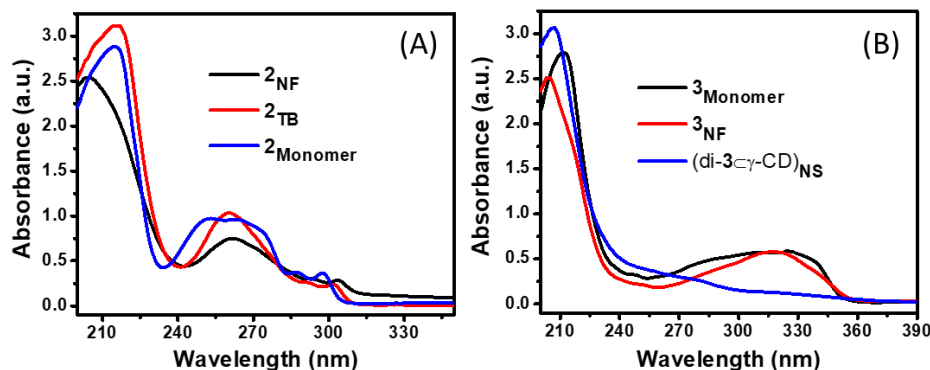


**Figure 4.11.** UV spectra for different nanostructures of peptide **2** and **3** at 0.1 mM, 25 °C. (A) Peptide **2** shows a red-shifted shoulder peak for **2<sub>NF</sub>**, and **2<sub>TB</sub>** relative to **2<sub>Monomer</sub>**. (B) Peptide **3** shows an almost loss of the peak at 320 nm of the 4-methylcoumarin for the nanosheet of (di-**3**- $\gamma$ -CD)<sub>NS</sub> compared to **3<sub>NF</sub>**.

wavelength of the peaks upon self-assembly. While **2<sub>Monomer</sub>** shows a shoulder peak at 297 nm, the self-assembled fibers, **2<sub>NF</sub>** and twisted bundles, **2<sub>TB</sub>** show red shifted peak at 303 nm and at 301 nm. In case of peptide **3**, absorbance value gets decreased for nanosheet (di-**3**- $\gamma$ -CD)<sub>NS</sub> in comparison to the peptide **3<sub>Monomer</sub>** and **3<sub>NF</sub>** (Figure 4.11).

**4.2.2.5. CD Spectroscopy:** The CD Spectra were recorded to investigate the self-assembly pattern for wavelength range of 200 nm to 325 nm with a scan speed of  $100 \text{ nm min}^{-1}$  at 25 °C. For peptide **2**, the CD spectra showed clear difference for **2<sub>Monomer</sub>**, **2<sub>NF</sub>**, and **2<sub>TB</sub>**. While **2<sub>Monomer</sub>** show random coil signature, **2<sub>NF</sub>** shows  $\beta$ -sheet signature with an absorbance minima at 212 nm. **2<sub>TB</sub>** shows a bathochromic shift indicating the formation of twisted  $\beta$ -sheet secondary structure with an absorbance minima at 218 nm (Figure 4.12A). However,

the characteristic  $\beta$ -sheet signature and induced CD band of the 4-methylcoumarin of  $3_{NF}$  gradually diminishes upon host-guest complexation as in  $(3_{C\gamma-CD})_{NF-NS}$  and further irradiation  $(di-3_{C\gamma-CD})_{NS}$  (Figure 4.12B).

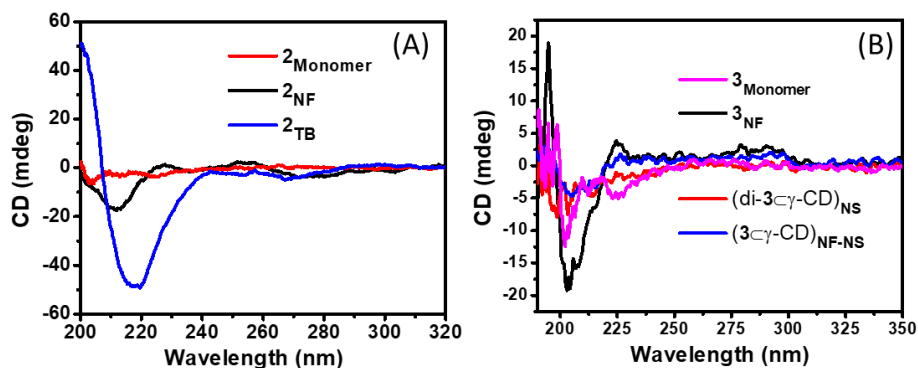
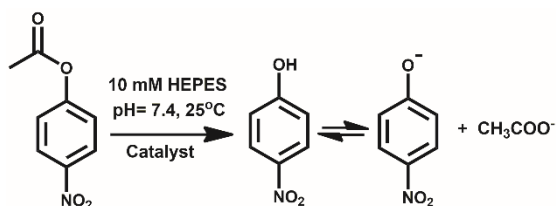


**Figure 4.12.** CD spectra for peptide **2** and **3** recorded at 0.1 mM, 25°C. (A) Peptide **2** shows a red shift in the absorbance minima for  $2_{NF}$ , and  $2_{TB}$  relative to  $2_{Monomer}$ . (B) Peptide **3** show a loss of the UV peak of the 4-methyl coumarin at 320 nm for the irradiated sample  $(di-3_{C\gamma-CD})_{NS}$  as compared to  $3_{NF}$ .

**4.2.2.6. Kinetics Study:** We explored the catalytic properties of difference peptide nanostructures of **2** and **3**. For this purpose, different morphologies from  $2_{NF}$ ,  $2_{TB}$ ,  $3_{NF}$ , and  $(di-3_{C\gamma-CD})_{NS}$  were utilized as catalysts against a model substrate reaction where *p*-NPA (substrate) gets hydrolyzed that results in the formation of yellow colored *p*-nitrophenolate



**Scheme 4.3.** A model hydrolyase reaction shows the conversion of *p*-NPA to *p*-NP in the presence of catalysts.

ion (*p*-NP). The formation of *p*-NP can be easily monitored using UV-vis absorption maxima at 400 nm as a function of time. The substrate concentrations were optimized using a fixed catalyst concentration (0.25 mM) in 10 mM HEPES buffer, pH 7.4 at 25 °C. Initially to begin with,  $2_{NF}$  solution was used as catalyst and addition of *p*-NPA solution to it, shows a linear increase of absorption intensity, and confirms the formation of *p*-NP in the reaction mixture

(Figure 4.13). To argue the role of histidine appended  $2_{\text{NF}}$  in catalyzing the reaction, a number of control experiments were performed. Thus, the substrate solution without the any peptides in HEPES buffer (10 mM, pH 7.4) and without histidinylated peptide ( $1_{\text{NF}}$  with lysine) shows no catalysis as corroborated from absorbance values showing no increase. On

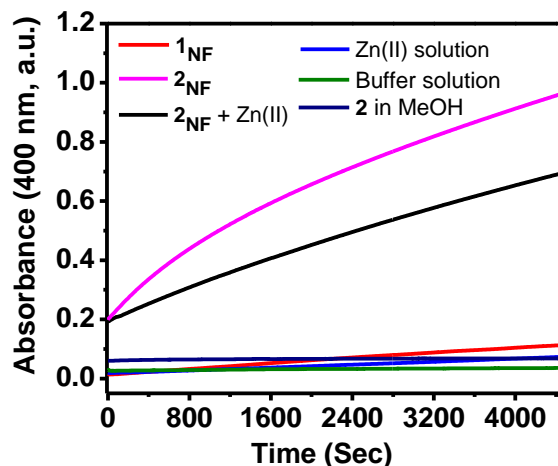


**Figure 4.13.** Timecourse UV-vis spectra were recorded in the presence of catalyst solution (0.25 mM) for the formation of *p*-NP at a fixed wavelength of 400 nm at 25 °C.  $2_{\text{NF}}$  as catalyst solution shows maximum slope with product formation. Zinc(II) coordinated to histidine units in  $2_{\text{NF}}$  showed a lower slope than native  $2_{\text{NF}}$  that is attributed to the blocked histidine sites. Addition of substrate solution in a solution of **1** in MeOH (monomeric state), 10 mM HEPES buffer, and  $1_{\text{NF}}$  where histidine units were replaced with lysine showed a constant value close to baseline with no considerable *p*-NP formation.

the other hand, peptide **2** was dissolved in methanol, the fibers get destroyed and does not exhibit *p*-NP formation indicating no catalytic cleavage of *p*-NPA. This emphasize the role of self-assembled  $2_{\text{NF}}$  with catalytic histidine residue that triggers the hydrolysis with formation of product. The importance of synergistic effect of histidine units and self-assembly in  $2_{\text{NF}}$  is evident as peptide **1** with two lysine units does not catalyze the model hydrolase reaction. Further, the catalytic efficacy of various peptide nanostructures of **2** were investigated with employing  $2_{\text{TB}}$  and  $2_{\text{NF}}$  as catalyst. The initial rate values from the absorption kinetics were calculated and were plotted against *p*-NPA concentrations that shows higher value for  $2_{\text{TB}}$  than  $2_{\text{NF}}$  (Figure 4.14A). Higher values for  $2_{\text{TB}}$  can be attributed to the two intertwined fibers that endows multiple histidine in close proximity that activates

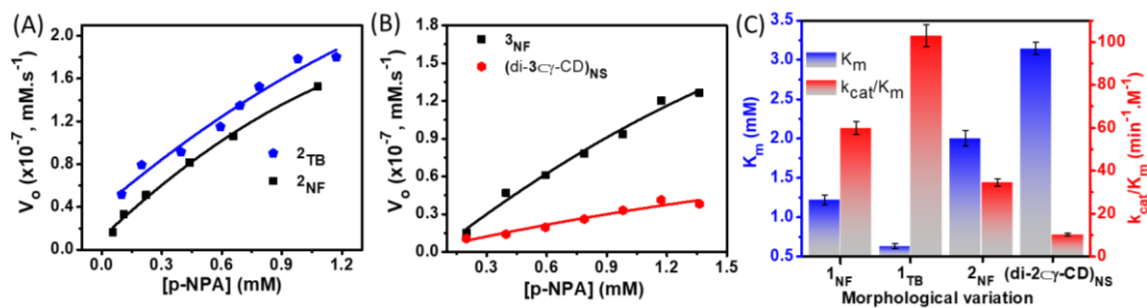


**Figure 4.14.** Comparison plots of the slope values vs respective  $[p\text{-NPA}]$  for (A)  $2_{\text{NF}}$  and  $2_{\text{TB}}$  (0.25 mM). (B)  $3_{\text{NF}}$  and  $(\text{di-}3\text{-}\gamma\text{-CD})_{\text{NS}}$  (0.25 mM). Value of the slopes with their corresponding  $[p\text{-NPA}]$  were fitted in Michaelis Menten's Equation to calculate various rate kinetics parameters. (C) Comparison of Michaelis Menten's constant ( $K_m$ ) and catalytic efficiency ( $k_{\text{cat}}/K_m$ ).

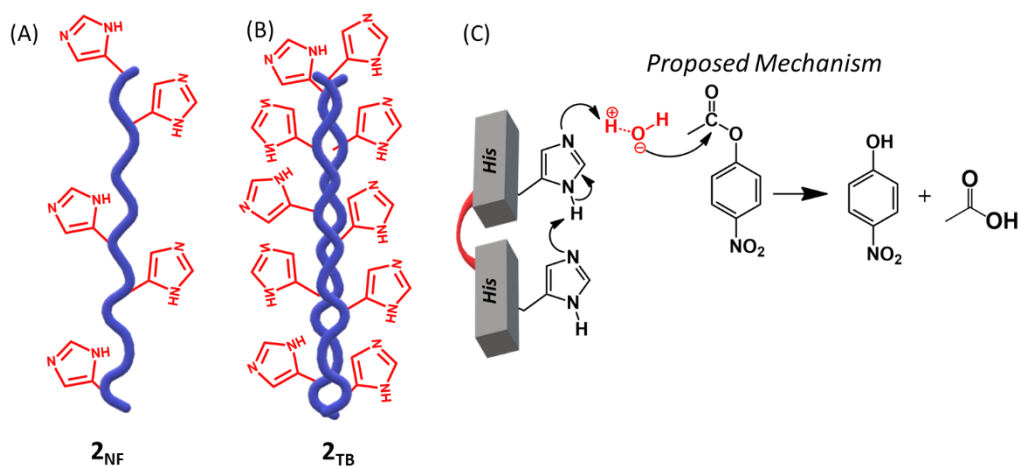
**Table 4.1.** Comparison of the kinetic parameters for different morphologies.

Morphology	Michaelis Menten's Parameters		
	$k_{\text{cat}}$ ( $\times 10^{-2}$ , $\text{min}^{-1}$ )	$K_m$ (mM)	$k_{\text{cat}}/K_m$ ( $\text{M}^{-1}\text{min}^{-1}$ )
$2_{\text{NF}}$	7.66	1.22	60.04
$2_{\text{TB}}$	6.49	0.67	102.91
$3_{\text{NF}}$	6.92	2.01	34.52
$(\text{di-}3\text{-}\gamma\text{-CD})_{\text{NS}}$	3.25	3.14	10.36

water molecules leaving hydroxyl anion free to act as nucleophile for ester hydrolysis in  $p\text{-NPA}$ . Initial rate values obtained using different morphologies with the corresponding substrate concentrations were further fitted Michaelis Menten's equation and were compared. Moreover, comparing the rate of hydrolysis reaction using 2-D nanosheets with 1-Dimensional nanofibers would be intriguing in the context of dimensions of self-assembly and accessibility of catalytic groups. When the nanosheets  $(\text{di-}3\text{-}\gamma\text{-CD})_{\text{NS}}$  solution was employed as catalyst, we found that the initial rate of product formation was much less (Figure 4.14B) than  $3_{\text{NF}}$ . Figure 4.14C and Table 4.1 shows the comparison of Michaelis Menten's constant ( $K_m$ ) along with catalytic rate ( $k_{\text{cat}}$ ) and catalytic efficiency ( $k_{\text{cat}}/K_m$ ). Lower  $K_m$  value reflects the higher affinity of the catalysts for substrate binding. The catalytic

efficiencies ( $k_{cat}/K_m$ ) were used to compare the reactivities of different catalyst on the same substrate (*p*-NPA).

To further envisage the performance of *in-situ* hydrolysis of *p*-NPA using a flow catalytic converters, flow catalysts were designed after casting the self-assembled networks of **1<sub>NF</sub>**, **1<sub>TB</sub>**, and (di-**2** $\gamma$ -CD)<sub>NS</sub> (0.5 w/v%) on 0.22  $\mu$ m nylon filter (Figure 4.15A). Further,



**Scheme 4.4.** Cartoon image with exposed imidazole residue for (A) **2<sub>NF</sub>** and (B) **2<sub>TB</sub>**. (C) A proposed mechanism for the conversion of *p*-NPA to *p*-NP.

*p*-NPA solution was passed through the each modified filter with a flow rate of 1 mL/min and absorption spectra of the filtrate were monitored after every 5 passage. The absorption intensity at 400 nm kept on increasing owing to production of *p*-NP and reached a saturation plateau with no further increment indicating the complete conversion of *p*-NPA to *p*-NP. In comparison to **2<sub>NF</sub>**, and (di-**3** $\gamma$ -CD)<sub>NS</sub>, **2<sub>TB</sub>** exhibited higher catalytic efficacy. This can be attributed to the more number of histidine units in **2<sub>TB</sub>** available to activate water molecule to leave hydroxyl free to attack substrate molecule (Scheme 4.4). For the control sample, when *p*-NPA solution was passed through the filter where self-assembled network was absent, *p*-NP formation was not observed.

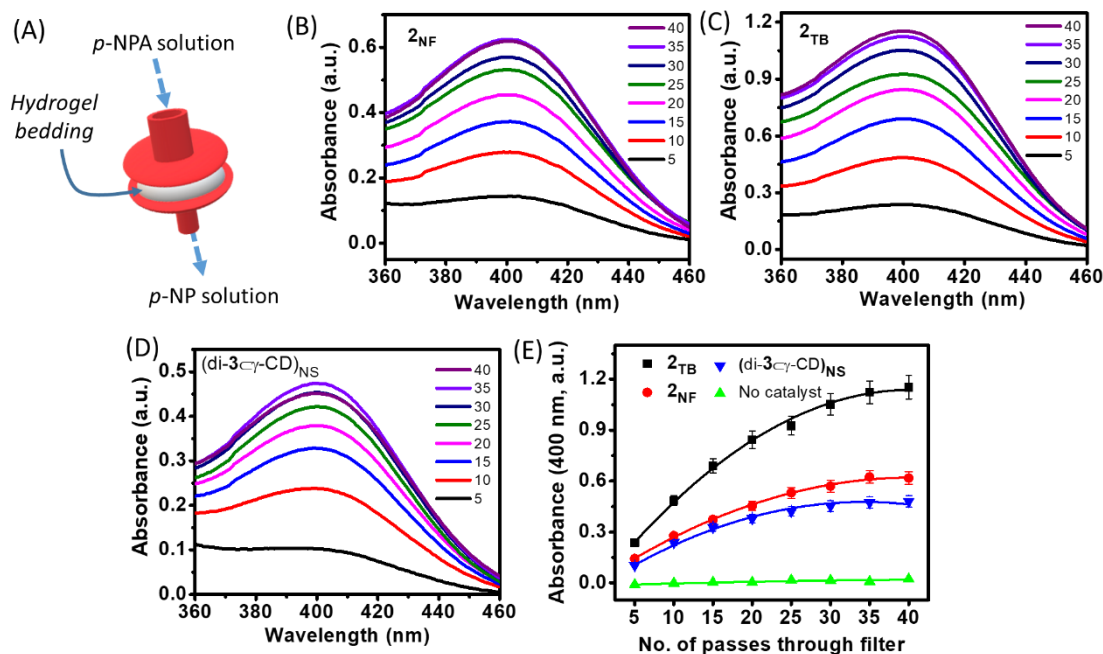
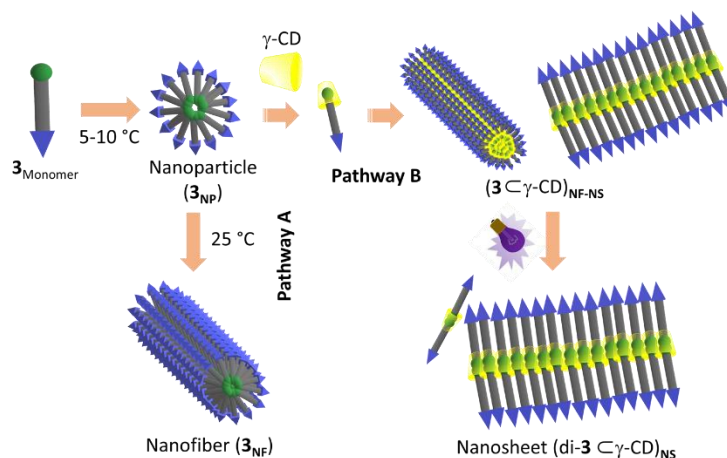


**Figure 4.15.** (A) The effect and performance of *in-situ* transformation of *p*-NPA to *p*-NP in flow condition was monitored using supramolecular network (4.14 mM) deposited in the 0.22  $\mu\text{m}$  nylon filter. UV-vis spectra showing the catalytic rate of conversion of *p*-NPA to *p*-NP at 400 nm against number of passage of the substrate solution (0.4 mM) through (B)  $2_{\text{NF}}$ , (C)  $2_{\text{TB}}$ , and (D)  $(\text{di-3}\gamma\text{-CD})_{\text{NS}}$  networks on the nylon filter.

### 4.3. Conclusions

Thus, we demonstrated pathway dependent tuning of self-assembly to furnish 1D and 2D nanostructures. The formation of metastable nanoparticles ( $2_{\text{NP}}$  and  $3_{\text{NP}}$ ) at 10  $^{\circ}\text{C}$  and on further increasing the temperature to 25  $^{\circ}\text{C}$ , metastable nanoparticles transform to kinetically stable nanofibers ( $2_{\text{NF}}$  and  $3_{\text{NF}}$ ). Further, increasing the temperature of  $2_{\text{NF}}$  solution to 85  $^{\circ}\text{C}$  and cooling back to 25  $^{\circ}\text{C}$  results in the formation of twisted bundles ( $2_{\text{TB}}$ ). On the other hand, addition of  $\gamma\text{-CD}$  solution to  $3_{\text{NP}}$  solution and subsequent irradiation at 320 nm results in the formation of 2D free standing nanosheets as shown in Scheme 4.5. The hierarchical organized supramolecular structures in creating artificial hydrolase enzyme generate catalytic centers and binding pocket that synergistically impart characteristic roles in enhancing the catalytic activities. These different nanostructures showed a variation in the

catalytic activity of hydrolyse reaction against a model substrate reaction. An altered catalytic efficiencies emphasized the route taken during self-assembly for peptide **2** and **3**



**Scheme 4.5.** Cartoon representation of peptide **3** and its pathway dependent morphological transformations.

that directly effects the exposed binding site and catalytic moieties for the incoming substrate.

## 4.4. Materials and Methods

### 4.4.1. Materials:

All Fmoc protected amino acids, activator (diisopropyl carbodiimide), piperazine, triisopropylsilane, anisole, 1,2-ethanedithiol, *p*-nitrophenol, *p*-nitrophenyl acetate and thioflavin-T were purchased from Sigma Aldrich. Oxyma, Fmoc-Rink amide MBHA Resin was purchased from Merck. HPLC grade Acetonitrile, HPLC water, ethanol and DMF were obtained from Merck. Trifluoroacetic acid was purchased from SRL.

### 4.4.2. Methods:

Solid Phase Peptide Synthesis was performed in Liberty Blue CEM, Matthews, NC, USA and the synthesized peptide was characterised using reverse phase C<sub>18</sub> column Waters HPLC coupled with Q-TOF MS detector. CD spectra were recorded using JASCO J-1500 Circular Dichroism Spectrometer, Easton, MD, USA. The wavelength range was selected

from 195 nm to 350 nm with a scan speed of 100 nm min<sup>-1</sup> using 2 mm path length CD quartz cuvette. UV spectrophotometer (Shimadzu UV-2600) was used to perform the kinetics experiments. The Samples were drop casted on silicon wafer and AFM height images were recorded using tapping mode on a Bruker Multimode 8 scanning probe microscope with silicon cantilever. TEM images were recorded using JEOL JEM 2100 TEM with a Tungsten filament at an accelerating voltage of 120 kV. The linear viscoelastic region, storage modulus, loss modulus and thixotropic studies were calculated using a Rheoplus 302 (advanced Rheometer) device using cone plate (CP25-2) geometry at measuring distance of 0.172 mm at 25 °C.

**4.4.2.1. Synthesis of peptide 1:** Microwave Automated Solid Phase Peptide Synthesizer (Liberty Blue CEM, Matthews, NC, USA) was used to synthesize peptide **1**, **2** and **3**. Fmoc-Rink Amide MBHA Resin was first swelled in dimethylformamide (DMF) for 30 minutes. All Fmoc protected amino acids were weighed as per the desired scale of the reaction followed by dissolving in required DMF solution. Deprotection of Fmoc group from the amino acid was achieved by using 20% piperazine in DMF containing 10% ethanol in the microwave reactor. Required mass of piperazine was vortexed in 10% of ethanol followed by addition of the remaining 90% of DMF for completely solubilization. Diisopropyl carbodiimide (DIC, activator) and Oxyma (activator base) in DMF, were used as activators for the coupling reaction between acid and amine to form the peptide bond. A cycle of coupling, deprotection steps was repeated to synthesize the required peptide anchored to the resin. The peptide was cleaved from the resin upon shaking with a cocktail solution, a mixture of trifluoroacetic acid (TFA)/triisopropylsilane (TIPS)/water/1, 2-ethanedithiol (EDT) (95: 2: 2: 1, v/v/v/v) for 3 h at room temperature. The resin was then filtered and the filtrate containing desired peptide and excess TFA was evaporated. The peptides were then precipitated from cold diethyl ether and dried to obtain white powder. The peptide was purified by RP-HPLC using a Waters Semi-Preparative binary HPLC system using a C<sub>18</sub>-reverse phase column with an acetonitrile-water mobile phase containing 0.1% TFA. The



purified peptide was confirmed by ESI-MS recorded with Waters HPLC Q-TOF mass instrument.

**4.4.2.2. Atomic Force Microscopy (AFM):** Sample preparation at low temperature was performed by placing silicon wafer on a cold water maintained at 10 °C. 10  $\mu\text{L}$  of 0.15 mM of the peptide solution was drop casted on silicon wafer. After 5 minutes, the silicon wafer was washed with 500  $\mu\text{L}$  water using micropipette to remove excess peptide. The silicon wafer was then left to be air dried in a desiccator. AFM height images were recorded by tapping mode on a Bruker Multimode 8 scanning probe microscope with silicon cantilever (Bruker).

**4.4.2.3. Transmission Electron Microscopy (TEM):** 6  $\mu\text{L}$  of 2  $\mu\text{M}$  aqueous peptide solution were drop-casted on a 200 mesh carbon-coated copper grid. After  $\sim$  5 min, excess solution was blotted using Whatman filter paper. 4-5  $\mu\text{L}$  of uranyl acetate solution (1.0 w/v %) was then added for negative staining and incubated for 4-5 minutes at room temperature. Solution was then wicked off by Whatman filter paper from all edges of the grid carefully. Further, grids with stained samples were dried in the desiccator under vacuum for 1 day. TEM images were recorded using JEOL JEM 2100 with a Tungsten filament at an accelerating voltage of 120 kV.

**4.4.2.4. Kinetics of *para*-nitrophenyl acetate (*p*-NPA) hydrolysis:** A stock solution of *p*-NPA (50 mM) was prepared in acetonitrile. 2  $\mu\text{L}$  of it was added to a quartz cuvette containing  $2_{\text{NF}}$  dissolution (0.25 mM, 0.5 mL) in 10 mM HEPES buffer, pH 7.4 at 25 °C. At this stage, the final concentration of *p*-NPA was 0.199 mM. The cuvette was immediately shaken and placed inside the UV-vis spectrophotometer for recording spectra. The kinetics spectra was recorded at a constant wavelength of 400 nm. A linear increase in the absorbance value shows the formation of product *p*-nitrophenol (*p*-NP) with course of time. A range of substrate aliquots 2  $\mu\text{L}$  (0.055 mM) to 12  $\mu\text{L}$  (1.080 mM) were added separately to a fresh solution of  $2_{\text{NF}}$  (0.25 mM in 10 mM HEPES buffer, pH 7.4) to record and investigate the

substrate dependence kinetics of hydrolysis with time. It was quite interesting to compare the effect of different morphologies on the hydrolysis kinetics resulting the formation of *p*-NP. Similarly, solutions of **2<sub>NF</sub>**, **2<sub>TB</sub>**, **3<sub>NF</sub>**, and (di-**3**⌊-CD)<sub>NS</sub> were used as catalyst to compare the hydrolysis rate.

**4.4.2.5. Rate of hydrolysis of *p*-NPA:** Absorbance values of initial 300 seconds were selected and plotted against time. These absorbance values were subtracted from the absorbance values of the catalyst without substrate. The resulting values of the absorbance at different intervals of time were divided with molar extinction coefficient  $12700 \text{ M}^{-1}\text{cm}^{-1}$ , slopes were calculated for each substrate (*p*-NPA) concentration in a fixed concentration of **2<sub>NF</sub>** (0.25 mM). The slope values were plotted against different substrate concentrations followed by polynomial fitting of the data points. These slope values with respective substrate concentrations were fitted in Michaelis-Menten's equation to calculate the kinetic parameters  $k_{cat}$ ,  $K_M$ , and  $k_{cat}/K_M$ .

**4.4.2.6. Kinetics study on nylon 0.22 μm filter:** 4.5 mM of stock solution of **2<sub>NF</sub>**, **2<sub>TB</sub>**, and (di-**3**⌊-CD)<sub>NS</sub> was prepared in HPLC water which was incubated for 24 h. Sodium phosphate buffer (SPB) was added to it to maintain the final concentration of **2** and **3** (4.14 mM, 0.5 w/v %, pH 7.4) with a final concentration of SPB of 10 mM. Addition of SPB to the free flowing self-assembled solution turned to a viscous solution and incubation for 6 h. A total of 400 μL of the viscous solution of different nanostructures was pushed to 0.22 μm nylon filter separately. After every 200 μL of addition of viscous solution, the syringe filter was placed undisturbed to form cast of supramolecular network. The filters with nanostructure matrix was incubated for air dry for 2 h. 200 μL of the viscous solution of peptide amphiphiles was again injected in the filter to form another layer of network followed by incubation air for 2 h for air drying. A stock of substrate solution 500 mM prepared in acetonitrile, was diluted in 10 mM HEPES buffer, pH 7.4 with a final concentration of 0.4 mM. 1.5 mL of the resultant solution was passed through modified filter having a cast of supramolecular network with a maintained flow rate of 1.0 mL/min. Filtrate

was collected and passed five times through the same filter, to get product *p*-NP in the filtrate solution. After five times passage, UV-vis absorption spectra were recorded. Further, following the same protocol, this solution was again passed 5 times through the same catalytic filter and spectra were recorded. The enhancement in the absorption value after every cycle at 400 nm confirms the transformation of *p*-NPA to *p*-NP. After 35 times of passage through the filter, the absorbance values get saturated suggesting no further formation of the product *p*-NP. The same protocol was followed using filter with a matrix of **2TB**, and (di-**3**- $\gamma$ -CD)<sub>NS</sub>. The absorption spectra were plotted and slope values were calculated against number of times the substrate solution passed through the catalytic filter.

## 4.5. References

- [1] C. P. J. Maury, *Cell. Mol. Life Sci.* **2018**, *75*, 1499.
- [2] R. V. Ulijn, A. M. Smith, *Chem. Soc. Rev.* **2008**, *37*, 664.
- [3] Y. Li, Y. Cao, *Chinese J. Polym. Sci.* **2018**, *36*, 366.
- [4] G. M. Whitesides, J. P. Mathias, C. T. Seto, *Science* **1991**, *254*, 1312.
- [5] A. Lakshmanan, S. Zhang, C. A. E. Hauser, *Trends Biotechnol.* **2012**, *30*, 155.
- [6] N. Habibi, N. Kamaly, A. Memic, H. Shafiee, *Nano Today* **2016**, *11*, 41.
- [7] O. Zozulia, M. A. Dolan, I. V. Korendovych, *Chem. Soc. Rev.* **2018**, *47*, 3621.
- [8] H.-S. Jang, J.-H. Lee, Y.-S. Park, Y.-O. Kim, J. Park, T.Y. Yang, K. Jin, J. Lee, S. Park, J. M. You, K.-W. Jeong, A. Shin, I.-S. Oh, M.-K. Kwon, Y.I. Kim, H.-H. Cho, H. N. Han, Y. Kim, Y. H. Chang, S. R. Paik, K. T. Nam, Y. S. Lee, *Nat. Commun.* **2014**, *5*, 3665.
- [9] T. O. Omosun, M. C. Hsieh, W. S. Childers, D. Das, A. K. Mehta, N. R. Anthony, T. Pan, M. A. Grover, K. M. Berland, D. G. Lynn, *Nat. Chem.* **2017**, *9*, 805.
- [10] C. Zhang, X. Xue, Q. Luo, Y. Li, K. Yang, X. Zhuang, Y. Jiang, J. Zhang, J. Liu, G. Zou, X. J. Liang, *ACS Nano* **2014**, *8*, 11715.
- [11] K. Duncan, R. U. Biocatalysis, undefined 2015, *degruyter.com* **n.d.**
- [12] J. L. Heier, D. J. Mikolajczak, C. Böttcher, B. Kocsch, *Biopolymers* **2017**, *108*, e23003.
- [13] L. Schoonen, K. S. Van Esterik, C. Zhang, R. V. Ulijn, R. J. M. Nolte, J. C. M. van Hest, *Sci. Rep.* **2017**, *7*, 1.
- [14] M. O. Guler, S. I. Stupp, *J. Am. Chem. Soc.* **2007**, *129*, 12082.
- [15] M. Wang, Y. Lv, X. Liu, W. Qi, R. Su, Z. He, *ACS Appl. Mater. Interfaces* **2016**, *8*, 14133.
- [16] M. Bélières, N. Chouini-Lalanne, C. Déjugnat, *RSC Adv.* **2015**, *5*, 35830.
- [17] K. Akagawa, K. Kudo, *Acc. Chem. Res.* **2017**, *50*, 2429.
- [18] Z. S. Al-Garawi, B. A. McIntosh, D. Neill-Hall, A. A. Hatimy, S. M. Sweet, M. C. Bagley, L. C. Serpell, *Nanoscale* **2017**, *9*, 10773.

- [19] A. J. Burton, A. R. Thomson, W. M. Dawson, R. L. Brady, D. N. Woolfson, *Nat. Chem.* **2016**, *8*, 837.
- [20] K. S. Broo, L. Brive, P. Ahlberg, L. Baltzer, *J. Am. Chem. Soc.* **1997**, *119*, 11362.
- [21] P. Makam, S. S. R. K. C. Yamijala, K. Tao, L. J. W. Shimon, D. S. Eisenberg, M. R. Sawaya, B. M. Wong, E. Gazit, *Nat. Catal.* **2019**, *2*, 977.
- [22] A. Chatterjee, S. P. Afrose, S. Ahmed, A. Venugopal, D. Das, *Chem. Commun.* **2020**, DOI 10.1039/d0cc00279h.
- [23] S. Bal, K. Das, S. Ahmed, D. Das, *Angew. Chem. Int. Ed.* **2019**, *58*, 244.
- [24] A. Singh, J. P. Joseph, D. Gupta, I. Sarkar, A. Pal, *Chem. Commun.* **2018**, *54*, 10730.
- [25] J. P. Joseph, A. Singh, D. Gupta, C. Miglani, A. Pal, *ACS Appl. Mater. Interfaces* **2019**, *11*, 28213.

## Chapter 5

# Peptide nanostructures directed bioglass composites as dynamic and self-healable bone matrix mimick

*This chapter demonstrates the pathway controlled self-assembly of peptide amphiphile **1** to furnish kinetically controlled nanofibers (**I<sub>NF</sub>**) and thermodynamically stable twisted bundles (**I<sub>TB</sub>**). These supramolecular nanostructures with different persistence lengths promote in situ mineralization to result templated bioactive glass composites, **I<sub>NF</sub>BG** and **I<sub>TB</sub>BG**-resorbable and degradable biomaterials as bone scaffolds. The structural features of the hydrogel composites were investigated extensively with microscopic characterization, EDX, Raman, XPS to conclude **I<sub>TB</sub>BG** as superior materials with a higher percentage of open network structures as obtained from ratios of non-bridging and bridging oxygen. The hydrogel composites showed excellent dynamic and self-healing behavior from rheological studies, especially the elastic moduli of **I<sub>TB</sub>BG** being almost comparable to natural bone. Upon incubation in simulated body fluid, the bioglass composites illustrated a tunable bioactive response mediated by the structural and topological control to induce the deposition of multiphasic calcium phosphate along with octacalcium phosphate and carbonate hydroxyapatite. Finally, such spatiotemporal composites facilitated stiffness-controlled osteoblast cellular interactions to support U2OS cell line in the hydrogel matrix, highlighting their efficacy as substrate for osteoblast growth.*

### 5.1 Introduction

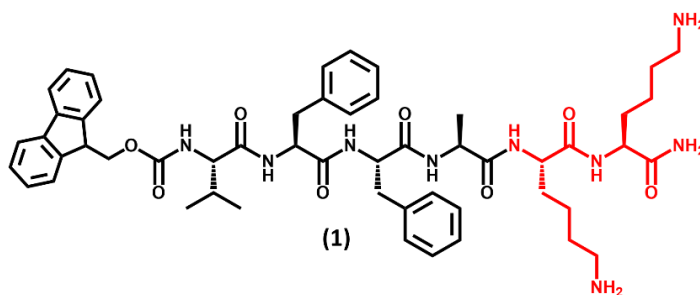
Peptide hydrogels have emerged as interesting scaffold materials for tissue engineering<sup>[1,2]</sup> and draw its advantage over native proteins owing to the ease of synthetic manipulations, resistance to denaturation and alleviation of pathogenic contamination from biological sources.<sup>[3,4]</sup> Moreover, self-assembled peptide structures as soft template for mineralization has immense scope in designing nanostructures from silica, calcium carbonate, metal nanoclusters, quantum dots and metal sulfides nanoparticles with emphasis

on their latest progresses in biomedical applications.<sup>[5-7]</sup> Interestingly, peptide amphiphile templated hydroxyapatite and calcium phosphate mineralization<sup>[8-11]</sup> have found its relevance owing to its structural analogy with collagen templated mineralization in tendon and ligaments. Peptide modified bioactive glass as a mimic to fibronectin and bone morphogenetic proteins exhibits osteogenesis of preosteoblast cells as reported by colin *et al.*<sup>[12]</sup> Pertinently, the positively charged amino acids close to the C-terminal end of the collagen molecules promotes the infiltration of the fibrils with amorphous calcium phosphate.<sup>[13]</sup> Tavafoghi *et al.* reported faster precipitation of hydroxyapatite induced by the positively charged arginine appended graphene oxide in simulated body fluids owing to the exposure of both carboxyl and amino groups on the surface which electrostatically attract both  $\text{Ca}^{2+}$  and  $\text{PO}_4^{2-}$  ions, thereby increasing local supersaturation.<sup>[14]</sup> Recently, we demonstrated pathway-driven self-assembly of peptide amphiphiles based on A $\beta$ 42 amyloid nucleating cores to design nanostructures ranging from 1D nanofibers, twisted bundles and 2D nanosheets that employs tandem interplay of noncovalent interactions such as hydrogen bonding, host-guest complexation and reversible photocyclization.<sup>[15,16]</sup> The pathway-controlled peptide nanostructures also emulate structural similarity with the cytoskeletal microfilaments and can be postulated to be utilized as mineralization template for designing bioactive glass composites to engender biomimetic deposition of calcium phosphate. Such composites for bone regeneration draws its analogy from the natural composition of bone, with collagen and biological hydroxyapatite as the main organic and inorganic constituents, respectively.<sup>[17]</sup> In this context, it is intriguing for us to explore the structure-property relation of the nanofibers and twisted helical bundle as a template for controlling osteogenesis in a bid to mimic the role of the fibrous protein and triple helical collagen protein of the bone ECM respectively. Herein, we attempt a structural control over the supramolecular peptide self-assembly that in turn, directly regulate the properties of resulting bioglass composite matrices and eventually influence the bone regeneration. Thus, kinetically controlled nanofibers (**1<sub>NF</sub>**) and thermodynamically stable twisted helical bundles (**1<sub>TB</sub>**) derived from a minimalistic peptide **1** are used as a template to design bioglass composites, **1<sub>NF</sub>BG** and **1<sub>TB</sub>BG** respectively (Scheme 5.1). The positively charged lysine moieties at the C-terminus

of the biomimetic peptide **1** are postulated to promote the mineralization of bioactive glass. Detailed structural investigations of the nanocomposites were carried out with advanced spectroscopy techniques *e.g.* Raman and XPS. The mechanical properties and stability of the nanocomposite hydrogels exhibit substantial increase in terms of elastic moduli and facilitate self-healing dynamic nature of the hydrogel composites. The bioactivity studies in simulated body fluid demonstrate evolution of a number of species of hydroxyapatite crystals over a few days. Lastly, biocompatibility of the composites and osteogenic activities with osteoblast like osteosarcoma cell line (U2OS cell line) show improvement and indicate its potential utility as a bone matrix mimicking materials. The present study precisely support for the development of a sustainable inorganic organic hybrid hydrogel with load bearing, self-healing ability and profound bioactivity which can be employed for bone tissue engineering application.

## 5.2. Biomineralization on self-assembled nanostructures:

The peptide amphiphile **1** was designed by tethering hydrophobic aromatic moiety fluorenylmethoxycarbonyl (Fmoc) at the N-terminus and two hydrophilic lysine units at the C-terminus of a short peptide sequence  $^N\text{VFFFA}^C$  through solid-phase synthesis.<sup>[15]</sup>



**Scheme 5.1.** Chemical structure of the peptide amphiphile **1**.

**5.2.1. Atomic Force Microscopy (AFM):** At physiological pH, the protonation of lysine amino groups renders it to self-assemble into kinetically controlled nanofibers **1<sub>NF</sub>** in aqueous medium. Further, heating the fibers furnished thermodynamically stable twisted

helical bundle  $1_{TB}$ . AFM images depict the peptide nanofibers ( $1_{NF}$ ) with height around 4 nm and twisted bundle ( $1_{TB}$ ) with height around 7-8 nm (Figure 5.1).

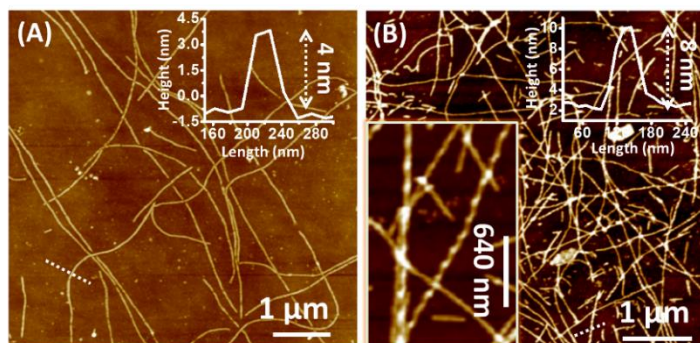


**Figure 5.1.** Comparison of AFM height image across the (A) kinetic nanofibers,  $1_{NF}$  (Inset shows height  $\sim 4$  nm) (B) twisted bundles,  $1_{TB}$  (inset shows height  $\sim 8$  nm, and periodic variation of height resulting in twisted bundle  $1_{TB}$ ).

**5.2.2. Persistence length ( $L_p$ ):** The persistence length of the nanofibers ( $1_{NF}$ ) and twisted bundles ( $1_{TB}$ ) were calculated using Easyworm software suite, coded in MATLAB that simplifies the analysis of the microscopic images. After uploading the PNG file of AFM height image, the Easyworm1 GUI allows fitting the contour of nanofiber chains to parametric splines. Data collected for 10 fibers was saved in one single .mat file which was

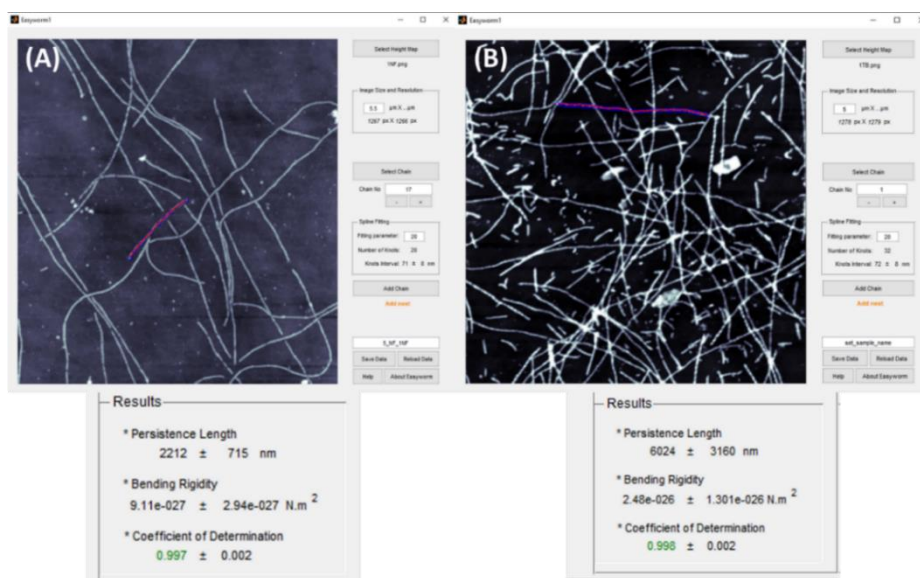
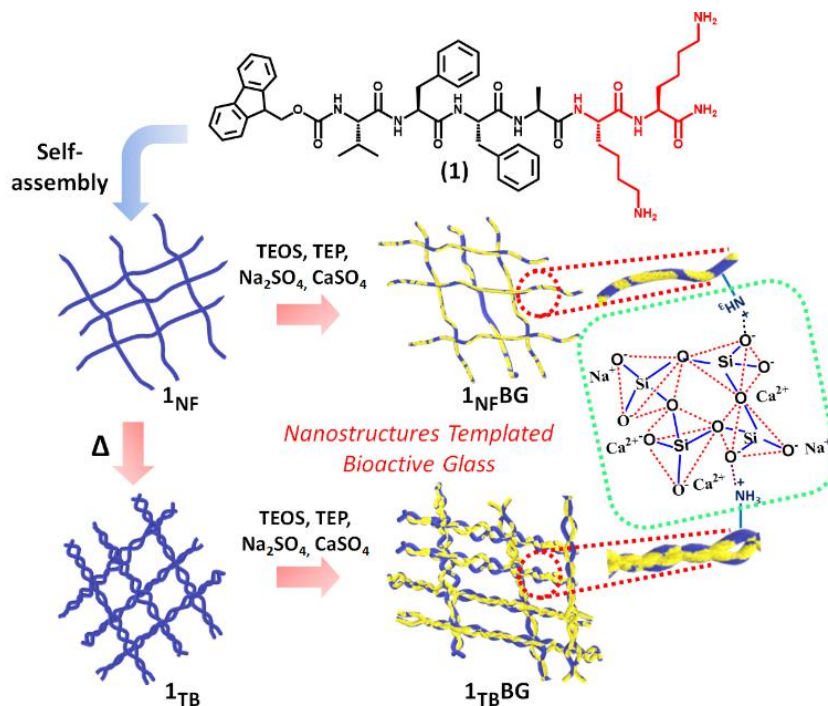


**Figure 5.2.** (A-B) Easyworm GUI fitting to find out the persistence length and bending rigidity of  $1_{NF}$  and  $1_{TB}$ .



uploaded in GUI Easyworm2 for the analysis purpose. Easyworm2 allows the calculation of persistence length ( $L_p$ ). Interestingly, the persistence length ( $L_p$ ) of the peptide nanofiber (**1NF**) is  $\sim 2.2 \mu\text{m}$ , comparable to that of the actin filaments ( $1.5 \mu\text{m}$ ). However, the twisted bundles of **1TB** show slightly higher  $L_p$  ( $6.0 \mu\text{m}$ ) as shown in Figure 5.2. Such chain bundling dictates higher bending rigidity and stiffness of the filaments to eventually modulate the elasticity, mechanical properties akin to the cytoskeletal filaments.<sup>[15,17,18]</sup> Thus, **1NF** and **1TB** were explored as a template for the *in situ* mineralization of bioactive glass to furnish **1NFBG** and **1TBBG**, respectively using bio-inspired synthetic approach.<sup>[19]</sup>

**5.2.3. Scanning Electron Microscopy (SEM):** Self-assembled peptide nanostructures has been explored for the mineralization and hybrid composites.<sup>[2,10]</sup> Here, the study envisage to evaluate the impact of same peptide's different self-assembled architecture on the



**Scheme 5.2.** Molecular structures of the peptide amphiphile, **1** and its pathway driven self-assembly to render nanostructures, **1NF** and **1TB**. The nanostructures with positively charged lysine moieties at surfaces are utilized as higher propensity sites for the bioactive glass mineralization. Tetraethyl orthosilicate (TEOS), triethylphosphate (TEP), sodium sulphate, and calcium sulphate were used as precursors to Si, P, Na and Ca content of the bioactive glass, respectively.

biomineralization. Briefly, to the template solution of **1<sub>NF</sub>** and **1<sub>TB</sub>**, TEOS and TEP were added sequentially with an interval of 15 min followed by the addition of network modifiers, sodium sulphate, and calcium sulphate (Scheme 5.2). After 30 min of incubation, the addition of sodium phosphate buffer (pH = 8) led to the formation of the composite hydrogels. This was further incubated for 2 days for the stabilization of *in situ* mineralization process of bioactive glass into the peptide hydrogel network. SEM was recorded to visualize *in situ* mineralization and eventual deposition of bioactive glass into the porous three dimensional fibrous network of peptide **1<sub>NF</sub>** and **1<sub>TB</sub>** (Figure 5.3A-B).

Interestingly, changes in the surface morphology as a result of the bioglass deposition in **1<sub>NF</sub>BG** and **1<sub>TB</sub>BG** were visualized owing to the difference in the respective template morphologies. Flattened deposition of bioactive glass for fibertemplated **1<sub>NF</sub>BG** and spicules type deposition similar to siliceous spicules from marine sponges for the twisted bundle templated **1<sub>TB</sub>BG** was observed. This reflected the role of supramolecular architecture in controlling the hydrogel composite topological features.

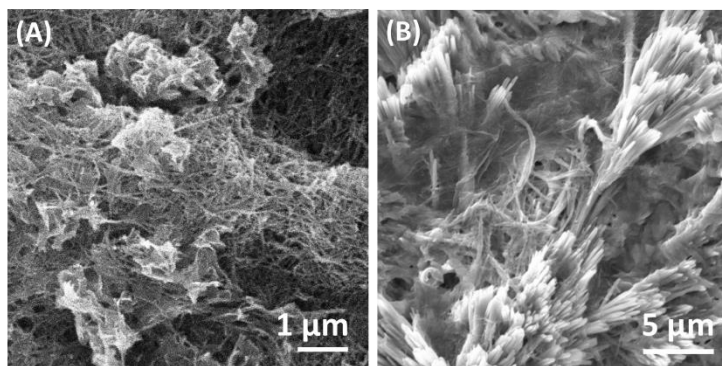


**Figure 5.3.** SEM images depicts mineralization of the bioglass on the peptide template for (A) **1<sub>NF</sub>BG** and (B) **1<sub>TB</sub>BG**.

**5.2.4. Energy Dispersive X-ray Spectroscopy (EDX):** The incorporation of bioglass into the peptide mesh network was confirmed by energy dispersive X-ray spectroscopy (EDX) with the characteristic elemental peaks of bioactive glass namely Si, P, Na, Ca, O present (Figure 5.4).

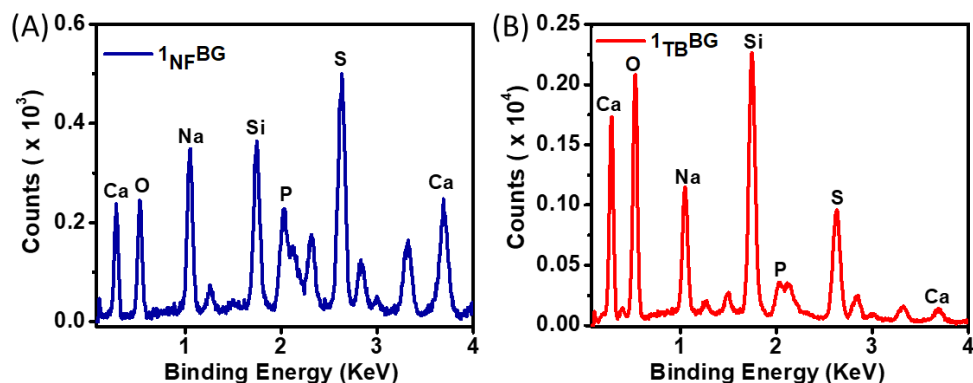


**Figure 5.4.** EDX analysis of elements for (A) **1NFBG** and (B) **1TBBG** composite showing the elements namely Si, P, Na, Ca and O making up the composition of the bioactive glass. Element S is observed due to the use of sulphate salt of sodium and calcium during hydrogel composite synthesis.

**5.2.5. Thermogravimetric Analysis (TGA):** The inclusion of inorganic content in the peptide hydrogel was further estimated from thermogravimetric analysis. The TGA graph for the dried gels and its composites clearly depict significant difference in terms of weight loss. The slight weight loss (<10%) up to 130 °C for all the samples were attributed to the loss of water molecules physically adsorbed on the surface (Figure 5.5). Thereafter, native peptides, **1NF** and **1TB** showed gradual weight loss up to 200 °C followed by rapid weight loss of ~ 35% and ~ 19% around 250 °C, associated with the chemically absorbed water and organic content of **1NF** and **1TB**. However, for the same range of temperature, the composites **1NFBG** and **1TBBG** remained comparatively stable. Further, for the entire range of thermal study up to 800 °C, ~ 98% weight loss was observed for **1NF** and **1TB** in comparison to mere ~ 40% and ~ 20% for **1NFBG** and **1TBBG**. This suggested significant incorporation of inorganic bioactive glass content into peptide hydrogel network thereby, enhancing the thermal stability of the composites. Presumably, the bundling process induces the entanglement of the nanofibers thereby bringing the lysine moieties in close vicinity that might accelerate the Ostwald nucleation and growth of the bioactive glass<sup>[20,21]</sup> and led to a higher inorganic content incorporated in **1TBBG** in comparison to **1NFBG**.

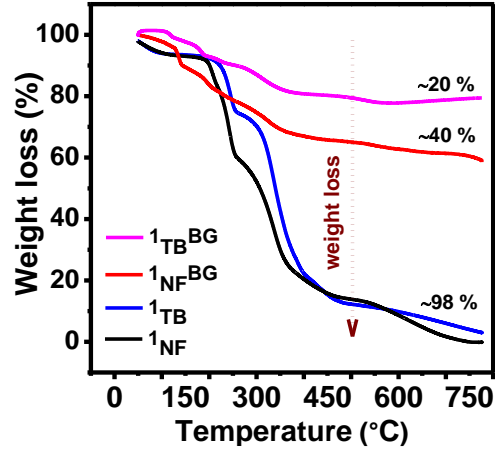


**Figure 5.5.** Thermo-gravimetric analysis for dried peptide hydrogels from nanostructures **1<sub>NF</sub>** and **1<sub>TB</sub>** and corresponding composites **1<sub>NF</sub><sup>BG</sup>** and **1<sub>TB</sub><sup>BG</sup>** indicating significant incorporation of inorganic components.

**5.2.6. X-ray Diffraction (XRD):** To investigate the effect of bioactive glass mineralization on the conformation adopted by the peptides, the synthesized hydrogel samples were lyophilized and subjected to X-ray diffraction analyses. The broad peak at  $2\theta$  degree values ranging from  $17^\circ$  to  $28^\circ$  centered at  $23^\circ$  observed in the diffraction pattern for both **1<sub>NF</sub><sup>BG</sup>**

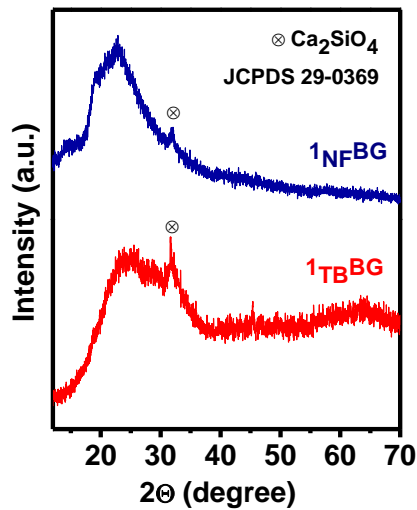


**Figure 5.6.** The broad peak at  $2\theta$  degree values ranging from  $17^\circ$  to  $28^\circ$  centered at  $23^\circ$  in the XRD diffraction pattern for both **1<sub>NF</sub><sup>BG</sup>** and **1<sub>TB</sub><sup>BG</sup>** reveals the amorphous nature of the in situ mineralized bioglass into the supramolecular peptide network hydrogel. Presence of  $\text{Ca}_2\text{SiO}_4$  phase in the XRD spectrum confirmed the incorporation of  $\text{Ca(II)}$  ion into the silica network of bioglass.

and **1<sub>TB</sub>BG** revealed the amorphous nature of the mineralized bioglass into the supramolecular peptide network hydrogel (Figure 5.6).<sup>[22]</sup> Furthermore, the presence of a sharp peak at 32.07° attributed to 116 plane of calcium silicate (Ca<sub>2</sub>SiO<sub>4</sub>) (JCPDS # 29-0369) along with the broad peak was indicative of the incorporation of calcium into the silica network of bioglass.<sup>[22]</sup> Noticeably, prominence of calcium silicate peak is slightly higher for **1<sub>TB</sub>BG** as compared to **1<sub>NF</sub>BG** indicating towards the possibility of higher bioactive response for **1<sub>TB</sub>BG**.

**5.2.7. Fourier Transform Infrared (FTIR) Spectroscopy:** The FTIR peaks at 1629 cm<sup>-1</sup> (amide I) and 1532 cm<sup>-1</sup> (amide II) for dried hydrogel peptide **1** indicate the existence of parallel β-sheet. The strong absorbance at 3276 cm<sup>-1</sup>, 3065 cm<sup>-1</sup> and 2935 cm<sup>-1</sup> correspond to the N-H stretching, -CH<sub>3</sub>/-CH<sub>2</sub> antisymmetric and symmetric stretching, respectively. Further, FTIR spectra was used to get insight of the involvement of different bonds for the mineralization process for the **1<sub>NF</sub>BG** and **1<sub>TB</sub>BG** samples. The characteristic amide I and amide II peaks of the peptide shift towards higher wavenumber upon bioglass composite formation.<sup>[23]</sup> Thus, chelation of metal ions to the amino acids moieties resulted in peak at 1632 and 1536 cm<sup>-1</sup> for amide I and II respectively (Fig. 5.7). Moreover, the characteristic peak of Si-O-Si (stretch at 1075 cm<sup>-1</sup> and bend at 465 cm<sup>-1</sup>), ring structure of the silicate

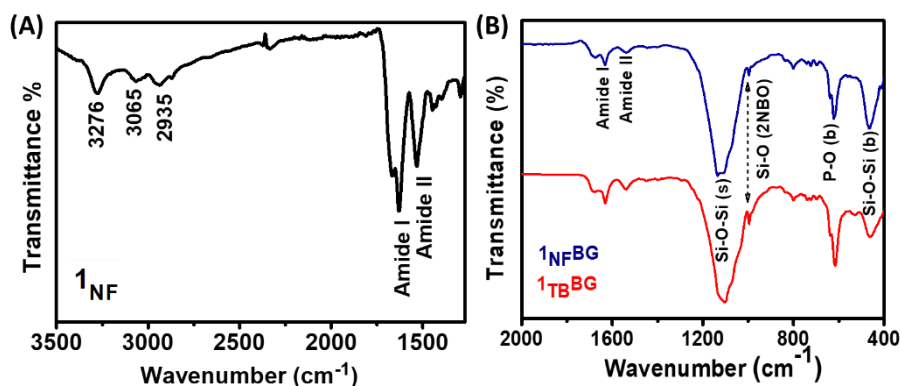


**Figure 5.7.** FTIR spectra for (A) dried hydrogel peptide **1** and (B) bioglass composites of **1<sub>TB</sub>BG** and **1<sub>NF</sub>BG**. After bioglass composite formation, characteristic amide I and amide II peaks of the peptide shift towards higher wavenumber due to chelation of metal ions to the amino acids moieties along with emergence of new peak ascribed to Si-O and P-O bond of bioglass could be noticed.

network ( $798\text{ cm}^{-1}$ ) and P-O ( $619\text{ cm}^{-1}$ ) bond along with Si-O (non-bridging oxygen) at  $995\text{ cm}^{-1}$  indicated the incorporation of bioglass into the peptide hydrogel. The presence of such non-bridging oxygen (NBO) owing to breaking of some of the Si-O-Si bonds validates an open network structure in silica based materials that can potentially accommodate alkali and alkaline-earth cations as network modifiers. The number density of such Si-O-NBO groups disrupts the continuity of the glassy network and plays pivotal roles to control the dissolution rate of the silica network through the formation of silanol groups at the glass surface resulting bioactive response of the materials.<sup>[24]</sup> A detailed understanding of the bonding configuration of composites and the identification of the Si-O-NBO groups immensely contribute toward improving the properties of new composites for tunable the bioactive responses.

**5.2.8. Raman Spectroscopy:** The atomic structures (described as  $Q^n$ ) of bioactive-peptide composites of  $1_{NF}BG$  and  $1_{TB}BG$  based on the presence of non-bridging (NBO) and bridging oxygen (BO), were elucidated through Raman spectroscopy (Figure 5.8A-B). The ‘Q’ refers to the different structures to describe network connectivity in a silica-based glass while ‘n’ is related to the average number of bridging oxygen atoms (n) per silicon and can range from 0 to 4.5 The Raman spectra recorded in the region of  $300\text{-}1700\text{ cm}^{-1}$  displays characteristic peaks for the peptides and corresponding bioglass samples. Raman peaks for symmetric

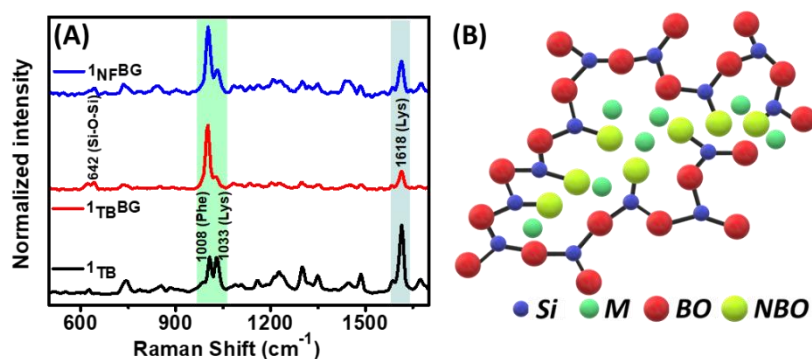


**Figure 5.8.** (A) Raman Spectra for  $1_{TB}$ ,  $1_{NF}BG$  and  $1_{TB}BG$  composites exhibiting decrease in characteristic Raman intensity for lysine moieties in  $1_{NF}BG$  upon bioglass mineralization. (B) Structural elucidation of non-bridging (NBO) and bridging oxygen (BO) in bioglass network (M indicates network modifiers). Bridging oxygens are shared by two silicon tetrahedral structures while non-bridging oxygens do not connect the two tetrahedral cations.

stretching and anti-symmetric bending of  $\text{NH}_3^+$  band of lysine at 1033 and 1618  $\text{cm}^{-1}$ , respectively was found to decrease in intensity upon glass mineralization for **1<sub>NF</sub>BG** and **1<sub>TB</sub>BG** samples.<sup>[25]</sup>

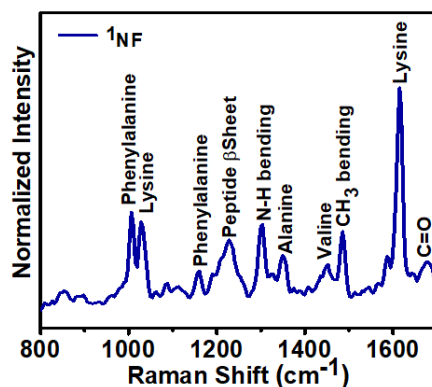


**Figure 5.9.** Raman Spectra for native peptide hydrogel **1<sub>NF</sub>** in the spectral region 800-1700  $\text{cm}^{-1}$  presents the characteristic Raman peak vibration for different amino acid of sequence VFFAKK along with its  $\beta$ -sheet structure.

Pertinently, the decrease in Raman peak intensity attributed to lysine moiety was higher in case of **1<sub>TB</sub>BG** as compared to **1<sub>NF</sub>BG**, thereby reflecting active participation of lysine unit in bioactive glass mineralization for **1<sub>TB</sub>BG** in corroboration with TGA data.

Emergence of new peak at 642  $\text{cm}^{-1}$  was ascribed to Si-O-Si bond of silica based bioactive glass.<sup>[26]</sup> However, characteristic Raman peaks in the region 970 to 1060  $\text{cm}^{-1}$  for different  $Q^n$  states of bioglass e.g.  $Q^2$  and  $Q^3$  are masked by the peaks of the phenyl alanine (Figure 5.9).<sup>[27,28]</sup>

**5.2.9. X-ray Photoelectron Spectroscopy (XPS):** To further assess the structural features with regards to the non-bridging and bridging oxygen constituent of bioglass, X-ray photoelectron spectroscopy was performed. The XPS survey scan spectrum for both **1<sub>TB</sub>BG** and **1<sub>NF</sub>BG** show well-defined peaks for Na, Ca, Si, P, N, S, O and C (Figure 5.10). The Si2p photoelectron spectra indicates a decrease in binding energy from 103.40 eV for **1<sub>NF</sub>BG** to 103.34 eV for **1<sub>TB</sub>BG** (Figure 5.10C). This might be due to relatively higher network modifier content in **1<sub>TB</sub>BG** that could result in higher proportion of non-bridging oxygen.<sup>[29]</sup>

Such observation is in agreement with TGA and Raman spectral analysis with higher inorganic content for **1<sub>TB</sub>BG**. Further, the ratio of non-bridging oxygen and bridging

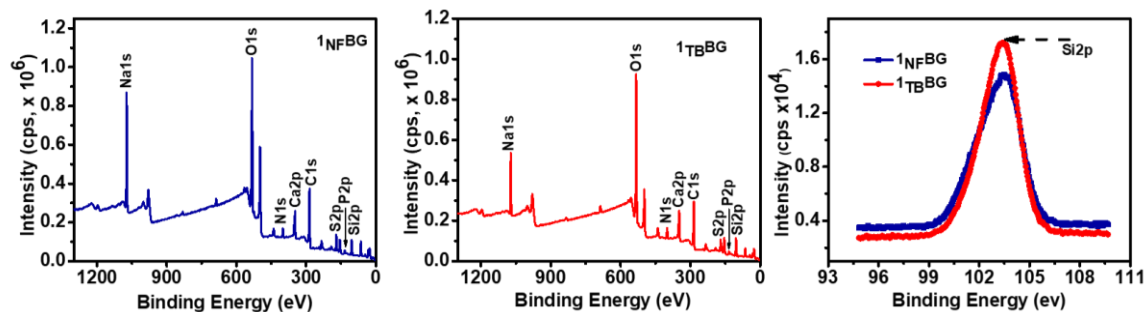


**Figure 5.10.** XPS survey scan for (A) **1<sub>NF</sub>BG** and (B) **1<sub>TB</sub>BG** showed characteristic binding energy peaks of carbon, oxygen, silicon, calcium, phosphorus, sodium, sulfur and nitrogen. (C) Si2p photoelectron spectra of **1<sub>NF</sub>BG** and **1<sub>TB</sub>BG**. A shift towards lower binding energy for **1<sub>TB</sub>BG** revealed the presence of higher network modifier content that could result in higher proportion of non-bridging oxygen associated with it.

oxygen was calculated through deconvolution of the O1s photoelectron spectra that furnished useful insight of different type of chemical bonding of the oxide ions in the silicate glasses (Figure 5.11A-B). A well resolved peak around 532 eV (solid line) associated with the Si–O–Si vibration (bridging oxygen groups, BO), accompanied by a shoulder at lower binding energies associated with Si-O-Na or Ca (non-bridging oxygen groups, NBO) was observed.<sup>[30,31]</sup> The small peak around 522 eV is an Auger electron signal of the ions.<sup>[29]</sup>

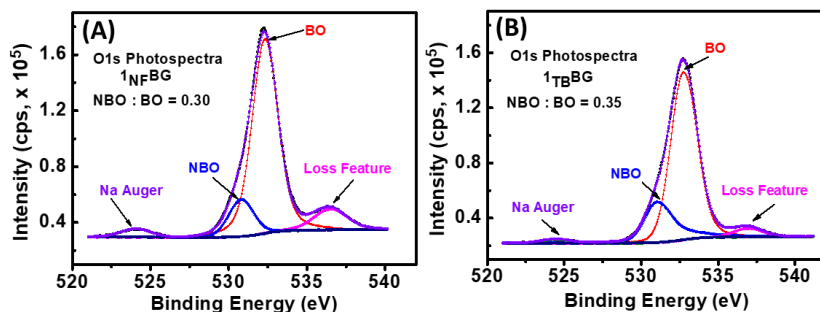


**Figure 5.11.** Comparison of deconvoluted O1s Photoelectron spectra for (A) **1<sub>NF</sub>BG** and (B) **1<sub>TB</sub>BG** shows different ratios of non-bridging to bridging oxygen.

NBO: BO ratio was found to be higher for **1<sub>TB</sub>BG** (0.35) in comparison to **1<sub>NF</sub>BG** (0.30). Increase in NBO: BO indicates a possible enhancement in the bioactivity response of the



biomaterial, **1<sub>TB</sub>BG**. This observation is in corroboration with XRD and FTIR data wherein a relatively higher calcium silicate peak and Si-O (NBO) peak in XRD and FTIR, respectively for **1<sub>TB</sub>BG** were observed.

**5.2.10. Rheological Studies:** The mechanical strength of the hydrogels and its composites were investigated using dynamic oscillatory rheology experiment. A characteristic frequency sweep experiment for the native peptide nanostructures exhibited the structural implications over the hydrogel strength with **1<sub>TB</sub>** having higher  $G'$  modulus than **1<sub>NF</sub>** (Figure 5.12A-B). Also, this is evident from the frequency dependent weak gel behavior of **1<sub>NF</sub>**, while **1<sub>TB</sub>** frequency independent behavior. It is pertinent to note that bundling increases the stiffness of the native peptide fibers resulting in enhanced elastic moduli for **1<sub>TB</sub>** relative to

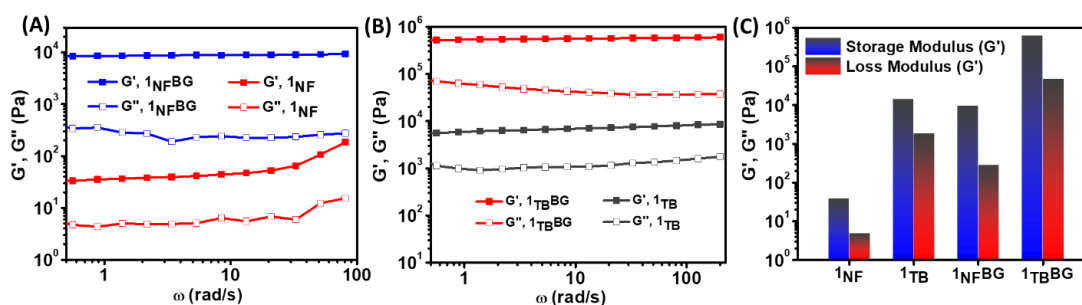


**Figure 5.12.** (A) Frequency sweep oscillatory rheology for the hydrogels (1 w/v%, pH 7) obtained by physical crosslinking of the kinetic nanofibers, (A) **1<sub>NF</sub>** and bioglass composite, **1<sub>NFBG</sub>** (B) **1<sub>TB</sub>** and corresponding bioglass composite, **1<sub>TBBG</sub>**. (C) Bar diagram showing the comparison between the storage moduli,  $G'$  and loss moduli,  $G''$  values at 0.1% strain for **1<sub>NF</sub>** and **1<sub>TB</sub>** along with corresponding bioglass composites.

**1<sub>NF</sub>**. The comparison of the mechanical response of the composites **1<sub>NFBG</sub>** and **1<sub>TBBG</sub>** with **1<sub>NF</sub>** and **1<sub>TB</sub>** native hydrogels showed more than 2-fold increase in the  $G'$  values of the in situ mineralized bioglass hydrogel than the corresponding native peptide hydrogel (Figure 5.12.C). A typical amplitude sweep study demonstrated much higher yield stress values for bioglass composites as compared to the native hydrogels (Figure 5.13.A-B). The critical strain value and corresponding yield stress were estimated by crossover values of  $G'$  and  $G''$ . Critical strain and yield stress for **1<sub>NF</sub>** is 6.17% and 1.88 Pa, **1<sub>NFBG</sub>** 45.60% and 1150 Pa, **1<sub>TB</sub>** 13.30% and 181 Pa and **1<sub>TBBG</sub>** 53.00% and 5780 Pa. The higher yield stress values

indicate resistance to flow under applied stress and is favorable for the load bearing applications in biological systems. Moreover, the difference between elastic moduli values indicated hard texture of the bioglass peptide composite hydrogel in comparison to a soft texture of the native hydrogel. Improvement in the This corroborates the increase in NBO:BO ratio on the XPS studies for enhanced elastic moduli values particularly for **1<sub>TB</sub>BG**, its elastic moduli were obtained comparable to natural bone.<sup>[32,33]</sup>

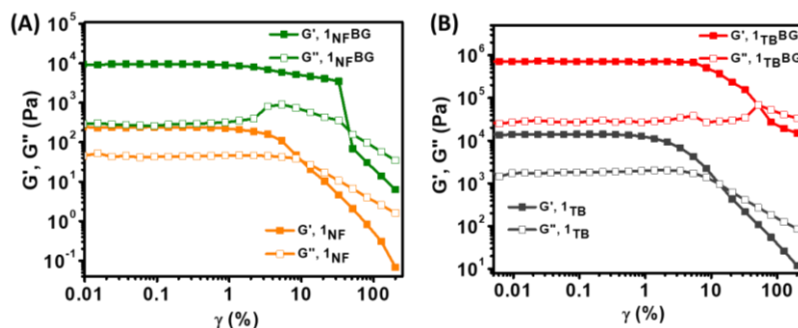


**Figure 5.13.** Comparative amplitude sweep oscillatory rheology experiments for the native hydrogels (**1<sub>NF</sub>** and **1<sub>TB</sub>**) and corresponding bioglass composites (**1<sub>NF</sub>BG** and **1<sub>TB</sub>BG**) obtained from (A) nanofibers (**1<sub>NF</sub>**) and (B) twisted bundles (**1<sub>TB</sub>**). The measurement was done with a constant angular frequency of 10 rad/s for the strain range 0.01-200 at 37 °C.

Further, dynamic oscillatory rheology was employed to rheological property of the hydrogel system indicates that the bioactive glass acted as reinforcement fillers. It involves continuous monitoring of storage moduli while straining of the gel until failure and then its recovery to confirm the self-healing nature of the gel (Figure 5.14.A). Interestingly, self-healing property of the **1<sub>TB</sub>BG** hydrogel was observed at room temperature. When blocks of gels were brought in close proximity, they self-adhered to each other in a few second, without the use of any external healing agent. For clarity, one of the blocks was doped using methyl orange. Using an alternative dye doped and undoped blocks, a single triblocks could be constructed owing to intrinsic self-healing dynamic nature of the composites. Thixotropic nature of **1<sub>TB</sub>BG** was investigated by alternative variation of 0.1% and 100% strain for three cycles, which exhibited instantaneous self-recovery of the network after removal of high strain (Figure 5.14.B). Such shear recovery character up to ~80% of the original values for both moduli,  $G'$ ,  $G''$  of **1<sub>NF</sub>BG** and **1<sub>TB</sub>BG** composites indicated the injectable nature of the supramolecular hydrogel composites.

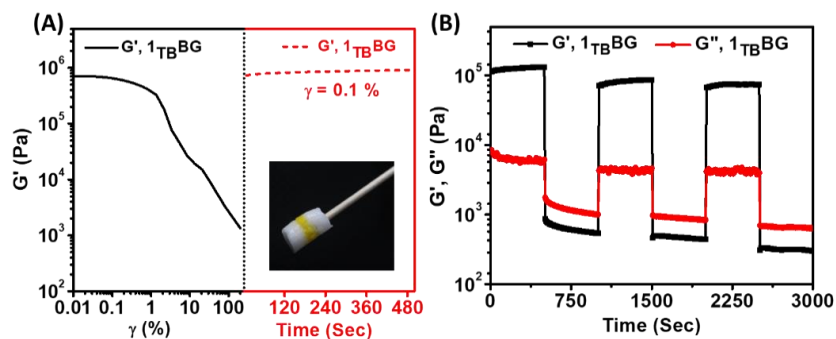


**Figure 5.14.** (A) Dynamic oscillatory rheology to quantify the speed of recovery by shearing **1<sub>TB</sub>BG** hydrogel at increasing strain (from 0.001 until 100%) at a constant angular frequency (10 rad/s), after which the recovery was monitored at 0.1% strain and 10 rad/s. Inset: digital image showing the self-healing property of the **1<sub>TB</sub>BG** composite. The self-healed single block prepared from three color-coded blocks held vertically. (B) Thixotropic behavior of **1<sub>TB</sub>BG** composite under alternative cycle of high (100%) and low strains (0.1%).

### 5.3. Bioactivity Study:

**5.3.1. Scanning Electron Microscopy (SEM):** The distinctive nature of the bioactive glass promotes rapid bone formation *via* dissolution of critical concentration of Si, P, Ca and Na ions from its surface in body fluids thereby, promoting intracellular and extracellular responses. Under *in vitro* condition, bioactivity in terms of hydroxyapatite formation for the

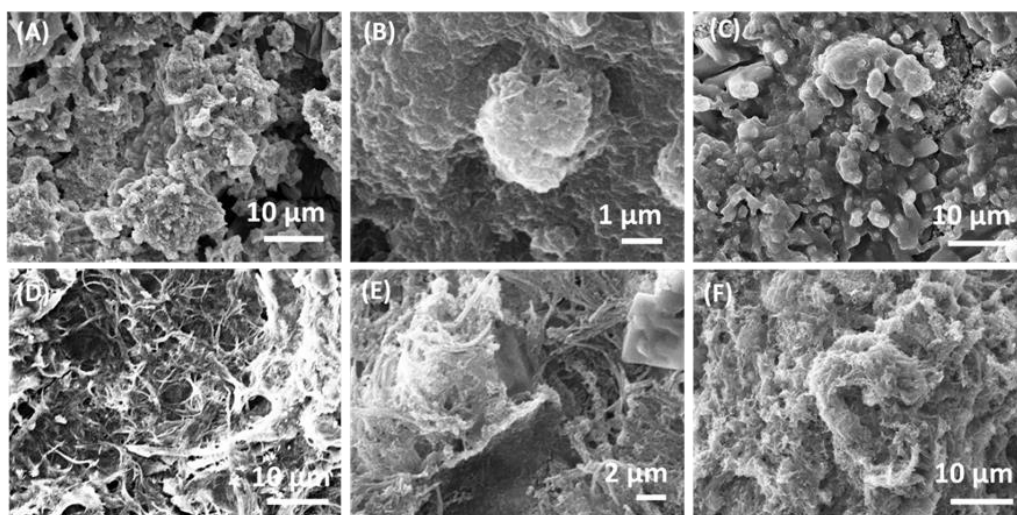


**Figure 5.15.** SEM images exhibiting deposition of hydroxyapatite over the bioglass mineralized on the peptide template, for **1<sub>NB</sub>BG** and **1<sub>TB</sub>BG** upon immersion in SBF for (A-C) and (D-F) after 4, 7, and 25 days respectively. With increase in immersion time in SBF, proportionally calcium phosphate deposition on the hydrogel surface increases.

bioglass composite was evaluated after immersion in simulated body fluid that exhibited a remarkable change in the microstructures for **1<sub>TB</sub>BG** over time. This could be attributed to the deposition of calcium phosphate (Figure 5.15) that forms owing to a sequence of chemical exchange occurring on the surface of bioactive glass.<sup>[34]</sup> The ratio of calcium and phosphorus percentage, as obtained from EDX data indicated an increase in the surface coverage with calcium phosphate deposition for both the peptide bioglass composites with

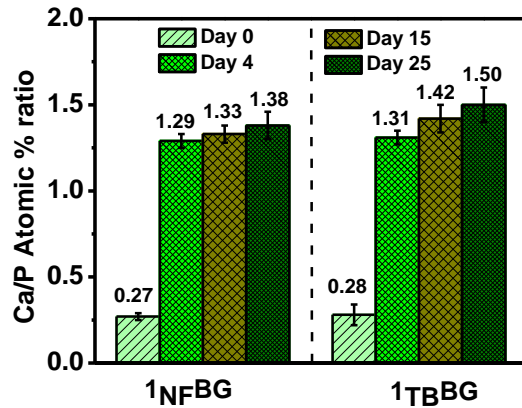


**Figure 5.16.** Bar diagram showing the comparison of Ca/P ratio as obtained from EDX for **1<sub>NF</sub>BG** and **1<sub>TB</sub>BG** at different time interval of SBF immersion.

longer immersion time in SBF (Figure 5.16). Thus, Ca:P ratio for **1<sub>NF</sub>BG** increased to 1.33 after 15 day, that resembled with octacalcium phosphate-a precursor to hydroxyapatite<sup>[35,36]</sup> while for **1<sub>TB</sub>BG**, the ratio reached a value of 1.42 after the same time period. This suggest a faster deposition process for **1<sub>TB</sub>BG** compared to **1<sub>NF</sub>BG** to furnish a Ca:P ratio close to natural hydroxyapatite (1.67). Such observation is in corroboration with O1s photoelectron analysis in terms of NBO: BO ratio for **1<sub>TB</sub>BG** compared to **1<sub>NF</sub>BG**. The presence of non-bridging oxygen is crucial in controlling the dissolution rate of silica and in turn, directs the bioactivity towards hydroxyapatite formation.<sup>[29]</sup>

**5.3.2. Fourier Transform-Infrared Spectroscopy (FTIR):** FTIR spectra showed a decrease in characteristic peaks of Si-O (NBO) of bioglass with simultaneous emergence of peaks ascribed to characteristic vibration modes carbonate ( $736\text{ cm}^{-1}$ ) and phosphate ( $560\text{ cm}^{-1}$ ) of hydroxyapatite (Figure 5.17).

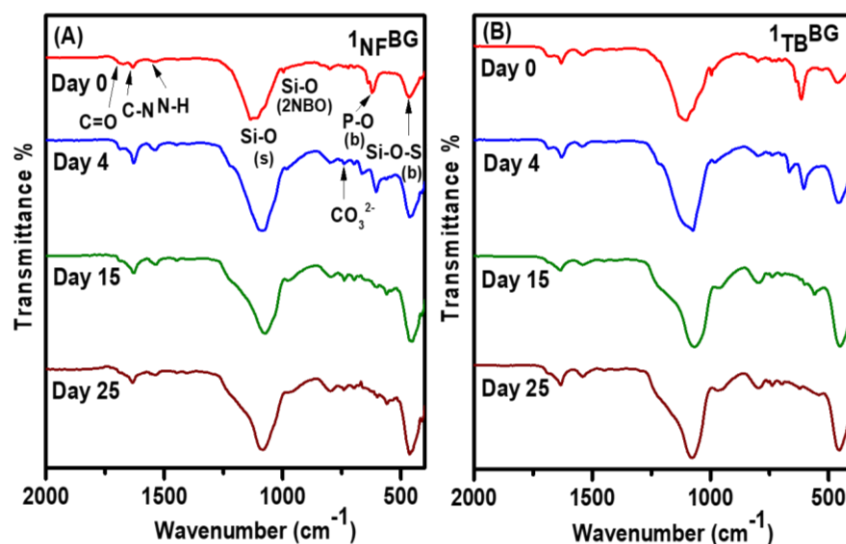


**Figure 5.17.** FTIR spectra for (A)  $1_{NF}BG$  and (B)  $1_{TB}BG$  before and after immersion in SBF for different time periods. Characteristic peaks namely, Si-O-Si,  $PO_4^{3-}$ ,  $CO_3^{2-}$ , N-H, C-N are marked on the graph. Increase in  $CO_3^{2-}$  and  $PO_4^{3-}$  peaks are observed with increase in immersion time in SBF.

**5.3.3. X-ray diffraction Studies (XRD):** XRD exhibited emergence of new peaks attributed to octacalcium phosphate (JCPDS-26-1056) and carbonate hydroxyapatite (JCPDS-19-0272) revealing the biphasic calcium phosphate deposition (Figure 5.18) upon soaking  $1_{NF}BG$  composite in SBF. It is pertinent to note that octacalcium phosphate is a precursor to

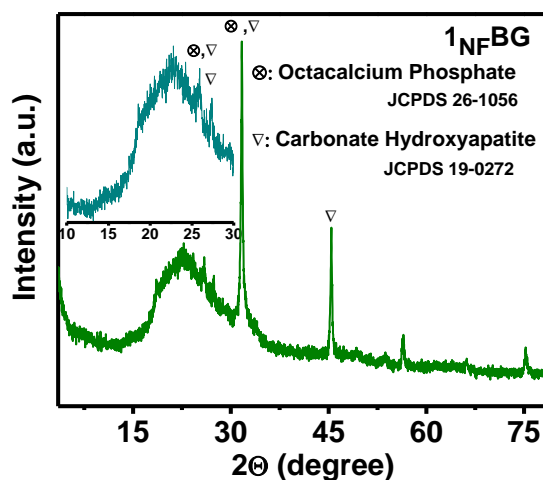


**Figure 5.18.** XRD spectrum for  $1_{NF}BG$  after immersion in SBF for 15 days indicates the presence of biphasic forms of octacalcium phosphate and carbonate hydroxyapatite (Inset shows the XRD spectrum region of  $1_{NF}BG$  from  $10$  to  $30^\circ$   $2\theta$  value).

hydroxyapatite and its granules are evaluated for their bone regenerative capability in collagen matrix. With the increase in immersion time, the growth of hkl plane orientation in 211, 203, 322 and 324 directions for octacalciumphosphate and 002, 112, 203 for carbonate hydroxyapatite becomes prominent for both the bioglass composites (Figure 5.19).

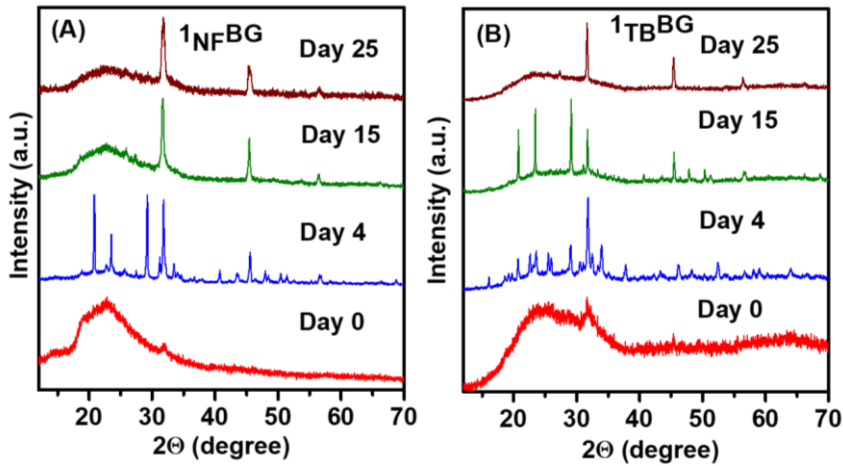


**Figure 5.19.** XRD data for (A) **1NFBG** and (B) **1TBBG** before and after SBF immersion for different time periods. Different phases of calcium phosphate are formed on immersion in SBF and eventually preferential growth in the (112) plane at  $2\theta = 32.17^\circ$  predominates. This is the characteristics of the carbonate hydroxyapatite (JCPDS 19-0272).

**5.3.4. Effect of pH:** It is to be noted that carbonate apatite possess compositions closer to bone and dental enamel than hydroxyapatite. However, relation between carbonate apatite and hydroxyapatite is vital, because carbonate increases the chemical reactivity of apatite<sup>[37]</sup> influencing the crystallinity on bioglass surface. Such formation of crystal phase decreases the formation kinetics of the apatite layer on the bioglass surface but do not totally suppress the formation of such layer. During the bioactive test of **1NFBG** and **1TBBG**, a gradual increase pH from 7 to 8 for the corresponding SBF solutions was observed that reached subsequent saturation plateau within 20 days (Figure 5.19). The increase in pH resulted in a decrease in solubility of the hydroxyapatites thereby, assisting its precipitation process.<sup>[31]</sup>

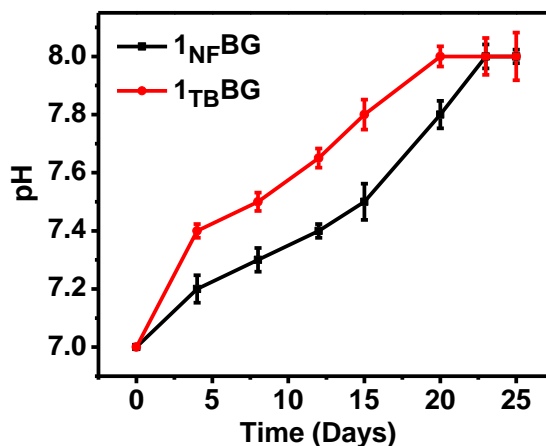


**Figure 5.20.** Change of pH of the solution as monitored during bioactivity studies for the bioglass composites of **1NFBG** and **1TBBG** in SBF at different time interval. A gradual increase in pH value results in a decrease in solubility of the hydroxyapatite and thus assists its precipitation process. Interestingly, the increase in pH value was comparatively faster for **1TBBG** suggesting faster dissolution rate of bioactive glass in **1TBBG**.

**5.3.5. Biocompatibility Study:** After confirming bioactive nature of the composites, further study of the biological response in terms of biocompatibility of the native peptide nanostructures and corresponding bioactive glass composites, **1NFBG** and **1TBBG** were carried out against human osteoblast like osteosarcoma (U2OS) and keratinocyte (HaCaT) cell lines. In order to estimate bio-compatibility, media in contact with different concentrations of the pre-sterilized samples (10, 50, 500 and 1000  $\mu\text{g/mL}$ ) for 48 h at 37  $^{\circ}\text{C}$  were made to interact with individual cell lines followed by MTT analysis after 48 h (Figure S13). All the samples showed internal variation in terms of the levels of cytotoxicity. Nonetheless, the overall viability for all were found to be above 85% thus signifying good bio-compatibility of hydrogels (Figure 5.21) against both cell lines.

Further, evaluation of cellular morphology through bright field microscopy on native and composite hydrogel surfaces showed that the cells exhibited an initial spherical morphology that is gradually stretched with time. For the native peptide hydrogel (**1NF** and **1TB**) elongation of the adhered cells was absent (Figure 5.22) although the anchorage might be attributed to the peptide cellular-ECM/integrin interaction which facilitated such cellular behavior.



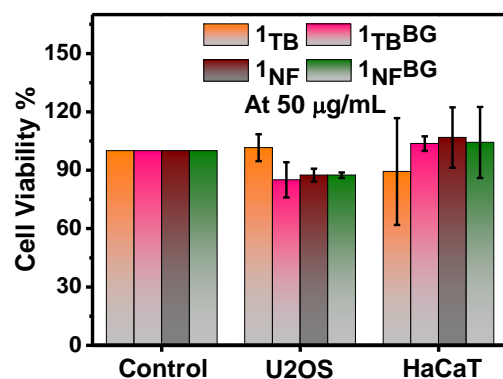


**Figure 5.21.** MTT assay for the native hydrogels, **1<sub>NF</sub>** and **1<sub>TB</sub>** along with the corresponding bioglass composites, **1<sub>NFBG</sub>** and **1<sub>TB</sub>BG** against U2OS and HaCaT cell lines after 48 h interaction. Untreated well was considered as positive control. Cells were treated with media in contact with the respective 50 µg/mL samples for 48 h. Data represents mean ± SD from 3 experiments carried out in triplicate.

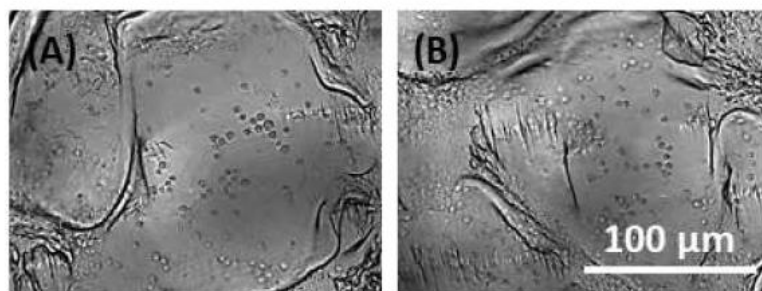


**Figure 5.22.** Native peptide hydrogel construct (A) **1<sub>NF</sub>** and (B) **1<sub>TB</sub>** showed flattened out morphology of the U2OS cell line under the optical microscope. The anchorage might be attributed to the peptide cellular-ECM/integrin interaction which facilitates such cellular behavior.

The hydrogel composites (**1<sub>NFBG</sub>** and **1<sub>TB</sub>BG**) exhibited excellent adherence and spreading leading to inter cellular network with time. Cell fingers longer than 10 µm are another salient feature that suggest complete cell spreading (Fig. 5.23).<sup>[34]</sup> Interestingly, over a period of 7 days, **1<sub>TB</sub>BG** showed more cell fingers as compared to **1<sub>NFBG</sub>** that might suggest the difference in surface topological feature and network elasticity in the composites to enhance spread area. Moreover, the viscoelastic nature and stiffness of gels are known to positively impact cellular attachment of keratinocytes<sup>[35]</sup> and U2OS<sup>[36]</sup> cells. Here, the differential persistence length for the peptide nanofibers and twisted bundles dictates mineralization efficacy leading to eventual difference in network elasticity. Thus, relatively



stiffer and twisted bundle mediated **1<sub>TB</sub>BG** composite correlates to the nature of bone cells microenvironment to facilitate efficient bone cell adhesion, spread area and cell-cell interactions in comparison to **1<sub>NF</sub>BG**.<sup>[36,37]</sup> This ensured that proportionally higher bioactive glass mineralized hydrogel construct **1<sub>TB</sub>BG** provided apt biochemical and biomechanical cues for favourable cellular adhesion, spread and growth which is of fundamental importance for tissue development.<sup>[34]</sup>

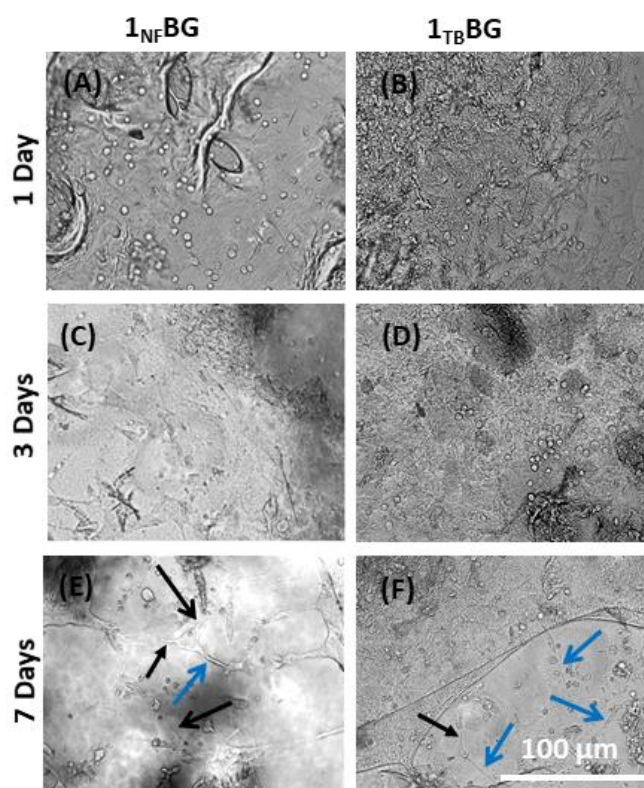


**Figure 5.23.** The morphology of the U2OS cells imaged under the optical microscope after incubating with **1<sub>NF</sub>BG** and **1<sub>TB</sub>BG** show spread morphology of the U2OS cell line with time. Black arrows show cell fingers while blue arrows show cell fingers longer than 10  $\mu\text{m}$ . (Scale Bar: 100  $\mu\text{m}$ ).

## 5.4. Conclusions

Thus, in summary, elegant design of a minimalistic peptide amphiphile was demonstrated that by the mediation of temperature-driven self-assembly modulates its structure from nanofibers to twisted helical bundles that are in close mimic to collagen helix.

Such pathway driven self-assembled peptide nanostructures served as a template for the bioactive glass in situ mineralization and control its structural-functional features. In comparison to nanofibers, twisted helical bundles imparted a higher proportion of non-bridging oxygen sites on the bioglass surface and in turn enhanced its hydroxyapatite mineralization efficacy. The bundling of the fibers and consecutive biomineralization increased the stiffness of the hydrogel network resulted in an efficient mechanical response close to the natural bone for twisted bundle templated bioglass hydrogel composites. Overall, this was the first example to exploit pathway-driven peptide self-assembly for developing supramolecular inorganic-organic hybrid hydrogel composites with variation in mechanical stiffness of the scaffold in the context of matrix microenvironment cues. Such biomaterials with topological, structural and mechanical control can be employed in the future with its high load-bearing ability and profound bioactivity as an implant coating for bone tissue engineering application.

## **5.5. Experimental Section**

### **5.5.1 Materials:**

All Fmoc protected amino acids, activator (diisopropyl carbodiimide), piperazine, triisopropylsilane, 1,2-ethanedithiol, tetraethyl ortho-silicate (TEOS), triethyl phosphate (TEP) and Hanks balanced salt solution were purchased from Sigma Aldrich. Oxyma, Fmoc-Rink amide MBHA resin, water, ethanol, and DMF were obtained from Merck. Trifluoroacetic acid (TFA) was purchased from SRL chemicals. Anhydrous sodium sulphate and calcium sulphate were procured from Emparta and SD Fine chemicals ltd. respectively.

### **5.5.2 Methods:**

**5.5.2.1. Design of self-assembled peptide templated bioactive glass:** Peptide amphiphile, **1** was synthesized using standard solid state synthesis performed in Liberty Blue CEM, Matthews, NC, USA as described previously in chapter 3.<sup>[15]</sup> The peptide amphiphile ( $c = 8.6 \text{ mM}$ ) was dissolved in water to result kinetically stable nanofibers in aqueous media at

25 °C and is referred as **1<sub>NF</sub>**. Upon heating at 80 °C for 30 min, nanofibers were converted to thermodynamically stable twisted bundle (**1<sub>TB</sub>**) in a temperature dependent self-assembly pathway.<sup>[15]</sup> Both **1<sub>NF</sub>** and **1<sub>TB</sub>** were utilized as a template for bioactive glass synthesis **1<sub>NF</sub>BG** and **1<sub>TB</sub>BG**, respectively.<sup>[29]</sup> To the template aqueous solution, different bioglass precursors namely, TEOS (223 mM), TEP (27 mM), sodium sulphate (112 mM) and calcium sulphate (115 mM) were added in sequential manner at an interval of 15 min at ambient condition. The hydrogel composite was formed upon cross-linking the peptide-bioglass fibers with 15 mM sodium phosphate buffer (pH 8). The whole system was then incubated for 48 h to complete in situ mineralization process. Thereafter, the bioglass mineralized hydrogels were characterized for the morphological, textural and structural properties. Noticeably, sulphate salts of sodium and calcium were preferred over acetate and chloride owing to their higher ionic strength that led to the entanglement of the nanofibers, turning free-flowing solution into hydrogels.<sup>[24]</sup>

**5.5.2.2. Thermo-gravimetric Analysis (TGA):** TGA was performed using Perkin Elmer thermo-gravimetric analyser TGA 4000 for all the samples heated from 50 to 800 °C at a heating rate of 10 °C/min.

**5.5.2.3. Atomic Force Microscopy (AFM):** 10 µL of 0.86 mM peptide solution was drop-casted on silicon wafer. After 5 minutes, the silicon wafer was washed with 500 µL water using micropipette to remove excess peptide. The silicon wafer was then left to be air dried in a desiccator. AFM height images were recorded by tapping mode on a Bruker Multimode 8 scanning probe microscope with silicon cantilever (Bruker) and analysed using the software NanoScope Analysis 1.5.

**5.5.2.4. Scanning Electron Microscopy (SEM):** 10 µL of peptide bioglass composite gel was drop-casted on double sided carbon tape. It was gold coated in sputtering machine before mounting on the stage and SEM image was recorded on JEOL JSM-IT300 attached with energy dispersive X-ray spectroscopy for elemental determination and quantification.

Different magnification images were collected under vacuum using 15 kV accelerating voltage and a working distance automatically adjusted for optimal image quality.

**5.5.2.5. X-ray Diffraction (XRD):** XRD spectra were recorded using Bruker D8 advance Powder X-ray diffractometer operated at 20 mA current and 40 KV using Cu K $\alpha$  source with wavelength of 1.54 Å.

**5.5.2.6. Fourier Transform Infra-Red spectroscopy (FTIR):** FTIR spectra were recorded in the range of 4000 to 400 cm<sup>-1</sup> as an attenuated total reflectance (ATR) mode using Bruker Vertex 70 FTIR spectrophotometer and analysed through Opus Software.

**5.5.2.7. Raman Scattering Spectroscopy:** Raman spectra for all the lyophilized powder samples were acquired with a WiTEC alpha300R microscope in Raman mode using a 20x (Numerical Aperture 0.9) and 532 nm (Elaser = 2.33 eV) Nd:YAG laser operating at constant power for each experiment up to ~75 mW. Raman data were collected by the WiTEC Control software and analysed in the WiTEC Project software. Spectra were collected using an integration time of 1 s.

**5.5.2.8. High-resolution X-ray photoelectron spectroscopy (XPS):** 10  $\mu$ L of the peptide bioglass composite (1 mg/mL in acetone) was dropcasted on silicon wafer. XPS spectra of the samples were recorded with Thermo Scientific Nexsa surface analysis system using monochromatic Al K $\alpha$  X-rays of energy 1486.6 eV under a vacuum of  $5 \times 10^{-10}$  torr and analysed through Advantage software.

**5.5.2.9. Rheology:** The linear viscoelastic region, storage modulus, loss modulus and thixotropic characteristics were studied using a Rheoplus 302 device using parallel plate (PP-25) geometry at a measuring distance of 0.2 mm at 37 °C. Amplitude sweep studies were performed from 0.01% to 250% strain at 10 rad/s, while frequency sweep oscillatory rheology were conducted from 0.5 to 100 rad/s at 1% strain in the linear viscoelastic region.

For evaluating self-healing ability of the hydrogel, thixotropic studies were performed wherein the gel network was completely broken at 100% strain, however, it recovers its gelation ability when the strain value was switched to 0.1%. Three consecutive cycles of high (100%) and low strain (0.1%) were performed at a constant angular frequency of 10 rad/s.

**5.5.2.10. Bioactivity Test:** An in vitro evaluation of the bone forming activity of the sample was performed in simulated body fluid (SBF) by monitoring the formation of hydroxyapatite on the surface of the bioglass incorporated hydrogel. To check the bioactivity of the hydrogels **1<sub>NF</sub>BG** and **1<sub>TB</sub>BG**, samples of equal shape and size of 10 mm was incubated in Hanks' Balanced Salt solution, an extracellular solution with an ionic composition similar to human blood plasma for different time intervals on shaker at 37 °C under sterile conditions and the SBF solution was replaced twice a week. The formation of hydroxyapatite was monitored on samples surface through SEM, XRD and FTIR, for evaluating bone forming activity of the sample.

#### **5.5.2.11. Cell Culture Studies:**

**Seeding method of U2OS cells:** For cell culture, the gels were prepared in wells of 96 well plates under sterile conditions. The swollen cylindrical hydrogels (50 µL/well) cast in each well of the 96 well plate. The gels were dried in 37 °C incubator for approximately 24-48 h in order to remove its water content. Once dried the hydrogels were washed twice with sterile phosphate buffer saline (PBS, pH 7.4) in order to remove any unreacted precursor. The step was carried out as unreacted bioactive glass precursors may prove detrimental to cellular growth environment. The hydrogels were then immersed in DMEM-F12 with 10% FBS for 24 h and kept in 37 °C, 5% CO<sub>2</sub> incubator for optimizing the growth conditions in the hydrogel. Following day, the media was replaced with fresh DMEM-F12/FBS medium contained pre counted cells for seeding at required densities for different experiments. For 3D cultures, freshly prepared gels once cast and pre-incubated at 37 °C were mixed through

gentle shaking with equal volume of cell suspensions, allowed to gel for 30 minutes and reconstituted with media.

**Cell-viability assay:** MTT assay was carried out to evaluate the biocompatibility the various peptide hydrogel constructs. The native hydrogels (**1<sub>NF</sub>** and **1<sub>TB</sub>**) and corresponding bioglass samples (**1<sub>NFBG</sub>** and **1<sub>TBBG</sub>**) were evaluated against human osteoblast like osteosarcoma (U2OS) cells. MTT (3-[4,5-dimethylthiazole-2-yl]-2,5-diphenyltetrazolium bromide) is a water soluble tetrazolium salt, which gets converted to insoluble purple formazan crystals through cleavage of its tetrazolium ring by succinate dehydrogenase. Succinate dehydrogenase is a mitochondrial enzyme whose assessment indicates the metabolic status of the cell thus hinting at its viability. The formazan crystals are impermeable to the cell membranes and therefore accumulates in healthy cells. Around 10,000 U2OS (human osteosarcoma cell line) cells per well was added in hydrogel in a 96 well plate. DMEM F12 (ThermoFisher scientific) was used as media constituted with 10% fetal bovine serum (FBS). Wells without hydrogels were taken as control for comparison. The plates were incubated for 24 hours in a 37 °C, 5% CO<sub>2</sub> incubator. 5 mg of MTT was dissolved in 1 mL of PBS and filter sterilized. 10 µL of the solution was diluted with 90 µL of OptiMEM (Invitrogen) and added to each well thus making a final concentration of 0.5 mg/mL per well. The solution was mixed thoroughly with the hydrogel so that cells inside the hydrogels are granted access. After incubating the MTT with samples in the incubator for 2 h, MTT solution was removed. DMSO was added (100 µL/well) to dissolve the formazan crystals in the wells. After 1 hour of incubation on a shaker, DMSO was removed from the wells and added to a new 96 well plate. The step was carried out to avoid any interference by the hydrogels in the well while absorption measurement. Absorbance was taken at 570 nm in a TECAN multiplate reader. The MTT assay was carried out in triplicates of three wells for each sample. Wells without hydrogels were taken as control.

**5.5.2.12. Evaluation of cellular morphology through bright field microscopy on hydrogel surfaces:** In order to evaluate cellular morphology, attachment, spreading, visual

proliferation and stability of hydrogel in culture conditions, around  $10^3$  cells were seeded in the hydrogels. The observations were made through an optical microscope (Fluor Cell Imaging Station) after 1, 3 and 7 days.

## 5.6. References

- [1] J. H. Collier, J. S. Rudra, J. Z. Gasiorowski, J. P. Jung, *Chem. Soc. Rev.* **2010**, *39*, 3413.
- [2] J. Candreva, E. Chau, E. Aoraha, V. Nanda, J. R. Kim, *Chem. Commun.* **2018**, *54*, 6380.
- [3] A. Anitha, D. Menon, T. B. Sivanarayanan, M. Koyakutty, C. C. Mohan, S. V. Nair, M. B. Nair, *ACS Appl. Mater. Interfaces* **2017**, *9*, 26707.
- [4] O. J. G. M. Goor, S. I. S. Hendrikse, P. Y. W. Dankers, E. W. Meijer, *Chem. Soc. Rev.* **2017**, *46*, 6621.
- [5] A. K. Awasthi, S. D. Bhagat, R. Ramakrishnan, A. Srivastava, *Chem. – A Eur. J.* **2019**, *25*, 12905.
- [6] V. Nanda, *Biophys. J.* **2016**, *110*, 2291.
- [7] C. L. Chen, N. L. Rosti, *Angew. Chemie - Int. Ed.* **2010**, *49*, 1924.
- [8] S. Segman-Magidovich, H. Grisaru, T. Gitli, Y. Levi-Kalishman, H. Rapaport, **n.d.**, DOI 10.1002/adma.200702125.
- [9] L. C. Palmer, C. J. Newcomb, S. R. Kaltz, E. D. Spoerke, S. I. Stupp, *Chem. Rev.* **2008**, *108*, 4754.
- [10] R. J. Mart, R. D. Osborne, M. M. Stevens, R. V. Ulijn, *Soft Matter* **2006**, *2*, 822.
- [11] S. S. Lee, B. J. Huang, S. R. Kaltz, S. Sur, C. J. Newcomb, S. R. Stock, R. N. Shah, S. I. Stupp, *Biomaterials* **2013**, *34*, 452.
- [12] C. Przybylowski, M. Ammar, C. LeBlon, S. S. Jedlicka, *J. Biomater. Nanobiotechnol.* **2015**, *06*, 146.
- [13] F. Nudelman, K. Pieterse, A. George, P. H. H. Bomans, H. Friedrich, L. J. Brylka, P. A. J. Hilbers, G. De With, N. A. J. M. Sommerdijk, *Nat. Mater.* **2010**, *9*, 1004.
- [14] M. Tavafoghi, M. Cerruti, *J. R. Soc. Interface* **2016**, *13*, DOI 10.1098/rsif.2016.0462.
- [15] A. Singh, J. P. Joseph, D. Gupta, I. Sarkar, A. Pal, *Chem. Commun.* **2018**, *54*, 10730.
- [16] J. P. Joseph, A. Singh, D. Gupta, C. Miglani, A. Pal, *ACS Appl. Mater. Interfaces* **2019**, *11*, 28213.
- [17] C. E. Nweke, J. P. Stegemann, *J. Mater. Chem. B* **2020**, *8*, 3972.
- [18] P. H. J. Kouwer, M. Koepf, V. A. A. Le Sage, M. Jaspers, A. M. Van Buul, Z. H. Eksteen-Akeroyd, T. Woltinge, E. Schwartz, H. J. Kitto, R. Hoogenboom, S. J. Picken, R. J. M. Nolte, E. Mendes, A. E. Rowan, *Nature* **2013**, *493*, 651.
- [19] B. Tsang, Z. E. Dell, L. Jiang, K. S. Schweizer, S. Granick, **2017**, *114*, 3322.
- [20] N. Gupta, D. Santhiya, *Mater. Lett.* **2017**, *188*, 127.
- [21] N. T. K. Thanh, N. Maclean, S. Mahiddine, *Chem. Rev.* **2014**, *114*, 7610.
- [22] N. Gupta, D. Santhiya, A. Aditya, *J. Mater. Chem. B* **2016**, *4*, 7605.
- [23] X. Cai, J. Lin, S. Wang, *Mar. Drugs* **2016**, *15*, 3.

- [24] L. L. Hench, *An Introduction to Bioceramics, Second Edition*, Imperial College Press, **2013**.
- [25] B. Hernandez, F. Pflüger, N. Derbel, J. De Coninck, M. Ghomi, *J. Phys. Chem. B* **2010**, *114*, 1077.
- [26] L. Marsich, L. Moimas, V. Sergo, C. Schmid, *Spectroscopy* **2009**, *23*, 227.
- [27] D. Bellucci, G. Bolelli, V. Cannillo, A. Cattini, A. Sola, *Mater. Charact.* **2011**, *62*, 1021.
- [28] D. Kurouski, T. Postiglione, T. Deckert-Gaudig, V. Deckert, I. K. Lednev, *Analyst* **2013**, *138*, 1665.
- [29] J. Serra, P. González, S. Liste, C. Serra, S. Chiussi, B. León, M. Pérez-Amor, H. O. Ylänen, M. Hupa, *J. Non. Cryst. Solids* **2003**, *332*, 20.
- [30] Y. Miura, H. Kusano, T. Nanba, S. Matsumoto, *J. Non. Cryst. Solids* **2001**, *290*, 1.
- [31] B. P. McGrail, J. P. Icenhower, D. K. Shuh, P. Liu, J. G. Darab, D. R. Baer, S. Thevuthasen, V. Shutthanandan, M. H. Engelhard, C. H. Booth, P. Nachimuthu, *J. Non. Cryst. Solids* **2001**, *296*, 10.
- [32] Y. Tanuma, T. Anada, Y. Honda, T. Kawai, S. Kamakura, S. Echigo, O. Suzuki, *Tissue Eng. - Part A* **2012**, *18*, 546.
- [33] L. T. De Jonge, S. C. G. Leeuwenburgh, J. G. C. Wolke, J. A. Jansen, *Pharm. Res.* **2008**, *25*, 2357.
- [34] D. D. Deligianni, N. D. Katsala, P. G. Koutsoukos, Y. F. Missirlis, *Biomaterials* **2000**, *22*, 87.
- [35] X. Zhao, Q. Lang, L. Yildirimer, Z. Y. Lin, W. Cui, N. Annabi, K. W. Ng, M. R. Dokmeci, A. M. Ghaemmaghami, A. Khademhosseini, *Adv. Healthc. Mater.* **2016**, *5*, 108.
- [36] J. P. Lee, E. Kassianidou, J. I. MacDonald, M. B. Francis, S. Kumar, *Biomaterials* **2016**, *102*, 268.
- [37] C. J. Flaim, S. Chien, S. N. Bhatia, *Nat. Methods* **2005**, *2*, 119.



## Publications

1. \*Pathway driven self-assembly and living supramolecular polymerization in amyloid-inspired peptide amphiphile. **Singh, A.**; Joseph J.; Gupta, D.; Sarkar, I.; Pal, A. *Chem. Commun.*, **2018**, 54, 10730-10733.
2. \*Chirality control to multi-stimuli responsive and self-healing supramolecular metallo-hydrogels. Sharma, B.; **Singh, A.**; Sarma, T. K.; Sardana, N.; Pal A. *New J. Chem.*, **2018**, 42, 6427-6432.
3. \*Pathway driven peptide nanostructures as catalytic amyloid for hydrolase mimick. **Singh, A.**; Joseph, J. P.; Miglani, C.; Gupta, D.; and Pal, A. (Under revision, 2020)
4. \*Peptide nanostructures directed bioglass composites as dynamic and self-healable bone matrix mimick. Gupta, N.; **Singh, A.**; Dey, N.; Joseph, J. P.; Ganguli, M.; Pal, A. (Under revision, 2020).
5. Enzyme responsive chiral self-sorting in amyloid-inspired minimalistic peptide amphiphiles. Gupta, D.; Ranjan, S.; **Singh, A.**; Joseph, J. P.; Miglani, C.; Agasti, S. S.; Pal, A. *Nanoscale*, **2020**, 12, 18692-18700.
6. Photoresponsive chain collapse in flexo-rigid functional copolymer to modulate self-healing behavior. Joseph, J.; Miglani, C.; **Singh, A.**; Gupta, D.; Pal, A. *Soft Matter*, 2020, 16, 2506-2515.
7. Tandem interplay of the host-guest interaction and photo-responsive supramolecular polymerization to 1D and 2D functional peptide materials. Joseph J.,† **Singh, A.**;† Gupta, D., Miglani, C.; Pal, A. *ACS Appl. Mater. Interfaces*, **2019**, 11, 28213–28220. († authors contribute equally).
8. Supramolecular gels from sugar-linked triazole amphiphiles for drug entrapment and release for topical application. Sharma K.; Joseph J. P.; Sahu, A., Yadav N.; Tyagi, M.; **Singh, A.**; Pal, A.; and Kartha K. P. R. *RSC Adv.*, **2019**, 9, 19819-19827.

9. Photoresponsive shape modulation in thymine tethered single chain polymers towards tuning of self-healing behavior. Miglani, C.; Joseph, J. P.; **Singh, A.**; Gupta, D.; Pal, A. Under preparation.
10. Dual control of photodimerization and host-guest interaction for polymer chain collapse in thermo-responsive polymers. Joseph, J.; Miglani, C.; Ray, D.; **Singh, A.**; Gupta, D.; Pal, A. Under preparation.
11. Exfoliated sheets of MoS<sub>2</sub> trigger formation of aqueous gels with acute NIR responsiveness. **Singh, A.**; Kapil, N.; Yenuganti, M.; Das, D., *Chem. Commun.*, **2016**, 52, 14043-14046.
12. Efficient MoS<sub>2</sub> exfoliation by cross- $\beta$  amyloid nanotubes for multistimuli responsive and biodegradable aqueous dispersions. Kapil, N.; **Singh, A.**; Singh, M.; Das, D. *Angew. Chem. Int. Ed.* **2016**, 55, 7772-7776.
13. Cross- $\beta$  amyloid nanohybrids loaded with Cytochrome C exhibit superactivity in organic solvents. Kapil, N.; **Singh, A.**; Das, D.; *Angew. Chem. Int. Ed.* **2015**, 54, 6492-6495.
14. Book Chapter on “Molecular design approach to self-healing material from polymer and its composites” by Springer. Joseph J., Singh, A., Pal, A. **2017**.

(N.B. \* Articles included in this thesis)

## Awards

1. **Best Oral Presenter Award** in 3<sup>rd</sup> In-house symposium at Institute of Nano Science and Technology, Mohali organized on 22<sup>nd</sup> November 2018, India.
2. **Malhotra Weikfield Foundation Nano Science Fellowship Award** in 9<sup>th</sup> Bengaluru India Nano Conference (2018) from **Bharat Ratna Prof. CNR Rao** at The Lalit Ashok, Bengaluru, India.
3. **Best Poster Award** in 1<sup>st</sup> National Workshop on Scanning Probe Microscopy (August, 2016) at National Chemical Laboratory (NCL), Pune, India.
4. **Best Poster Award** in **CRSI, 18<sup>th</sup> CRSI National Symposium in Chemistry (2016)** organized by Institute of Nano Science and Technology, Mohali and Panjab University, Chandigarh, India.
5. **Best Poster Award** in **Conclave on Nano Biotechnology**, December 2014 held at Institute of Nano Science and Technology (INST), Mohali, Punjab, India.



## *Curriculum Vitae*

### ***Ashmeet Singh***

*Ph.D. Research Scholar*

*Institute of Nano Science and Technology (INST) &*

*Indian Institute of Science Education and Research (IISER) Mohali*

*Punjab, India*



Ashmeet Singh completed B.Sc. (H) Chemistry in 2011 from S.G.T.B. Khalsa College, North Campus, University of Delhi and M.Sc. Chemistry in 2013 from Hindu College, Department of Chemistry, University of Delhi. He joined the very first batch of Ph.D. scholars at Institute of Nano Science and Technology (INST) and registered with Indian Institute of Science Education and Research Mohali on 30th July 2014. His research interests include short peptide-based stimuli-responsive functional materials from structural control to catalytic activities. He authored several research articles in reputed international journals. He has presented his research work in several National and International conferences, in some of which he was awarded.